GEOMATICS
ENGINEERING

UCGE Reports
Number 20301

Department of Geomatics Engineering

Arctic Sea Ice Freeboard Heights from Satellite Altimetry

(URL: http://www.geomatics.ucalgary.ca/graduatetheses)

by

Vidyavathy Renganathan

January 2010

SCHULICH
School of Engineering
UNIVERSITY OF CALGARY

UNIVERSITY OF CALGARY

Arctic Sea Ice Freeboard Heights from Satellite Altimetry

by

Vidyavathy Renganathan

A THESIS
SUBMITTED TO THE FACULTY OF GRADUATE STUDIES
IN PARTIAL FULFILLMENT OF THE REQUIREMENTS FOR THE
DEGREE OF DOCTOR OF PHILOSOPHY

DEPARTMENT OF GEOMATICS ENGINEERING

CALGARY, ALBERTA

JANUARY, 2010

Abstract

The Arctic sea ice cover is most sensitive to climate change and variability, mainly due to the ice-albedo feedback effect. With an increase in the average temperature across the Arctic during the past few decades, sea ice has been melting rapidly. The decline in the sea ice extent was estimated as 10% per decade since satellite observations began in 1979. Sea ice thickness is an important parameter that moderates the heat exchange between the ocean and the atmosphere, extent of sea ice deformation and sea ice circulation in the Arctic Ocean. In addition, sea ice thermodynamics and dynamics depend on the thickness of the sea ice cover. In order to estimate the trend in the sea ice volume, both the extent and thickness must be known. Hence, it is important to measure the sea ice freeboard (a representative fraction of the thickness) distribution in the Arctic Ocean.

In this thesis, the total ice freeboards (height of the snow/ice surface above the sea level) were derived from satellite laser altimetry. NASA's Ice Cloud and Land Elevation Satellite (ICESat) carries a Geoscience Laser Altimetry System (GLAS) onboard, and provides dense coverage of snow (or sea ice) surface heights in the Arctic Ocean up to 86° N. The total freeboard height at each ICESat footprint location was computed by removing the instantaneous sea surface height from the ice/snow surface height. In this study, the instantaneous sea surface heights were *modeled* using a combination of geodetic and oceanographic models.

In order to improve the accuracy of the freeboard estimation, an accuracy assessment of the ocean tide models (one of the component models in the sea surface height estimation) in the Arctic Ocean was performed. The Arctic Ocean Tide Inverse Model

(AOTIM-5) was found to have the best accuracy in the Arctic Ocean and was, therefore, used in the sea ice freeboard estimation. It was also shown that the present generation of ocean tide models have ignored the ice-tide interaction processes in the model parameterization, as they are not constrained by observations from sea ice covered regions.

A sensitivity analysis of the freeboard estimation procedure indicates an uncertainty of ~ 0.24 m over a length scale of 100 km. The estimated total ice freeboards were compared with freeboard measurements from other methods (e.g. 'lowest level'), and a good agreement was found between the two methods at regional scales. The sea ice thickness, in the multi-year ice region north of Greenland and Ellesmere Island, was also derived from the total ice freeboard heights by assuming a hydrostatic equilibrium condition. The estimated thicknesses were compared with the thickness measurements from a Helicopter-borne Electromagnetic Induction technique. The difference between the means of the two thickness distributions was ~ 0.53 m, which is well below the accuracy of the thickness estimates of ~ 0.98 m.

The sea ice freeboard estimation procedure, demonstrated in this study, can also be applied to upcoming laser and radar altimetry missions, such as Cryosat-2 and ICESat-2, to continuously monitor the regional, seasonal and inter-annual changes in the Arctic sea ice freeboard (and thickness) distribution.

Acknowledgements

First of all, I would like to thank my supervisor, Dr. Alexander Braun, for supporting, guiding and mentoring me throughout my PhD research. I would like to thank Dr. Michael Sideris and Dr. John Yackel, the members of my supervisory committee, for sharing their expertise in specific topics of my research. I also thank Dr. Benoit Beauchamp for being a member of my Candidacy and Thesis defense committee. I would like to thank Dr. LeeAnn Fishback, external member of the defense committee, for her help and support in planning the field work in Churchill, Manitoba.

I thank Ms. Henriette Skourup and Mr. Rene Forsberg for providing their sea ice freeboard grids for comparison in this Thesis. I also thank them for collaboration in the ArcGICE project. I would like to acknowledge Dr. Jinlun Zhang for providing the mean dynamic topography model, and Dr. Bob Schutz for providing the ICESat orbit information. I thank Mr. Malcolm Lowings for mentoring me and sharing his time and his knowledge in Arctic science.

I acknowledge NSERC, ArcGICE, NRF, Department of Geomatics Engineering, the University of Calgary for providing financial support for this research work. I also acknowledge the Schulich School of Engineering, University of Calgary, for providing funding to attend the 'The Determination and Use of the Geoid' summer school at the University of Copenhagen, Denmark, and the 'IPY Sea ice Summer School' at the University Center in Svalbard, Svalbard. These courses provided a strong foundation for my research work. I greatly appreciate the Graduate Student Association and the Teaching and Learning Center for offering many academic workshops that helped me develop a number of essential skills.

I thank Sina and Martin for helping me with many technical issues. I also thank Wouter for sharing his knowledge in GPS RTK surveying. I acknowledge the gravity group members – Alex, Elena, Feng, Sinem, Kwang Bae, Jin, Mohammed, Ibrahim; past-members – Meda, Matthias, Balaji, Chen; office-mates – Lani, Thaer, Jing and Aboud; and fellow grad students for their friendship and support. I also thank my friends Bert, Poorani, Gopi, Vani, Kumaran, Suren, and Saranya for their friendship.

I express my immense gratitude to my Guru and Dr. Ranjit, Nirmala, Swaminathan, Kelly, and Val for their love and keeping me rooted on this wonderful journey. With all my heart, I express my gratitude to my parents, Meena and Renganathan, and brother, Vasu, for their unconditional love. I have come this far because of your constant support, motivation and faith. Thank you Mom for ‘e-caring’ me while I wrote this Thesis.

Om Namah Shivaya

Table of Contents

List of Tables

List of Figures

List of Symbols and Abbreviations

K_1	Diurnal Lunisolar tidal constituent
M_2	Semi-diurnal Lunar Constituent
O_1	Diurnal lunar tidal constituent
S_2	Semi-diurnal lunar tidal constituent
T_f	Salinity-dependent freezing-point temperature
AMSR-E	Advanced Microwave Scanning Radiometer - EOS (Earth Observing System)
AO	Arctic Oscillation
AODTM	Arctic Ocean Linear-Dynamics Based Tide Model
AOTIM-5	Arctic Ocean Tide Inverse Model
ArcGICE	Combination of Spaceborn, Airborne and In-Situ Gravity Measurements in Support of Arctic Sea-Ice Mapping Project
ArcGP	Arctic Gravity Project geoid model
AVISO	Archiving, Validation and Interpretation of Satellite Oceanographic Data
CHAMP	CHAllenging Minisatellite Payload
CIS	Canadian Ice Service
CSR	Center for Space Research global ocean tide model, version 4.0 or 3.0
DEM	Digital Elevation Model
ECMWF	European Centre for Medium-Range Weather Forecasts
EIGEN-GL04c	Eigen GRACE-LAGEOS-2004-Combination geoid model

EMI	Electromagnetic Induction
ERS	European Remote sensing Satellite
FYI	First-year Ice
GLAS	Geoscience Laser Altimeter System
GOT00.2	Goddard/Grenoble Ocean Tide Model
GPS	Global Positioning System
GRACE	Gravity Recovery and Climate Experiment
HBS	Hudson Bay System
HEM	Helicopter Electromagnetic Induction
IBE	Inverse Barometric Effect
ICESat	Ice, Cloud, and Land Elevation Satellite
IDL	Interactive Data Language
IPCC	Intergovernmental Panel on Climate Change
JASL	Joint Archive for Sea Level
MDT	Mean Dynamic Topography
MEDS	Marine Environmental Database System
MYI	Multi-year Ice
NAO	North Atlantic Oscillation
NASA	National Aeronautics and Space Administration
NCEP	National Centers for Environmental Prediction
NSIDC	National Snow and Ice Data Center
NWP	Northwest Passage

QuikSCAT	Quick Scatterometer
RADARSAT	Radar Satellite
RTK	Real-time Kinematic Survey
SAR	Synthetic Aperture Radar
SIC	Sea Ice Concentration
SRTM	Shuttle Radar Topography Mission
SSM/I	Special Sensor Microwave/Imager
SWE	Snow Water Equivalent
T/P	Topex/Poseidon
TGR	Tide Gauge Record
TPXO6.2	TOPEX/Poseidon global tide model version 6.2
TWL	Tide Water Level
ULS	Upward-Looking Sonar
WGS-84	World Geodetic System 1984

Chapter 1

Introduction

1.1 Motivation

The Arctic sea ice cover plays a vital role in governing the Earth's climate because of its complex interaction between the key components of the Earth's climate system, over a wide range of scales in time and space. Cold, dry sea ice surface reflects most of the incoming solar radiation back to the atmosphere, while the ocean absorbs it. When there is an increase in the radiative forcing (due to climate warming) more melting occurs on the sea ice surface. Consequently, more melt ponds are formed that absorb more radiation which cause further melting of the surrounding sea ice. This creates a feedback mechanism, known as the ice-albedo feedback effect, that accelerates the melting process and leads to a decrease in the sea ice extent. Hence, the climate variability signals are more pronounced in the Arctic. The Arctic sea ice cover is, therefore, an important environmental parameter that serves as an indicator of climate change and variability.

Sea ice also moderates a number of processes in the cryospheric system. (i) It controls the ice-albedo feedback mechanism that amplifies the climate response at high-latitude regions (*Ingram et al.*, 1989). (ii) The growth (melt) rate affects the salt (freshwater) flux from the sea ice cover which is significant to global ocean circulation and deep water formation (*Foster*, 1969). (iii) Due to a relatively thin layer of ice floating on the deep ocean, it is subject to winds and ocean currents. The resulting sea ice dynamics and circulation are responsible for the ice and freshwater export from the Arctic Ocean (section 2.2.2). (iv) The sea ice cover alters the surface heat and mass budget in the Arctic Ocean, which greatly depend on the ice thickness (section 2.1.2). (v) Particulate flux from the sea ice controls the nutrient regeneration, food transport to benthic organisms, and preservation of sediment records of climate change (*Dunbar et al.*, 1998). The sea ice processes, clearly, span a wide range of scales from micrometer to thousands of kilometers and a wide range of disciplines.

Among the two polar regions, the Arctic is studied more extensively, mainly because the sea ice in the Arctic has a higher residence time (5–7 years), the quest for natural resources, and navigation through the Northwest Passage. Despite about 200 years of research and observations, the evolution of sea ice and its role in the climate system is not completely understood making future climate predictions difficult. More observations are required for small- and large-scale processes at longer and continuous time-series. But, field campaigns in the Arctic are challenging due to the nature of the environment and its relative inaccessibility. Hence, remote sensing techniques are crucial as they can provide global coverage and continuous time-series.

Passive microwave satellite remote sensing has, by far, provided the longest observations of sea ice extent and concentration since 1979. The Arctic sea ice extent has been declining at a rate of $\sim$ 2.8% per decade during 1979–1996 (*Parkinson et al.*, 1999). The rate of decline has now shifted to $\sim$10% per decade. The perennial summer sea ice extent reached a minimum in September 2007, that is about 38% lower than the 2005 record low (National Snow and Ice Data Center, see Fig. 1.1). Also, the Northwest Passage was ice-free for the first time since satellite observations began in 1979 (Fig. 1.1).

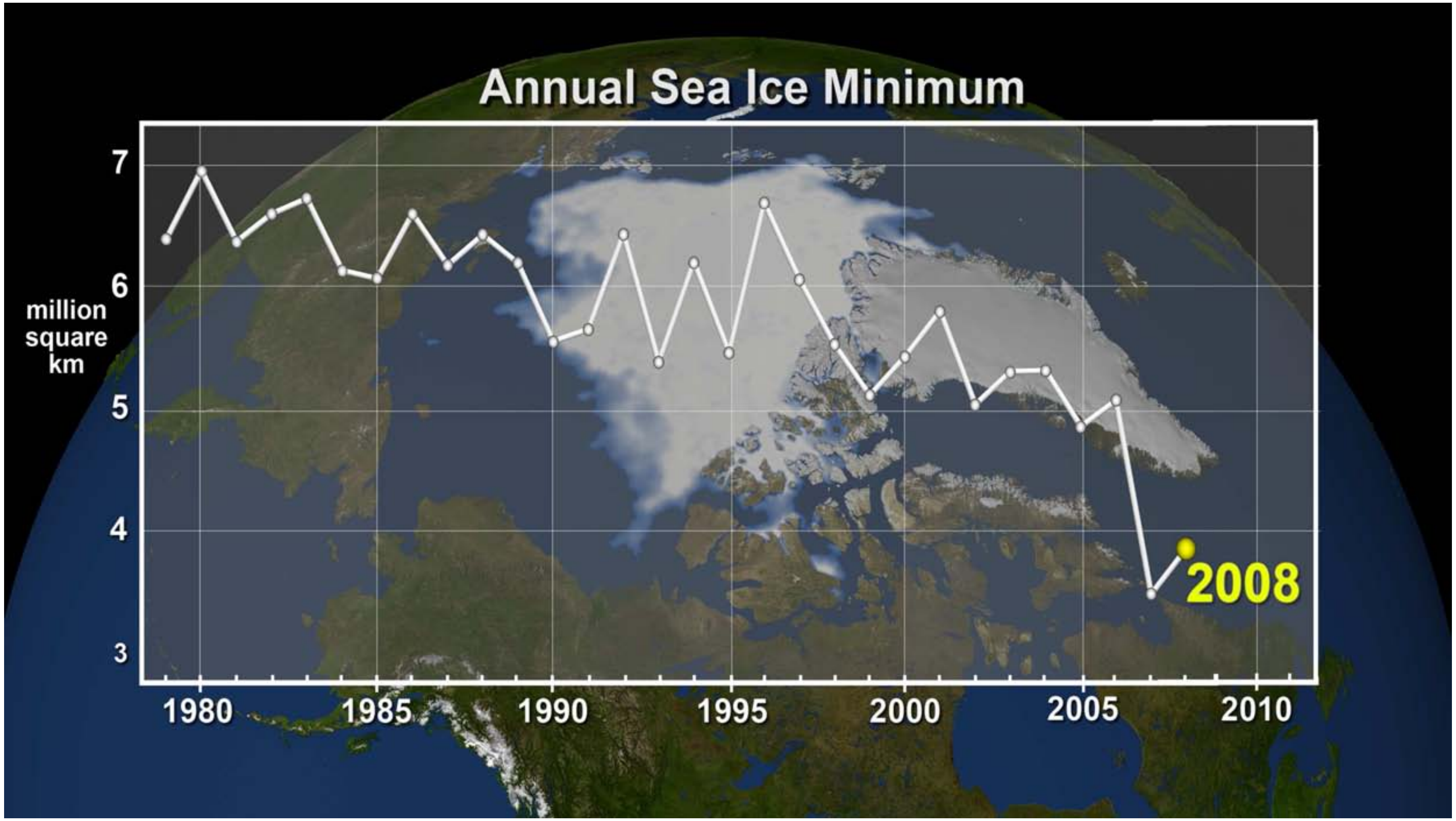

Figure 1.1: A record minimum Arctic summer sea ice extent and the ice-free Northwest Passage in September 2007 (NSIDC. Credit: NASA)

The sea ice thickness controls various processes in the cryospheric system. (i) It moderates the heat exchange between the ocean and the atmosphere. (ii) It influences the surface radiative and turbulent heat fluxes. (iii) Sea ice albedo depends on the ice thickness and its thermodynamic state. (iv) It controls the extent of sea ice deformation due to forcing parameters, such as winds and ocean currents. (v) It also controls the ice-tide (ocean tides) interaction, and affects the tidal amplitude and phase. Hence, the ice thickness distribution and its variability must be *continuously* measured in order to understand these processes.

In order to assess the response of the sea ice cover to climate variability, the change in *sea ice volume* needs to be measured. In other words, both sea ice thickness and extent must be known. So far, remote sensing techniques have been employed to derive a number of climate properties, such as sea ice surface temperature, sea ice extent, sea ice concentration, melt onset/duration, and sea ice motion in the Arctic Ocean. However, it was not possible to measure the sea ice freeboard (height of the sea ice surface from the instantaneous sea surface) at basin-wide scales, until the launch of satellite altimeters such as the European Remote Sensing (ERS) and the Ice, Cloud, Elevation Satellite (ICESat). ERS covered only up to 81.5°N/S, while ICESat, launched in 2003, provides coverage up to 86° N/S. Therefore, ICESat is considered as one of the benchmarks in Cryospheric observation systems. Seasonal and inter-annual variations in the sea ice freeboard distribution can be measured using ICESat which can improve our current understanding of the physical processes in the sea ice system.

1.2 Thesis Objectives

The main objective of this thesis is to derive sea ice freeboard heights in the Arctic Ocean. This research aims to address the following questions to achieve this research objective.

1. Do ICESat laser altimetry data have the potential to provide sea ice freeboard heights in the Arctic Ocean?
2. Instantaneous sea surface height must be known in order to derive the sea ice freeboards. Can the instantaneous sea surface heights be modeled with acceptable accuracy by combining the existing models of the geoid, ocean tides, mean dynamic topography and atmospheric pressure?
3. What is the magnitude of uncertainty in this freeboard retrieval process from ICESat?
4. What is the best available ocean tide model in the Arctic Ocean?
    - How does the sea ice cover in the Arctic Ocean affect the ocean tides?
    - Do the global and regional ocean tide models have acceptable accuracy in the Arctic Ocean?
5. How does the sea ice freeboards derived in this thesis compare with other methods?
6. Can the sea ice thickness be derived from the sea ice freeboard estimates from ICESat?

  - What is the magnitude of uncertainty in this sea ice thickness estimation procedure?

7. How does ICESat elevations compare with field measurements over sea ice?

1.3 Thesis Outline

The research questions posed in the previous section are addressed in the following Chapters.

- In Chapter 2, an overview of the formation of sea ice, its seasonal evolution (*i.e.,* the thermodynamic stages), and the factors that control the sea ice distribution in the Arctic Ocean are presented. It is important to understand these processes in order to interpret the Arctic sea ice freeboard heights derived from ICESat.
- In Chapter 3, the various methods for obtaining sea ice thickness data in the Arctic Ocean, such as field measurements, remote sensing (shipborne, airborne, spaceborne) and numerical modeling, are presented. It is important to understand the measurement principle, the spatial and temporal resolution, and the sources of error before these data sets can be used to validate sea ice freeboards derived from ICESat.
- In Chapter 4, the description of the ICESat sea ice altimetry data, the filtering procedures implemented to obtain sea ice surface elevations, and the methodology used to derive the sea ice freeboards are presented.
- In Chapter 5, the findings from the accuracy assessment of existing global and regional ocean tide models in (i) Churchill, and (ii) the Arctic Ocean are pre-

sented. The ocean tide model that has the best accuracy in the Arctic Ocean will be used in the sea ice freeboard estimation.

- In Chapter 6, the results from the two field experiments conducted in Churchill, Manitoba to compare the ICESat elevations with field measurements over multiple surface types are presented.
- In Chapter 7, the Arctic sea ice freeboards maps derived from ICESat, the sensitivity analysis of the freeboard retrieval procedure, and the validation of sea ice freeboard by comparison with other independent estimates are presented.
- In Chapter 8, a summary of the research findings, conclusions, and an outlook for future work are provided.

Chapter 2

Sea Ice in the Climate System

In this chapter, an overview of the seasonal evolution of sea ice, the factors that control the sea ice thickness distribution, and the current status of the sea ice distribution in the Arctic Ocean are provided. It is important to understand these processes in order to study and interpret the regional, seasonal and inter-annual variations of sea ice freeboard derived from ICESat.

2.1 Evolution of sea ice

2.1.1 Formation

A special property of sea ice is that the temperature of maximum density and the temperature of freezing (T_f) are the same, $-1.86\,^{\circ}\mathrm{C}$, which is slightly lower than the T_f of lake ice because the dissolved salts in the sea water reduce its T_f. As cooling occurs (*i.e.*, maximum density approaches) during the freeze-up period in Fall, the cold water sinks and warm water from below replaces the cold surface water. This process triggers a thermohaline convection and continues until the entire water column (in the mixed layer $\sim$100 m) is at the T_f. Impurities in the sea water (*e.g.*, dissolved salts) act as nuclei for the ice formation or a slush layer (*i.e.*, ice crystals, needles, spicules or platelets) (*Eicken*, 2003). As the temperature continues to drop, further freezing occurs that causes an aggregation of ice crystals, consolidation of the slush layer, and finally, the formation of thin frazil ice.

2.1.2 Growth

Oceanographical and meteorological conditions that prevailed at the time of ice formation, influence the ice growth and ice texture (*Lange*, 1990). For example, pancake ice is formed as the frazil ice aggregates into small discs (∼10 cm) under strong wind action.

The equation of surface heat budget that controls the thermodynamic ice growth is given by *Maykut* (1986) and *Eicken* (2003),

$$(1-\alpha)F_r - I_o + F_L \Downarrow - F_L \Uparrow + F_s + F_e + F_c + F_m = 0, \tag{2.1}$$

where α is the ice albedo, F_r is the incoming solar short-wave flux, I_o is the total short-wave flux penetrating through the ice, $F_L \Downarrow$ is the incoming long-wave flux, $F_L \Uparrow$ is the outgoing long-wave flux, F_s is the sensible heat flux, F_e is the latent heat flux, F_c is the conductive heat flux, F_m is the heat due to melting or freezing processes. The ice continues to grow as long as the net surface heat budget is negative.

$$F_c = -\lambda_{si}\left(\frac{T_0 - T_f}{H}\right), \tag{2.2}$$

where λ_{si} is the thermal heat conductivity of the ice layer, T_0 is the ice surface temperature, T_f is the freezing temperature of the ice bottom and H is the thickness of the ice layer (*Eicken*, 2003).

F_c is one of the important parameters that determines the ice growth rate. It is directly proportional to the temperature gradient between the ice surface and the salinity-dependent freezing temperature at the ice bottom and, inversely proportional to the thickness of the ice layer. Therefore, the ice growth rate increases during

Winter, when there is a stronger temperature gradient and, decreases as the ice gets thicker. In other words, the ice growth rate is less over already thick multi-year ice regions and high over young first-year ice regions.

In the Arctic, the average sea ice thickness that is reached from thermodynamic growth in one year is ∼1.8 m, whereas in Antarctica it is merely ∼0.7 m. Possible reasons are (i) the thicker snow cover over sea ice in Antarctica due to the presence of moisture sources (open ocean), ii) the temperature gradient is not very high in Antarctica (due to higher incoming solar radiation at ∼ 60° S), and iii) the very high oceanic heat flux in Antarctica (*Haas* (2003); also see section 2.2.1 – temperature).

2.1.3 Melting

The incoming solar radiation begins to increase after the period of polar darkness. As the surface temperature increases to the T_f, from strong negative temperatures that prevailed during the winter, the brine volume increases in the ice layer. When the surface continues to get warmer, above the T_f, the surface heat budget becomes positive and, the excess heat is absorbed as latent heat of fusion. At this point, the ice changes its state into water and melt ponds are formed on the surface of the ice. This results in a reduction of the ice albedo and ice thickness. The melt water eventually percolates through the underlying ice layer or evaporates.

Compressed ice leads to the formation of pressure ridges and increases the ice thickness locally. Therefore, a stronger temperature gradient is needed for maintaining its equilibrium. Otherwise, the oceanic heat flux (or F_c) cannot escape through the ice layer and the ridges begin to melt earlier than the level ice. Other factors that cause the melting of ridges are: i) The ridges are void of snow cover. Hence, it has a lower albedo. ii) The ridge keel might reach into the warmer deep water below. iii) Rough bottom topography increases the turbulent heat fluxes. iv) Flanks of the ridges are aligned almost normal to the sun's radiation because of the low elevation (*Haas*, 2003). Therefore, the melting rate is higher over pressure ridges.

2.2 Controlling parameters

The factors that influence the growth, formation and decay of sea ice through the thermodynamic and dynamical processes are enlisted and described in this section. In some cases, the polar hemispherical differences are also discussed.

2.2.1 Thermodynamics

Temperature

The sea ice will form when the air temperature is below the freezing point temperature (T_f) of sea water. Ice production is more efficient when the temperature gradient between air and sea water is large. When the gradient is small, a lesser amount of heat escapes the ocean (more heat is retained) preventing it from freezing. The Arctic Ocean is at a higher latitude (66° N - 90° N) than the Antarctic (50° S - 60° S). Therefore, the air temperature, solar radiation and the duration of summer is lower for the Arctic than the Antarctic (*Haas*, 2003). In the Arctic Ocean, the fresh water input from the river runoff of continental basins stratifies the ocean. This fresh water layer below the sea ice decreases the oceanic heat flux and prevents bottom melting. While, in the Antarctic, there is less riverine input or a fresh water layer. Hence, bottom melting occurs that decreases the ice thickness. Oceanic heat flux in the Arctic is $\sim$10 times less than the Antarctic (*Haas*, 2003). These are some of the reasons why thicker sea ice is observed in the Arctic than in the Antarctic ocean.

Salinity

T_f of water changes with salinity. Hence, the freshwater freezes more readily (S $\sim$0, T_f 0 °C) than the sea water (S $\sim$34 psu, $T_f \sim -1.86\,^{\circ}$C). Thermal properties such as heat capacity and heat conductivity, influence the freezing/melting processes in sea ice, and they are both a function of the bulk salinity (*Eicken*, 2003).

Snow cover

Snow cover provides an insulation for the sea ice layer due to its low thermal conductivity. It reduces the heat flux across the air-sea interface. Therefore, the presence of snow on sea ice during the freeze up period inhibits ice formation; and, during the melt onset, it delays the melting process. Snow cover on sea ice is thicker in the Antarctic because of the presence of moisture sources (open ocean), whereas the Arctic is surrounded by continents. Thick snow can cause negative freeboards in sea ice. As a result, flooding occurs in the snow layer followed by refreezing, and results in the snow-ice or superimposed-ice formation (*Ackley et al.*, 1990), a characteristic of Antarctic sea ice. This process increases the ice thickness in the Antarctic by 20-30% (*Ackley et al.*, 1990). Snow greatly increases the albedo of the sea ice.

Cloud cover

Clouds affect the radiative heat flux across the air-sea ice interface. Incident solar irradiance decreases with cloud cover. Thus, in summer, clouds prevent the heating of the surface layer and delay the melting process. In winter, clouds trap the outgoing longwave emission from the sea ice and reflect it back to the surface, inhibiting the ice formation or growth. Clouds also cause more precipitation (snow) which again reduces the ice growth.

2.2.2 Dynamics

Wind

Ice production is more efficient when the ice is thin, because the heat exchange is more efficient across thin ice. Strong winds can enhance the ice production by transporting the newly formed thin ice (*e.g.*, in Barents Sea) away from the freezing zones (during divergent motion). In some areas, strong winds also cause convergent motion resulting in rafting and/or pressure ridge formation. The contribution of ridging and rafting towards the total sea ice volume is 30∼80% (*Haas*, 2003). Turbulent heat fluxes (sensible and latent heat fluxes), that dominate the surface heat budget over thin ice, are also dependent on the wind conditions. The change in the ice thickness distribution is given by the equation

$$\frac{\partial g}{\partial t} = -\frac{\partial (fg)}{\partial h} + div(\boldsymbol{\nu} g) + \Phi, \tag{2.3}$$

where the three factors that contribute to change in ice thickness distribution ($\partial g/\partial t$) are the thermodynamic growth rate ($\partial h/\partial t$, h is the ice thickness), ice motion ($\boldsymbol{\nu}$ is the velocity vector due to winds and currents) and the re-distribution function (Φ). In the Arctic, the Beaufort Gyre and the enclosed basin causes the sea ice to converge and form thicker ice, whereas in the Antarctic ice is free to drift northwards resulting in divergent motion. Hence, thicker multi-year ice is seen in the Arctic.

Ocean currents

Surface currents and ocean tides play a similar role as the wind forcing. They can cause convergent or divergent motion in sea ice. Ocean currents also transport the salt and heat from the equator to polar regions, thereby moderating the temperature gradient between warm and cold regions; *e.g.*, the Norwegian branch of the North Atlantic Current brings warm saline water into the Norwegian seas, inhibiting the ice formation.

Atmospheric Circulation

Although the Arctic summer sea ice decline is widely attributed to climate warming, part of the variability is due to the Arctic Oscillation (*Morison et al.*, 2006) and North Atlantic Oscillation. Changes in the Arctic Ocean mass distribution, sea ice circulation, reduction in the sea-ice extent and thickness in the eastern Arctic, and surface temperature and wind anomalies are related to the changes in atmospheric circulation associated with the Arctic Oscillation (*Morison et al.* (2007), *Lindsay and Zhang* (2005), and *Rigor et al.* (2002)). *Ogi and Wallace* (2007) and *Rigor et al.* (2002) provide statistical evidence that the Arctic Oscillation index induces anomalies in the sea ice distribution during the ensuing summer.

2.3 Where are we at?

Arctic sea ice is undergoing significant changes due to climate change and variability. Climate change is defined as the statistically significant change occurring in climate properties over decadal scales and is caused by external forcing, such as solar radiation, volcanism, and greenhouse gas composition in the atmosphere (IPCC – *Hegerl et al.* (2007)). Climate variability, on the other hand, occurs at all time scales and is caused by internal forcing, *e.g.*, low-frequency atmospheric variability related to inter-annual changes in atmospheric circulation, such as Arctic Oscillation (IPCC, *Hegerl et al.* (2007)). Climate change and variability signals are more pronounced in the Arctic due to the ice-albedo feedback effect.

Evidences for thinning and retreat of Arctic ice cover can be found in submarine draft measurements (*Rothrock et al.* (1999), *Wadhams and Davis* (2000) and *Rothrock et al.* (2003)), electromagnetic induction measurements of ice thickness in the Arctic transpolar drift (*Haas*, 2004), passive microwave remote sensing observations of sea ice extent (*Serreze et al.* (2003), *Parkinson et al.* (1999)). In spite of the uncertainties in model output of climate models (*Hegerl et al.*, 2007), these models unanimously predict Arctic sea ice decline (IPCC, *Randall et al.* (2007)). They predict ice-free summer in the Arctic Ocean by the end of 2100 (*Zhang and Walsh* (2006) and *Stroeve et al.* (2007)) with abrupt reductions beginning in 2015 (*Holland et al.*, 2006).

Fig. 2.1 shows the regime shift in the age of the Arctic sea ice distribution since the satellite observations began in 1979. The multi-year ice composition was about 52% during 1981–2000. However, this value has dropped to only 19% in 2009, which is a record minimum since 1981 (NSIDC – C. Fowler and J. Maslanik, University of Colorado at Boulder). That is, the sea ice cover at the end of the melt season was predominantly multi-year ice during 1981-2000. Now, it is predominantly thin first-year and second-year ice. Therefore, it is more vulnerable to melt during the following summer melt season.

Increasing variability in the sea ice cover and poor representation of the sea ice in climate models require detailed observations of key physical variables, *e.g.*, ice thickness. The new emerging technique to estimate the sea ice freeboard (that is a fraction of the ice thickness) from radar or laser altimetry is a promising tool to obtain large-scale and long time-series observations. New satellite missions such ICESat, and the upcoming missions ICESat-2 and Cryosat-2, cover up to 86 and 88°

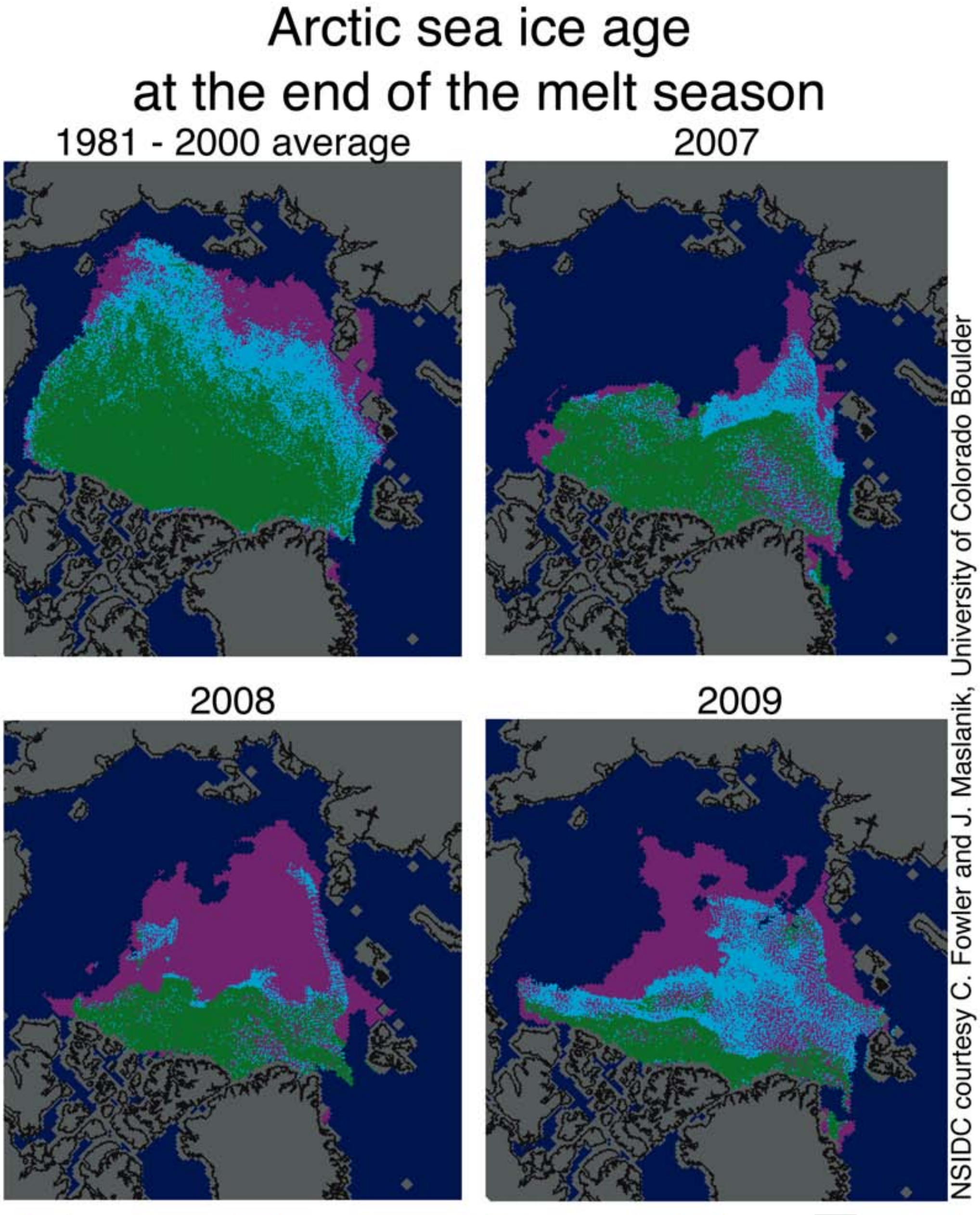

Figure 2.1: The age of the Arctic sea ice during the end of the melt season in 2007, 2008, 2009 and 1981-2000 average. Credit: NSIDC.

N/S, respectively, and will target new features (sea ice) that were not covered by past altimetry missions. Ultimately, sea ice thickness and extent (from satellite altimetry and passive microwave sensors) can be combined to derive a sea ice volume trend in high latitude regions.

Chapter 3

Sea Ice Observations

Motivation

In-situ and other independent measurements of sea ice thickness/freeboard are needed to validate the sea ice freeboard estimates from ICESat. Each measurement technique measures the sea ice variable at different length-scales (spatial resolution) with different levels of accuracy. It is important to understand the measurement principle, spatial resolution, and the inherent errors in those measurements before they can be used to validate the sea ice freeboards derived from ICESat. In this chapter, a description of the observation techniques that are currently used (and have been used in the past) to measure sea ice thickness and other physical variables of sea ice, and the associated uncertainties are presented. First, the definitions of some sea ice parameters that are widely measured to monitor changes in the sea ice cover are provided in the following paragraph.

Definitions – *Sea ice extent*, or the position of the ice edge, is the boundary where the height of the sea ice surface is reduced to the level of the local sea surface. *Sea ice area* is the difference between sea ice extent and open water or leads contained within the region. *Sea ice freeboard* is the height of the sea ice surface above the local instantaneous sea level. *Sea ice draft* (typically about 85% of the thickness) is the depth of the sea ice underside (bottom topography) below the local sea level. *Sea ice drift* is the sea ice motion as a result of external forcing due to winds and/or ocean currents. *Sea ice concentration* is a ratio (expressed in percentage) used to describe the amount of ice covered area as a fraction of a representative area.

3.1 Field Measurements

3.1.1 Drilling

Drilling is a conventional field method used to collect *in situ* ice thickness profiles. Snow depth, ice thickness, and ice freeboard can be measured with an accuracy of about 2∼5 cm. Other snow and sea ice physical properties such as density, grain size, wetness, and salinity are also measured *in situ.* The Atmospheric Environment Program of Environment Canada has established a number of monitoring stations in the Canadian Arctic (∼ 195 sites) since 1947. These locations were selected based on two criteria: (i) stations are close to the shore and, (ii) where the depth of the water will always exceed the maximum ice thickness (*CIS*, 2009). Ice thickness and snow depth were measured using an ice auger or hot wire ice thickness gauge on a weekly basis at approximately the same location. Measurements are taken after the freeze-up period (once the ice surface becomes safe to walk on) and continue until the ice break-up season. The data collected are available from the Canadian Ice Service (CIS) archives. For some stations (*e.g.*, Eureka and Resolute) the record length exceeds 50 years of data. *Brown and Cote* (1992) stated that the potential sources of error in these field measurements are possibly due to variations in measurement locations, changes in field personnel and disturbances within the measurement area.

The New Arctic Program was started in 2002 in order to support climate change studies by updating the historical datasets from the Canadian Arctic monitoring stations, since many stations were no longer operational. Figure 3.1 shows the New Arctic Program stations that were re-opened in Fall 2002. CIS archive data (*CIS*, 2009) are used to plot the landfast ice thickness profiles at selected monitoring stations. The seasonal and annual variability of ice thickness since the freeze-up (October) until the melt onset (May) can be seen in Fig. 3.2. These new data sets can be used to validate measurements from remote sensing techniques, however, with some caution. The *in-situ* drilling measurements represent landfast sea ice conditions and, therefore, cannot be extrapolated to interpret sea ice conditions in the open ocean.

Brown and Cote (1992) analyzed the ice thickness data from 1950 to 1989 in the Canadian Arctic and concluded that (i) the interannual variability of land fast ice thickness is closely tied to annual and decadal variations in snow depth and, (ii) in order to separate the thinning trends from inter-annual variability, longer time series of data from more monitoring stations are needed. Drilling techniques can also be used to infer the thickness distribution in an ice floe, by creating a probability distribution function using sufficient number of samples. *Eicken and Lange* (1989) suggest that a good representation of the thickness distribution in an ice floe is possible to achieve even with shorter profiles. Drilling methods have poor spatial and temporal resolution because they are labor intensive, expensive and are usually carried out in campaigns. On the other hand, they provide a highly accurate validation data set that is required for remote sensing data calibration and validation. *In situ* measurements of physical properties of snow and ice are also needed in order to convert sea ice freeboard into sea ice thickness using isostatic equilibrium assumptions (Equation 3.1).

Ground penetrating radar (GPR) GPRs are also widely used to measure the snow and sea ice thickness by converting the GPR velocities into thickness esti-

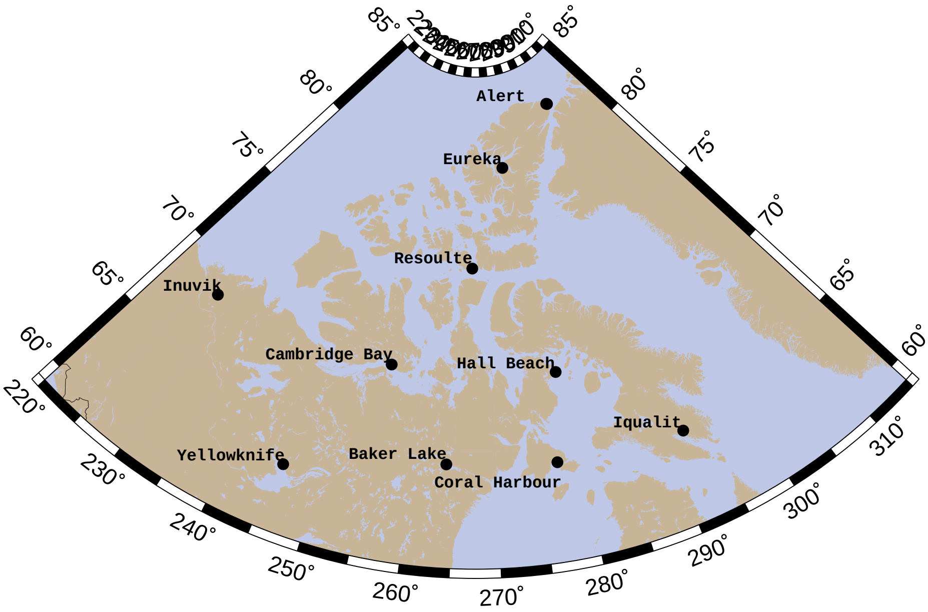

Figure 3.1: The New Arctic Program monitoring stations in the Canada.

mates. This method can provide larger spatial coverage when compared to the drilling method. However, GPR is a field remote sensing technique. Hence, it has a larger uncertainty in the ice thickness measurements when compared to the drilling method. *Galley et al.* (2009) found good agreement between the GPR measurements and the physical and dielectric properties of the snow/ice medium.

3.2 Remote Sensing

3.2.1 Submarine

Upward-Looking Sonar (ULS) ULSs are mounted on submarines and used to measure the sea ice draft (Fig. 3.3). The pressure sensor located in the submarine's hull measures the depth of the ULS below sea level. The sonar transducer mounted on the conning tower of the submarine measures the time taken by the sound beam to reach target (under-ice topography) and reflect back to the transducer (which can

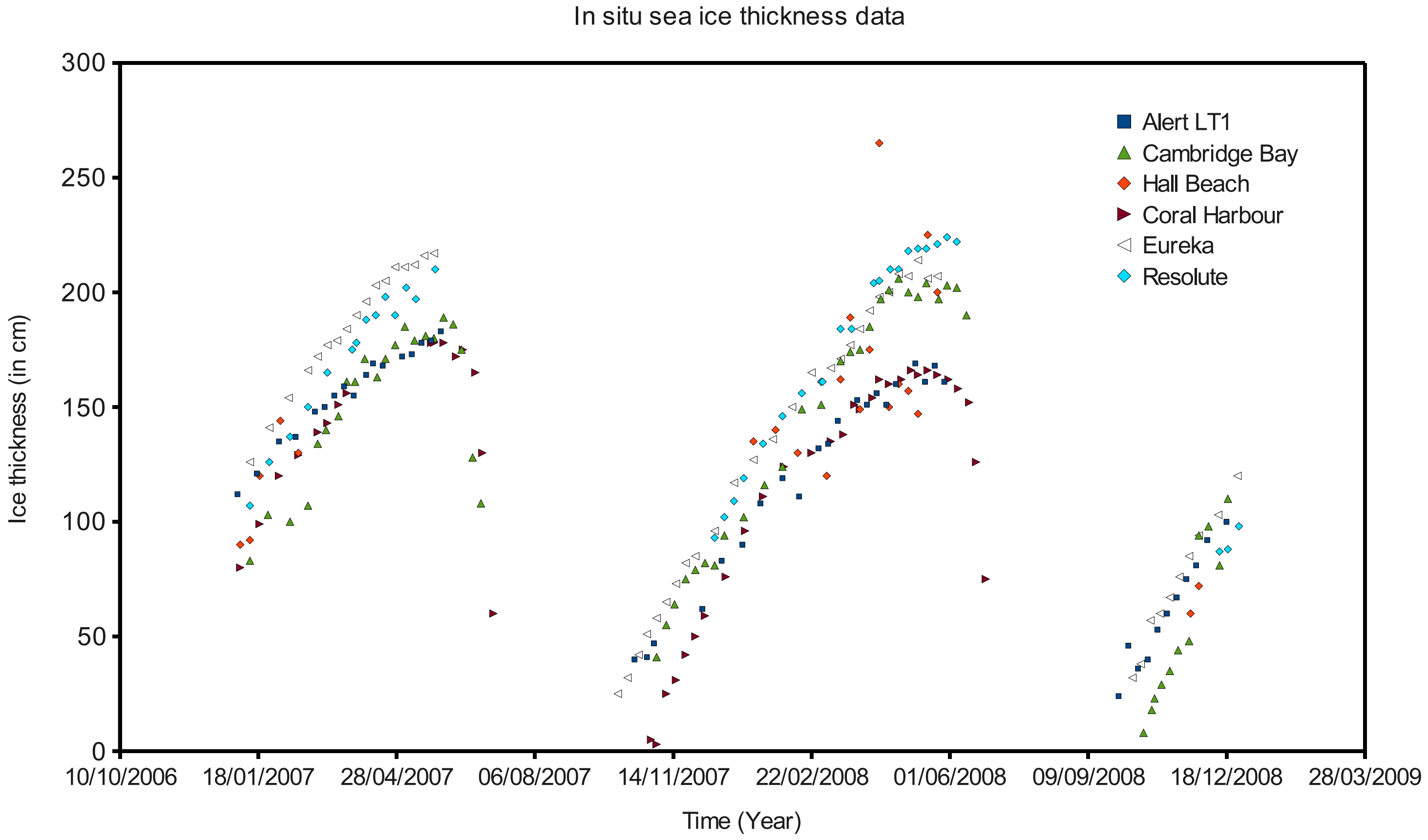

Figure 3.2: The land-fast ice thickness profiles measured at a number of monitoring stations in the Canadian Arctic. Data archived by the Canadian Ice Service.

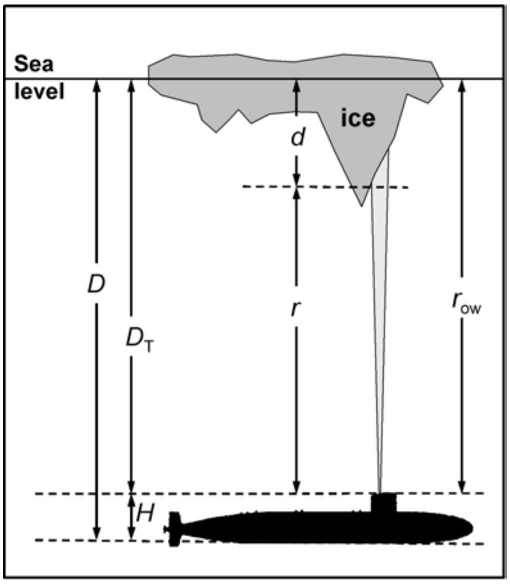

Figure 3.3: A schematic representation of the submarine, sonar beam, and the ice cover. The pressure sensor measures the keel depth, D. The height H is the vertical distance from the pressure sensor to the sonar transducer, mounted on the conning tower at depth D_T. 'r' and '$r_o w$' are the ranges to the ice and open water. 'd' is the measured sea ice draft. Source: *Rothrock and Wensnahan* (2007).

be interpreted as the distance between the ULS and ice bottom surface). These two measurements are combined to derive the sea ice draft.

Sea ice thickness, t, can then be calculated from the sea ice draft, d, by assuming isostatic equilibrium, using equation 3.1,

$$t = \frac{\rho_w d - \rho_s s}{\rho_i}, \tag{3.1}$$

The snow depth (s) and the densities of water (ρ_w), ice (ρ_i) and snow (ρ_s) are obtained from *in situ* measurements or standard values are assumed. The standard values and the expected uncertainties in each of these parameters are described in more detail in Chapter 7, section 7.3.

ULS mounted on United States Navy submarines have routinely measured the ice draft in the Arctic Ocean since 1958 (*Rothrock et al.*, 1999). Data from approximately 70 cruises, at least one per year that lasted about 20-40 days, were archived. These data include measurements of both the winter maximum and the summer minimum ice draft. Data from 1976-2000 covering about 120,000 km of profiles were made available to the science community through the National Snow and Ice Data Center (NSIDC) .

These draft measurements were collected for safe maneuvering of submarines in ice-covered oceans and were not intended for scientific research. Hence, these data sets have random spatial and temporal coverage. If these data sets are to be used in scientific research, knowledge of their quality or an error estimate is essential. *Rothrock and Wensnahan* (2007) identified the possible sources of errors in submarine draft measurements, namely measurement precision, errors in identifying open water, sound speed error, errors due to variable sonar footprint size, uncontrolled gain and thresholds, difference between analog and digitally recorded data. The measured pressure is converted into keel depth using an assumed sea water density value, which introduces additional errors. *Rothrock and Wensnahan* (2007) report that the submarine drafts have a tolerable error of $\sim$ 25 cm averaged over 10's of kilometers and, therefore, these data sets can be used to validate observations from spaceborne techniques.

Submarine drafts were used in a number of studies to estimate the thinning of Arctic sea ice cover (*e.g.*, *Rothrock et al.* (1999), *Rothrock et al.* (2003), *Yu et al.* (2004), *Zhang et al.* (2000), *Wadhams and Davis* (2000)). *Rothrock et al.* (1999) found that the mean ice draft in the Arctic Ocean decreased by $\sim$ 40% between 1958-

1976 and 1993-1997. *Wadhams and Davis* (2000) found a 43% decrease in mean ice draft between 1976-1996. Studies attribute the decrease in ice draft to (i) changes in precipitation, and (ii) increased ice export that is associated with decadal variations in atmospheric circulation, North Atlantic Oscillation (NAO) and Arctic Oscillation (AO) (*Kwok and Rothrock*, 1999).

3.2.2 Airborne

Electromagnetic Induction The Electromagnetic Induction (EMI) sounding technique has been used, since 1990, to collect sea ice thickness measurements in the Arctic and the Antarctic (*Kovacs and Holladay* (1990), *Haas* (2004), *Eicken et al.* (2001)). The EMI instrument can be used to collect both ground-based and airborne data. However, they can yield only limited spatial and temporal resolution compared to the spaceborne techniques. Shipborne measurements are possible but are limited by the fact that ships cannot penetrate through the thickest ice regions. The EMI technique is based on measuring the sub-surface mean electrical conductivity. Because of the strong contrast in electrical conductivity between sea ice layer, $0 \sim 50\ mSm^{-1}$ (millisiemens per metre) and underlying cold sea water, $\sim 2500\ mSm^{-1}$, the EMI can successfully distinguish between the two mediums and measure the sea ice thickness (*Haas*, 2003). The transmitter coil creates a primary electromagnetic field that induces eddy currents at the ice-ocean interface (see Fig. 3.4). As a result, a secondary electromagnetic field is generated. The receiver coil then measures the strength and phase of the secondary field which is dependent on the thickness of sea ice. Thick ice produces a weak secondary field, while thin ice produces a strong secondary field.

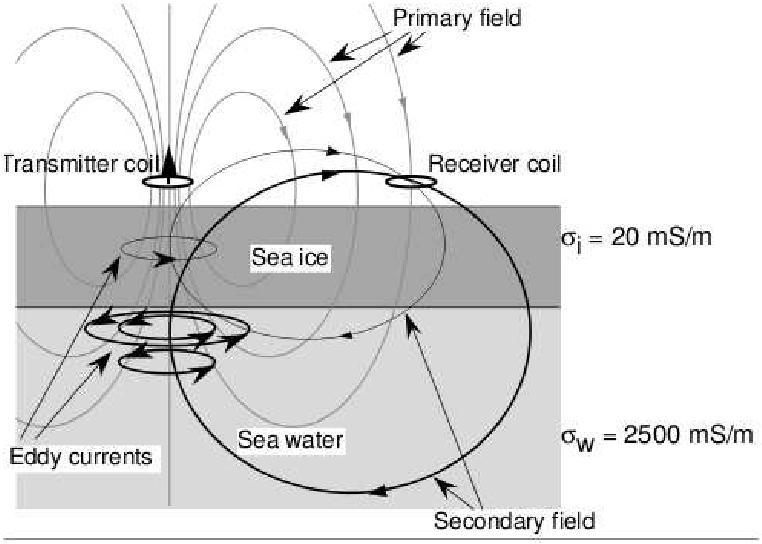

Figure 3.4: The principle of Electromagnetic Induction ice thickness sounding. Source: *Haas* (2003). The transmitter coil generates the primary field that induces eddy currents at the ice-ocean interface. Consequently, a secondary field is generated. The receiver coil measures the amplitude and phase of the secondary field.

The EMI method has an accuracy of ∼ 10 cm over level ice, estimated from the comparisons with drilling measurements (*Haas*, 2003). It has a much poorer accuracy over pressure ridges, because the ice thickness is underestimated in those regions. The measurements are averaged over a certain footprint area that is approximately equal to the distance between the sensor and the water surface. Hence, over ridge keels, the receiver records mixed signals from the narrow ridge keel and the adjacent sea water, thus underestimating the ice thickness. In Antarctica, the gap layer below the superimposed ice also causes underestimation of ice thickness (*Haas*, 2003). If the height of the sensor system above the sea level is known, then freeboard can be derived using isostatic equilibrium assumptions (Equation 3.1). These independent EMI freeboard estimates can be used as validation data for freeboard estimates from satellite altimetry.

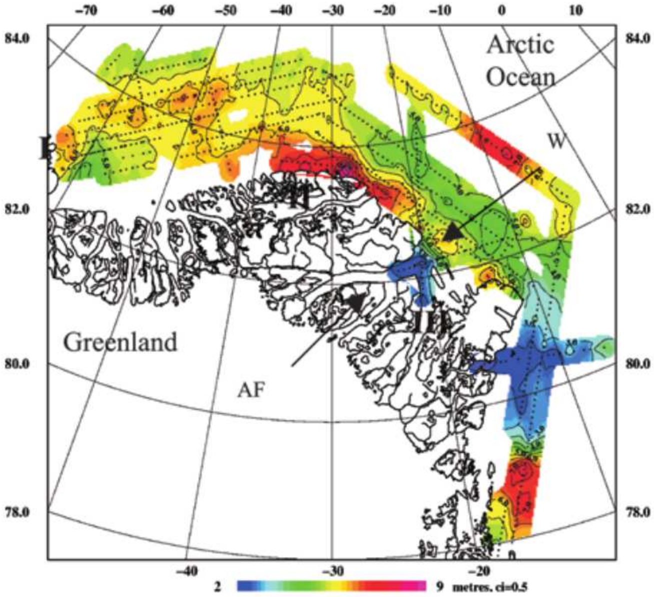

Figure 3.5: Mean ice thickness measured from an airborne laser altimeter near Greenland from mid to late June 1998. Source: *Hvidegaard and Forsberg* (2002).

Haas et al. (2008) analyzed airborne-EMI measurements made from helicopters during late summers of 2001, 2004 and 2007 over the Transpolar Drift. They found an ongoing reduction of up to 44% in the mean ice thickness near the North Pole region and suggested that the main reason for this reduction is due to a regime shift in sea ice from multi-year ice to second-year ice to first-year ice.

Laser Altimetry Sea ice freeboards can be derived using airborne laser altimetry techniques. *Hvidegaard and Forsberg* (2002) analyzed data collected with an Optech 501SX laser altimeter during the airborne gravity campaigns in 1998 over the polar seas off northern Greenland. Figure 3.5 shows the ice thickness calculated from the measured freeboards. *Hvidegaard and Forsberg* (2002) estimated an accuracy of ∼15 cm for the derived freeboards and a thickness accuracy of ∼1 m. The laser altimeter operates at a wavelength of 904 nm and has a footprint size of less than 1 m.

GPS (Global Positioning System) receivers onboard provides precise positioning. A laser altimetry system measures the surface elevation which is reduced to sea ice freeboard by combining the elevations with a regional geoid model (*Forsberg et al.*, 2000). Sea ice freeboard can be converted into sea ice thickness using isostatic equilibrium assumptions (Equation 3.2).

$$K = 1 + \frac{\rho_i h_i + \rho_s h_s}{h_i(\rho_w - \rho_i) + h_s(\rho_w - \rho_s)} \tag{3.2}$$

where K is the conversion factor, h and ρ are the thickness and density values respectively, for ice (i), snow (s) and water (w). The standard values and the expected uncertainties in each of these parameters are described in more detail in Chapter 7, section 7.3.

Major error sources were identified as snow loading (leads to an overestimation of thickness), lack of open water regions (leads to underestimation of thickness) and, errors in the freeboard to thickness conversion factor (on the order of ∼30 cm, *Wadhams et al.* (1992).

Varnai and Cahalan (2007) describe the potential of offbeam lidar techniques to provide snow and ice thickness measurements. The method is based on, "observing the horizontal spread of lidar pulses: The bright halo observed around an illuminated spot extends farther out in thicker layers because photons can travel longer without escaping through the bottom" (*Voss and Schoonmaker* (1992), Fig. 3.2.2). This principle was already used in many applications, *e.g.*, to measure thickness of clouds (*Polonsky et al.*, 2005). Sea ice halos are usually larger because sea ice is much thicker than snow and snow halos are brighter because snow has more scatterers in the medium (*Varnai and Cahalan*, 2007). The authors report that for snow and

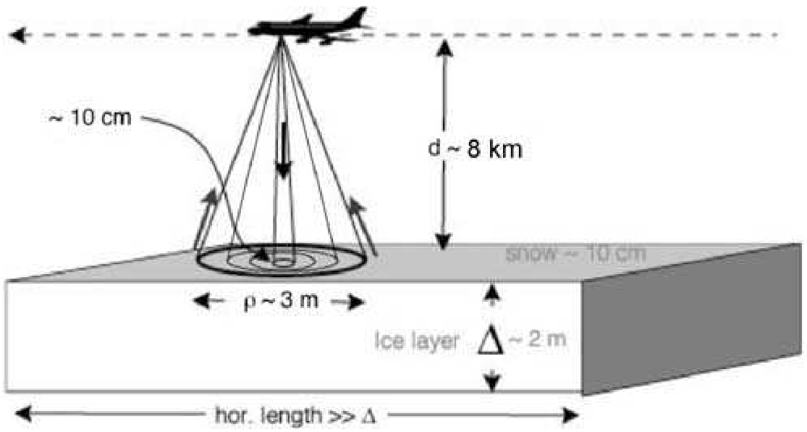

Figure 3.6: A schematic representation of the airborne sea ice measurements using offbeam lidars Source: *Varnai and Cahalan* (2007).

sea ice thickness (< 30 cm and 3 m, respectively) the uncertainties in the thickness retrievals are $\sim 10\%$.

3.2.3 Spaceborne

Passive Microwave The first global views of the sea ice cover was made possible by the development of spaceborne measurement techniques. Passive microwave sensors have been used to monitor the sea ice extent, area, concentration and velocity since 1978. Advanced Very High Resolution Radiometer (AVHRR), Scanning Multichannel Microwave Radiometer (SMMR) and Special Sensor Microwave/Imager (SSM/I) have been widely used to determine the trends in sea ice extent (Fig. 1.1, *Gloersen et al.* (1999), *Parkinson et al.* (1999), *Comiso* (2002), *Comiso et al.* (2003) and *Comiso and Parkinson* (2008)). *Agnew et al.* (2008) used AMSR-E enhanced resolution data from 2002-2007 to estimate the daily sea ice area fluxes between the Canadian Arctic Archipelago and the Arctic Ocean and Baffin Bay. *Cavalieri and Parkinson* (2008) analyzed 28 years of Antarctic sea ice extent derived from SSM/I and SMMR and found that the total Antarctic sea ice extent trend increased slightly from approximately 1.0 ± 0.4% per decade. *Kwok* (2008) used AMSR-E data to reliably retrieve sea ice motion in the Arctic. He states that this sensor has improved spatial resolutions and lower sensitivity to atmospheric moisture which resolved a number of previous issues with the sea ice motion retrieval process.

Gloersen et al. (1999) reported a global sea ice extent decrease by $0.01 \pm 0.003 \times 10^6\ km^2$ per decade and decrease in areal coverage as $0.009 \pm 0.002 \times 10^6\ km^2$. *Parkinson et al.* (1999) analyzed a 18.2 year record of Arctic sea ice extent from SSM/I (1978-96) and found seasonal, regional, and interannual variabilities with an overall decreasing trend of 34300 km^2yr^{-1}. It is important to note that in order to comprehensively study the changes in sea ice cover due to climate change and variability, change in sea ice *volume* (both area and thickness) must be analyzed.

Sea ice velocities can also be derived from SSM/I. *Alexandrov et al.* (2000) studied the sea ice exchange between Laptev Sea and the Arctic Ocean using ice drifts from SSM/I, imaging side-looking radar and a dynamic-thermodynamic model. *Kwok* (2000) examined the sea ice motion associated with NAO using 18-years of SSM/I and buoy data. Variation in the sea level pressure due to NAO results in wind forcing, which in turn changes the sea ice circulation in the Arctic Ocean. Consequently, ice flux, ice extent, and ice thickness distribution are affected. *Kwok and Rothrock* (1999) and *Kwok et al.* (2004a) identified significant correlation between sea ice area flux through the Fram strait and the NAO index.

Because of its capability to monitor during day/night and at almost all-weather conditions at global scale with high temporal resolution (∼ daily), passive microwave sensors are the primary tool that provides relatively long historical record of sea ice conditions in the Arctic and Antarctic. SSM/I data have a spatial resolution of about 25 $km \times 25$ km. These data are freely available through NSIDC and have been used in a number of studies to analyze the spatial and temporal variations in sea ice cover at global scales. Fig. 3.7 shows the Arctic sea ice extent which was $\sim$ 15.14 million square kilometers on February 28, 2009, the day it reached a winter maximum for the year (source: NSIDC). The maximum extent was reported to be 720,000 square kilometers less than the 1979-2000 average (NSIDC).

Synthetic Aperture Radar Synthetic Aperture Radar (SAR) is a spaceborne imaging radar system onboard RADARSAT–1/2, ERS–1/2, Envisat ASAR, and TerraSAR-X satellites among others. SAR backscatter data have been used to discriminate between various features, such as multi-year ice (MYI), first-year ice (FYI), and open water or leads (*Kwok et al.* (2004b), *Melling* (1998)). Figure 3.8 shows MYI characterized by its brighter tone and rough texture (region A), old ice floes identified by bright round shapes (regions C and D), open water distinguished by its dark tone (region E) and pressure ridges identified by bright linear features (region F). Sea ice type information obtained from SAR backscatter data can be used to interpret radar/laser altimetry waveforms. Therefore, the laser altimeter onboard ICESat (which delivers both the waveform and ellipsoidal height for every footprint) has the potential to provide both thickness and sea ice type information.

Bogdanov et al. (2007) describe a number of algorithms to retrieve sea ice parameters from SAR data, including supervised and unsupervised sea ice classification and sea ice concentration. SAR data have also been used to study the sea ice motion and deformation in the Arctic Ocean (*Kwok and Cunningham* (2002), *Kwok* (2004)). *Barber et al.* (1998) identified the different thermodynamic phases in the

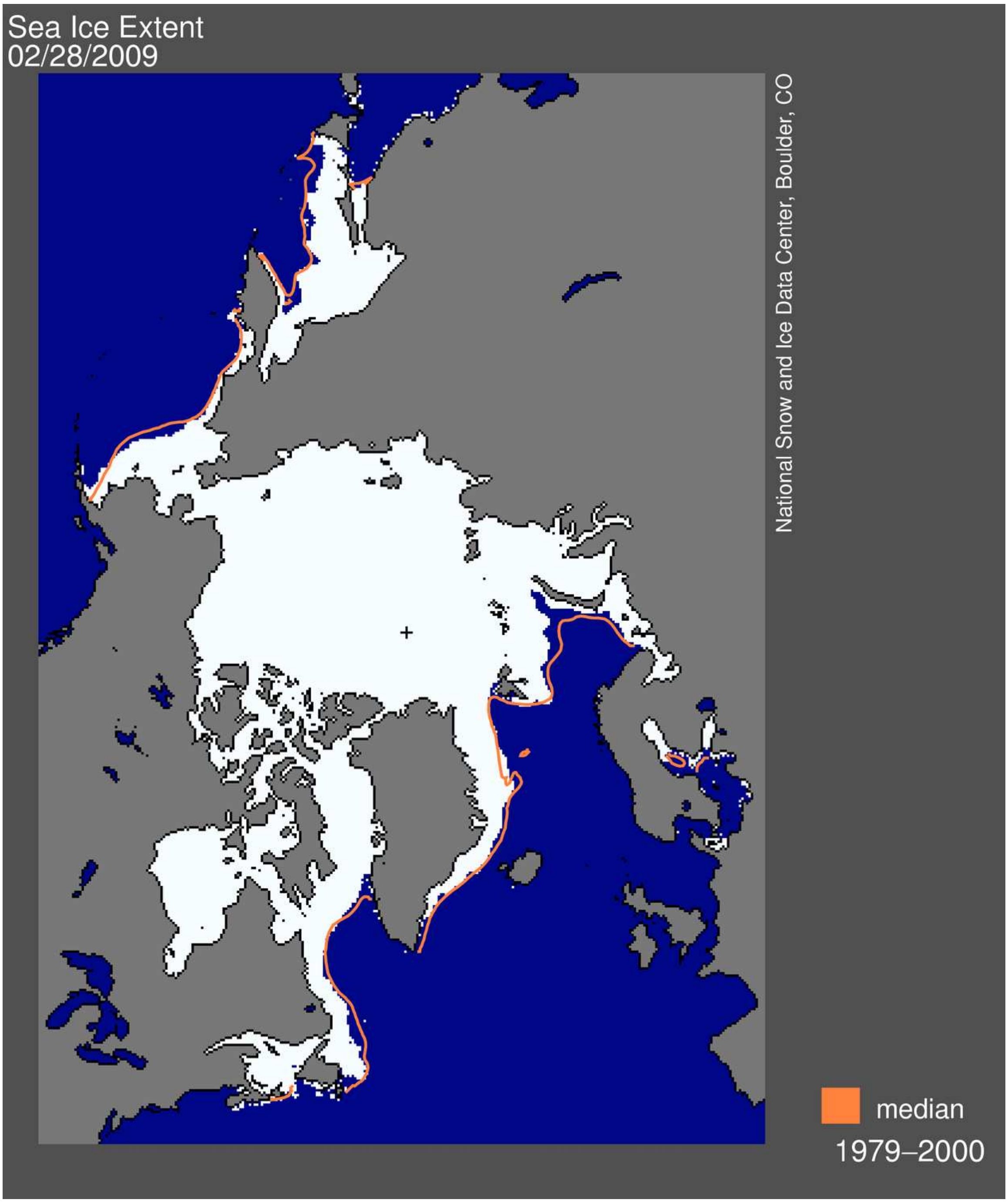

Figure 3.7: Arctic sea ice extent on February 28, 2009, the date of the annual maximum. The orange line shows the 1979 to 2000 median extent for that day. Credit: National Snow and Ice Data Center.

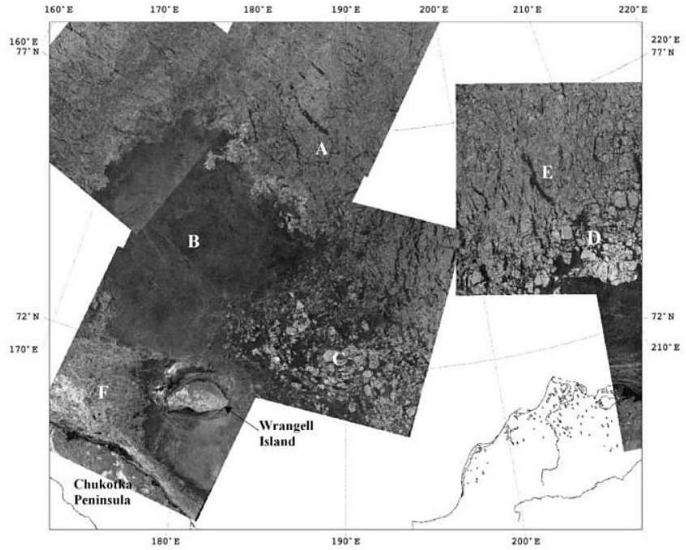

Figure 3.8: RADARSAT SAR image showing different sea ice types in the East Siberian Sea. A – multi-year ice; B – first-year ice; C and D – floes of old ice; E – leads. Source: *Alexandrov et al.* (2007).

seasonal evolution of radar backscatter: fall freeze up, winter, early melt, melt onset and advanced melt. Changes in backscatter for snow-covered FYI and MYI during these periods are shown in *Barber et al.* (2001). *Yackel et al.* (2001) evaluated the potential of time-series RADARSAT-SAR data to detect the melt onset on landfast FYI. *Wadhams et al.* (1991) found a positive correlation between SAR backscatter level and ice drafts (measured by sonar), although the processes that influence the backscatter are not directly related to thickness. They reported that only 46% of the backscatter variances are explained by draft variations. In summary, SAR systems are an important tool for monitoring the geophysical state of the sea ice.

3.3 Sea Ice Modeling

Coupled ice-ocean models were developed to improve our understanding of the Earth's climate and how it is changing by studying the air-sea-ice interaction. The thermodynamic growth and dynamical redistribution of sea ice are modeled typically with forcing parameters such as winds, currents, albedo and temperature, and are constrained with observations. *Hibler* (1979) developed a dynamic thermodynamic sea ice model where the sea ice thickness was treated in only two-categories, as thick ice or open water. Later, *Hibler* (1980) and a number of researchers adapted a variable thickness sea ice model based on *Thorndike et al.* (1975) to improve the model simulation. The ice-thickness distribution function is given by

$$\frac{\partial g}{\partial h} = -\nabla.(\mathbf{u}g) - \frac{\partial (fg)}{\partial h} + F_L + \psi \tag{3.3}$$

where g is the ice-thickness distribution function, t is time, $\mathbf{u}$ is ice velocity in x and y direction, f is the ice growth rate, h is the ice thickness, F_L term describes lateral melting and ψ is a redistribution function due to ridging.

Zhang and Rothrock (2001) further improved the *Thorndike et al.* (1975) model by incorporating the sea ice enthalpy distribution that conserves both the ice mass and ice thermal energy. *Bitz et al.* (2001) simulated the ice thickness in a coupled-climate model based on *Thorndike et al.* (1975), where the thickness distribution is Eulerian in x-y space and Lagrangian in h space, while in *Thorndike et al.* (1975) it is Eulerian in both domains. The difference between the lagrangian formulation of the ice-thickness and the eulerian method is that the lagrangian method allows for the inclusion of a vertical temperature profile with relative ease (*Bitz et al.*, 2001). *Lindsay* *and Zhang* (2006) developed a sea ice model by assimilating observational sea ice concentration and sea ice velocity data which improved the model results significantly when compared with the ice draft measurements. *Miller et al.* (2007) and *Miller et al.* (2005) report that their Arctic sea ice thickness model was found to correlate well with observations when the large scale shear strength of the sea ice leads was increased and observational data of sea ice thickness, draft, extent, and velocity are used in model development. *Rollenhagen et al.* (2009) developed a finite element sea ice model by assimilating 3-day mean sea ice drift fields obtained from passive microwave sensors and found that thickness distribution became more realistic. *Randall et al.* (1998) and *Steele and Flato* (2000) reviewed the recent progress made in sea ice model development. In summary, a number of sea ice models are developed and improved by parameterizing a more realistic dynamic and thermodynamic processes in sea ice.

3.4 Summary

The number of field and remote sensing techniques that are used to measure the sea ice thickness and other physical variables of the sea ice cover were described. A list of the measurement techniques and the expected errors are presented in Table 3.1. The expected error in spaceborne techniques are discussed in Chapter 7.

Table 3.1: Techniques used to measure the sea ice thickness and their expected uncertainty

Method	Parameter	Uncertainty
Drilling	Thickness	2∼5 cm
Upward-looking Sonar	Draft	25 cm over 10's km
Airborne Electro-magnetic Induction	Thickness	10 cm over level ice
Airborne laser altimetry	Freeboard	15 cm

Chapter 4

Arctic Sea Ice Freeboard Heights from Satellite Altimetry

In this chapter, the satellite radar altimetry measurement principle, the Arctic sea ice thickness from the European Earth Resources Satellite (ERS), the ICESat and GLAS systems, and the principle of Arctic sea ice freeboard retrieval from ICESat are introduced.

4.1 Radar altimetry measurement principle

The main objective of satellite radar altimetry is to measure the distance from the satellite to the ocean surface, *i.e.*, the range. The altimeter transmits radar pulses that interacts with the sea surface and get reflected back to the altimeter receiver system. The round-trip travel time of the received pulse is then determined to calculate the range using the formula (section 2.4 in *Chelton et al.* (2001)),

$$R = \hat{R} - \sum_j \Delta R_j, \tag{4.1}$$

where $\hat{R}$ = c*t/2. $\hat{R}$ is the range calculated from the round-trip travel time t and the speed of light c. R is the corrected range. ΔR_j are the positive corrections that are removed from $\hat{R}$ to correct for atmospheric refraction effects, sea-state biases, instrument corrections such as antenna gain and doppler shift, and geophysical corrections such as geoid height, ocean tides and atmospheric pressure loading.

For more details about the radar measurement principles, range corrections and sea surface height determination refer to *Chelton et al.* (2001).

4.2 Overview of the ICESat laser altimeter mission

Mission objective The main objective of the Ice, Cloud, Elevation Satellite (ICESat) mission is to monitor the polar ice sheets and determine the inter-annual and long-term mass changes with high accuracy and precision (*Zwally et al.*, 2002). Specifically, the mission objective was to reduce the uncertainty in the ice sheet mass balance estimates by achieving an accuracy of better than 2 cm/yr over a 100 km x 100 km area (*Schutz et al.*, 2005). In order to achieve this optimistic objective, ICESat utilized a narrow beam laser altimeter with sophisticated design and instrumentation. A number of calibration and validation experiments were carried out to ensure that the elevation products meet the science requirements in terms of accuracy and precision. In this study, two campaigns were carried out in Churchill, Manitoba, to determine the accuracy of ICESat over multiple surface types (Chapter 6).

Applications Although, ICESat was primarily designed to meet the increasing demands of cryospheric research (polar ice sheets and Arctic sea ice), the 15 Geoscience Laser Altimeter System (GLAS) data products are currently used in many multidisciplinary and interdisciplinary applications such as land topography, hydrology, oceanography, vegetation canopy heights, cloud heights and atmospheric aerosol distributions.

Mission description ICESat was launched from the Vandenberg Air Force Base, California on January 13, 2003 into an orbit of $\sim$ 600 km altitude and 94° inclination.

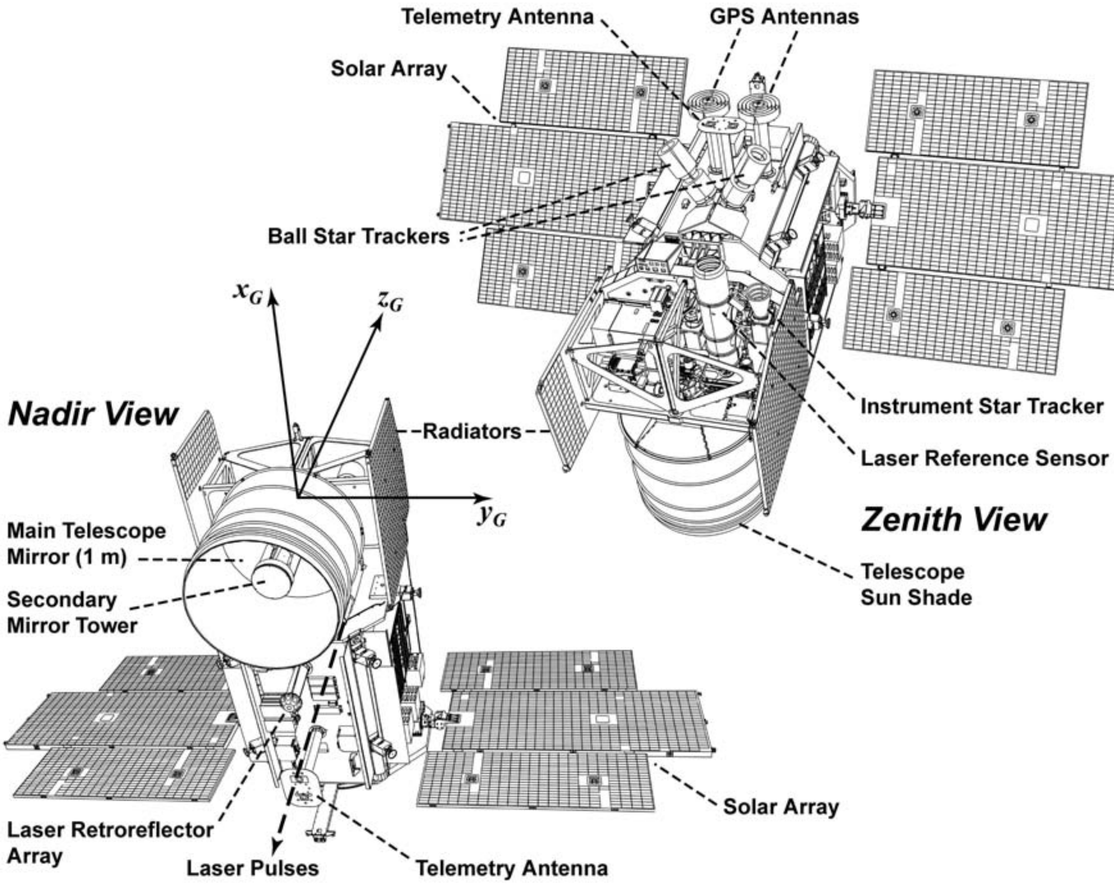

Figure 4.1: Nadir and Zenith views of the Ice, Cloud, and Elevation Satellite and Geoscience Laser Altimeter System (*Schutz et al.*, 2005).

This inclination was mainly chosen to allow for the comparison of derived elevations at crossover points (*Schutz et al.*, 2005). The two reference orbits that were used in the mission are an 8-day repeat and a 91-day exact repeat (with a 33 day sub-cycle). The 91-day interval provides a denser track coverage for science applications, while the 8-day interval allows frequent repeats of ground calibration sites. In sub-Arctic and Arctic regions, the tracks are more densely spaced than near the equator and, therefore, it provides dense coverage for the sea ice application.

ICESat carries the Geoscience Laser Altimeter System (GLAS) (see Fig. 4.1). GLAS produces 1064 nm and 532 nm laser pulses at a rate of 40 Hz – 1064 nm for surface altimetry and dense cloud heights and 532 nm for vertical distribution of clouds and aerosols studies (*Spinhirne et al.*, 2005). The transmitted laser pulses illuminate a footprint area of $\sim$ 65 m in diameter and a footprint spacing of $\sim$ 172 m (Fig. 4.2). GLAS has three lasers (referred to as laser 1, 2 and 3) mounted on a rigid optical bench, which is the reference for GLAS measurements, with only one laser operating at a time. Laser 1 started firing on February 20, 2003 but failed on March 29, 2003. The Independent GLAS Anomaly Review Board concluded that the most likely cause for the failure for laser 1 was an unexpected failure mechanism in a pump diode array and rise in oscillator temperature that led to excessive power degradation. These early issues in laser life time required a reduction in the laser operating period to 33-days, three times per year – February/March, May/June, October/November (*Abshire et al.*, 2005), which would still meet the science requirements of polar ice sheet monitoring studies (*Schutz et al.*, 2005). Laser 2 started firing on September 25, 2003 and collected data during three ICESat epochs. On June 21, 2004, laser 2 was switched off and laser 3 started the data acquisition and continued on until October 19, 2008, when it failed. On November 25, 2008, laser 2 was turned back on and acquiring data from Fall 2008 to Spring 2009. Laser 2 unexpectedly stopped firing on October 11, 2009 during the Fall 2009 campaign. With the completion of the spring 2009 campaign, the GLAS instrument successfully completed taking over 1.9 billion measurements.

The spacecraft was designed to accommodate special off-nadir pointing maneuvers that would allow the laser to be pointed at selected targets that lie slightly off the

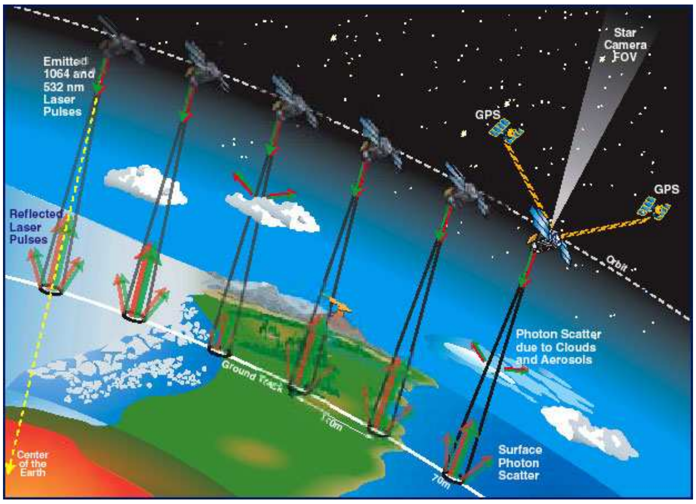

Figure 4.2: ICESat measurement principle – GLAS measures the range to the surface (land, ocean, sea ice) and clouds by transmitting short laser pulses at two frequencies (near infrared and green). The ICESat position is determined from the GPS and ICESat orientation and location of the laser footprint on the surface are determined by the Instrument Star Tracker and Precise Attitude Determination (*Zwally et al.*, 2002).

nominal nadir track (up to +/- 50 km away). These special maneuvers were also used in compensating for the orbit drifts, carried out near polar regions, and to support calibration/validation (*Schutz et al.*, 2005). The off-nadir pointing option did not apply to this research, as we target the *entire* Arctic Ocean rather than a specific area within the Arctic Ocean. However, such maneuvers would have been useful for field campaigns (see, Chapter 6).

4.2.1 Measurement principle

The GLAS system provides the elevation of the Earth's surface with respect to a reference ellipsoid. GLAS transmits laser pulses (nominal pulse length 6 ns) that illuminates an area on the surface of the Earth, within its footprint, and gets reflected back to the instrument. The echo pulse is received by the telescope (see Fig. 4.1) and the analog detector. The transmitted and received pulses are digitized by a 1 GHz sampler and telemetered to the ground stations. These digitized pulses, called laser waveforms, are analyzed to calculate the pulse travel time and the *range vector*. The range is calculated from the centroid of the waveform. The centroid is determined from the peak location of the Gaussian curve that is fitted to the received waveform. *Yi et al.* (2003) reported an uncertainty of $\sim$ 2 cm in the range estimate due to this fitting procedure. Tropospheric corrections are then applied to the calculated range vector.

The Instrument Star Tracker (Fig. 4.1) provides the *direction* of the range vector through the Precision Attitude Determination (PAD) process and, the GPS tracking system provides the *position* of the GLAS system in space through the Precision Orbit Determination (POD) process. Finally, the elevation of the laser footprint on the Earth's surface is derived, with respect to a reference ellipsoid, from its position vector which is the sum of the two vectors: the position vector of the GLAS system and the range vector (*Schutz et al.*, 2005). A more detailed description of the procedure followed to determine the absolute elevation estimate is given by *Brenner et al.* (2003).

Since its launch, ICESat has provided a highly accurate three-dimensional view of the Earth. Due to its high accuracy and precision, ICESat data has been used to evaluate the SRTM (Shuttle Radar Topography Mission) DEM's (*Braun and Fotopoulos* (2007), *Bhang et al.* (2007)). *Carabajal and Harding* (2005) reported a vertical error in elevation of about 1 $\sim$ 4 cm over flat surfaces. This level of accuracy is acceptable for sea ice freeboard application. However, *Zwally et al.* (2002) reported an elevation uncertainty of $\sim$ 14 cm, which includes uncertainties in orbit determination (5 cm), attitude determination (7.5 cm), atmospheric delay (2 cm), atmospheric forward scattering (2 cm) and other unmodeled errors (1 cm). More details on ICESat accuracy and the validation experiments carried out, thus far, are provided in Chapter 6.

4.2.2 Data products

GLAS data products are generated by the ICESat Science Investigator-led Processing System (I-SIPS), located at NASA's Goddard Space Flight Center. The calibrated data are archived and freely available for users through the National Snow and Ice Data Center (NSIDC). NSIDC also distributes tools to decode (data are available in scaled integer binary format, big-endian (Unix) byte order format), visualize and analyze the data products, including subsetting spatial data sets. In this study, calibrated Level 2 GLAS data products were used. Level 2 implies that various Precision Orbit Determination (POD) and Precision Attitude Determination (PAD) corrections were applied to the Level 0 data (raw data transmitted to the ground). Table 4.1 contains the entire list of laser operational periods since the launch date.

Since 2003, GLAS data have been reprocessed numerous times resulting in a number of data releases. In this study, GLAS data release 428 (the most recent release available at this time) was used to derive Arctic sea ice freeboard heights. Since October 2008, release 29 data products were made available, but only for a few mission phases. A new release for all ICESat mission phases is made usually when improved processing algorithms are available that will increase the accuracy and reliability of the GLAS data. Many parameters are recomputed with the updated algorithms or computed for the first time. As an example, the ocean tide model that is applied to the GLAS elevations was changed from the GOT99.2 model to the TPX07.1 model (which is a more recent and more accurate ocean tide model; see Chapter 5). Other

Table 4.1: Laser operational period for ICESat/GLAS since mission launch

Laser	Number of days	Start date	End date
1	38	2003-02-20	2003-03-29
2A	55	2003-09-24	2003-11-18
2B	34	2004-02-17	2004-03-21
2C	35	2004-05-18	2004-06-21
3A	37	2004-10-03	2004-11-08
3B	36	2005-02-17	2005-03-24
3C	35	2005-05-20	2005-06-23
3D	35	2005-10-21	2005-11-24
3E	34	2006-02-22	2006-03-27
3F	33	2006-05-24	2006-06-26
3G	34	2006-10-25	2006-11-27
3H	34	2007-03-12	2007-04-14
3I	37	2007-10-02	2007-11-05
3J	34	2008-02-17	2008-03-21
3K	16	2008-10-04	2008-10-19
2D	23	2008-11-25	2008-12-17
2E	34	2009-03-09	2009-04-11

improvements between data releases include calibration of reflectivity estimates, corrections for waveform saturation and oscillator frequency.

The GLAS data products that are processed and distributed include global altimetry (GLA01), global atmosphere (GLA02), global backscatter (GLA07), global cloud and aerosol heights (GLA09 and GLA10), antarctic and greenland ice sheet altimetry (GLA12), ocean altimetry (GLA15) and land surface altimetry (GLA14). GLAS-13 sea ice altimetry data products for mission phases until March 2007 (Table 4.1) were analyzed in this study. This product provides sea ice elevations (laser footprint geolocation) along with the reflectance values, geophysical corrections, and instrument/atmospheric/saturation corrections and flags for the range measurements.

4.2.3 Data filtering

The GLAS system provides the elevation of the Earth's surface with respect to the Topex/Poseidon (T/P) reference ellipsoid. These elevations are obtained by removing the average range measurements within the footprint area from the orbital height of the satellite. Corrections for instrument and atmospheric biases and ocean tides have been applied to the GLAS-13 product prior to distribution. A number of other corrections were applied to the data products in order to obtain reliable, precise estimates and reduce the systematic errors and uncertainties for the sea ice freeboard retrieval. They are similar to the procedure followed by *Kwok et al.* (2006).

- Outliers are removed by checking the difference between the geoid height and the ellipsoidal height for each footprint. If the difference is more than 2 m (*i.e.*, +/- 2 m) then the data are removed from the analysis. This check is essential to remove the measurements from clouds or fog.

- Data are removed where the sea ice concentration value is less than 30 %. Sea ice concentration values were derived from NASA's gridded (12.5 km resolution) QuikSCAT backscatter data.

- i_reflctUcorr is the *reflectivity*, which is the ratio of the received energy and the transmitted energy. Data are rejected when the reflectivity is greater than 1 because the waveform distortion increases as the reflectivity increases.

- i_gainSet1064 is the *time-varying gain setting* and indicates the level of contamination by atmospheric scattering due to clouds, water vapor. A high time-varying gain setting implies low signal-to-noise ratio. In this study, data are rejected when the gain is above 30.

- i_SeaIceVar is an indicator of the level of non-Gaussian nature of the return waveform, *i.e., the standard deviation of the sea ice Gaussian fit.* A high i_SeaIceVar value indicates high uncertainty in the elevation estimate. Data are rejected when i_SeaIceVar is greater than 60.

- i_satElevCorr is the *saturation elevation correction*. This correction was introduced to mitigate the error caused by higher than predicted energy return, that occurred more frequently during the early mission phases (Laser 1, Laser 2A, Laser 2B, Laser 3A, and Laser 3B) (reported by NSIDC data release summary). A fraction of the waveforms become saturated due to the limited dynamic range of the instrument. Depending on the i_satCorrFlg (saturation correction flag) value (valid or invalid) i_satElevCorr will be applied. Otherwise, it might introduce an error of $\sim$ 1 m (NSIDC).

- i_ElvuseFlg is the *elevation use flag* that indicates the validity of the elevation measurements. Data are rejected when the flag is invalid.

- i_numPk indicates the *number of peaks* in the return pulse that is detected by the Gaussian fitting procedure. Data were rejected when more than two peaks were found.

4.3 Overview of the sea ice freeboard estimation procedure

Sea ice freeboard is calculated by subtracting the sea surface height from the sea ice surface height. The ICESat/GLAS system measures the ellipsoidal height of the snow surface overlying the sea ice medium, as the backscatter from a laser altimeter originates from the air-snow interface rather than the snow-ice interface as in the case of a radar altimeter (under cold and dry conditions). Therefore, the snow depth must be known in order to derive sea ice surface heights from ICESat. The next step is to determine the sea surface heights. There are two approaches to determine the sea surface height: (i) from ICESat observations from open water regions, referred to as 'lowest level' method in the literature and (ii) from a combination of models (this method was adapted in this study).

4.3.1 Sea ice freeboard from the 'lowest levels'

Sea ice freeboard from ERS

The method of deriving Arctic sea ice thickness from radar altimetry was first demonstrated by *Laxon et al.* (2003) and *Peacock and Laxon* (2004). They used eight years of data (1993-2001) from the 13.8-GHz radar altimeter on board the ERS-1 and ERS-2 satellites. The data covered a major portion of the permanent sea ice cover in the Beaufort, Chukchi, East Siberian, Kara, Laptev, Barents and Greenland Seas, 65°

N up to 81.5° N. The elevations over the ice surface and open water were derived by applying corrections for orbit, ocean tides and atmospheric delays. The sea surface height is determined from specular returns (they mainly originate from smooth surfaces such as leads and open water that are in between ice floes) in the radar backscatter and used as the reference for local sea level. The total ice freeboard is then obtained by subtracting the sea surface height from the sea ice surface elevations. Under cold and dry conditions, radar backscatter originates from the snow-ice interface (*Beaven et al.*, 1995). In this case, the total ice freeboard actually represents the sea ice freeboard. Fig. 4.3 shows the average winter Arctic sea ice thickness (October to March, 1993–2001). Ice thickness is computed from the ice freeboard by assuming hydrostatic equilibrium and fixed densities of sea ice and sea water. *Laxon et al.* (2003) concluded that the data revealed high interannual variability in the mean Arctic ice thickness, dominated mainly by the changes in the amount of summer melt.

Sea ice freeboard from ICESat

Kwok et al. (2007) used a similar procedure as *Laxon et al.* (2003), *i.e.*, the local sea surface was derived from the altimetry data. In their method, the tie points for sea surface estimates from the GLAS elevations were chosen using three criteria within every 25 km^2 area:

1. ICESat data from new openings/leads that were identified using SAR imagery.

2. When the reflectivities of the data points were lower than the background snow-covered sea ice *and* the ICESat elevation at that data point exceeded a certain deviation below that of the local mean surface.

3. Under the only condition that the ICESat elevation exceeded an expected de-

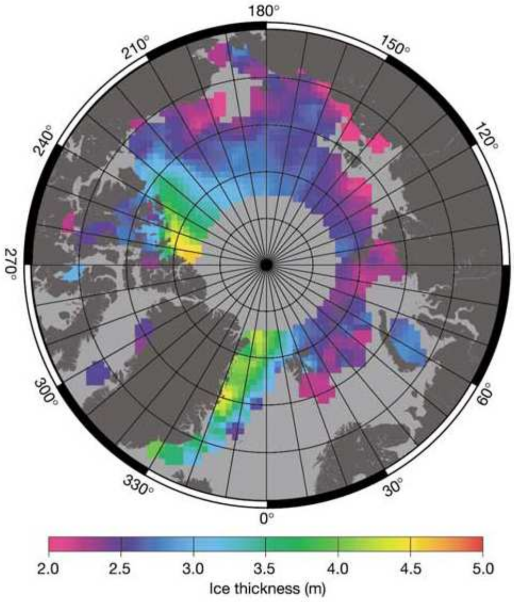

Figure 4.3: Average winter (October–March) Arctic sea ice thickness from 1993–2001 measured using ERS (*Laxon et al.*, 2003). No data available in the marginal seas or above 81.5° N (ERS latitudinal limit).

viation below that of a local mean surface.

The tie points are used to derive the sea surface heights that are removed from the snow/sea ice surface heights to get the total freeboard. The limitations are that it depends on the availability of new openings in every 25 km^2 area. Otherwise, the sea surface will be tilted due to variations in short length-scale geoid, tides and mean dynamic topography. Also, the specular returns from open water are limited by the dynamic range in the instrument (see section 4.2.3) and sometimes are rejected as saturated data points. Therefore, the lowest levels are not truly from open water areas; instead, are from recently refrozen thin ice or rough sea surface.

Forsberg and Skourup (2005) derived sea ice freeboards from ICESat data in the Arctic Ocean using the 'lowest level' method. They determined the 'lowest level' surface, a representation of the local sea level, from the geoid-reduced ICESat elevations (at 10 km length scales) which was used in the sea ice freeboard retrieval. *Kurtz et al.* (2008) also used the 'lowest level' method similar to *Forsberg and Skourup* (2005) at different length scales (50 km, 25 km) to determine the sea ice freeboards in the Arctic.

4.4 Sea ice freeboard from geodetic models

The total freeboard (sea ice + snow) is calculated by subtracting the sea surface height from the snow surface height measured by the laser altimeter ICESat.

$$F = E - SSH, \tag{4.2}$$

where, F is the sea ice plus snow freeboard, E is the ellipsoidal height of the snow surface, and SSH is the instantaneous sea surface height at the ICESat footprint location. Sea surface height, in this study, is defined as the sum of the geoid (N), ocean tides (T), mean dynamic topography (MDT), and atmospheric pressure loading effect (IBE). The basic equation for sea ice freeboard height estimation from altimetry data products using geodetic and oceanographic models is, therefore (Fig. 4.4),

$$F = E - N - T - MDT - S - IBE - e, \tag{4.3}$$

where, F is the ice freeboard, S is the snow thickness, e is sum of errors in each measurement. The procedure for calculating each parameter in Eqn. 4.3 is discussed in the following sections.

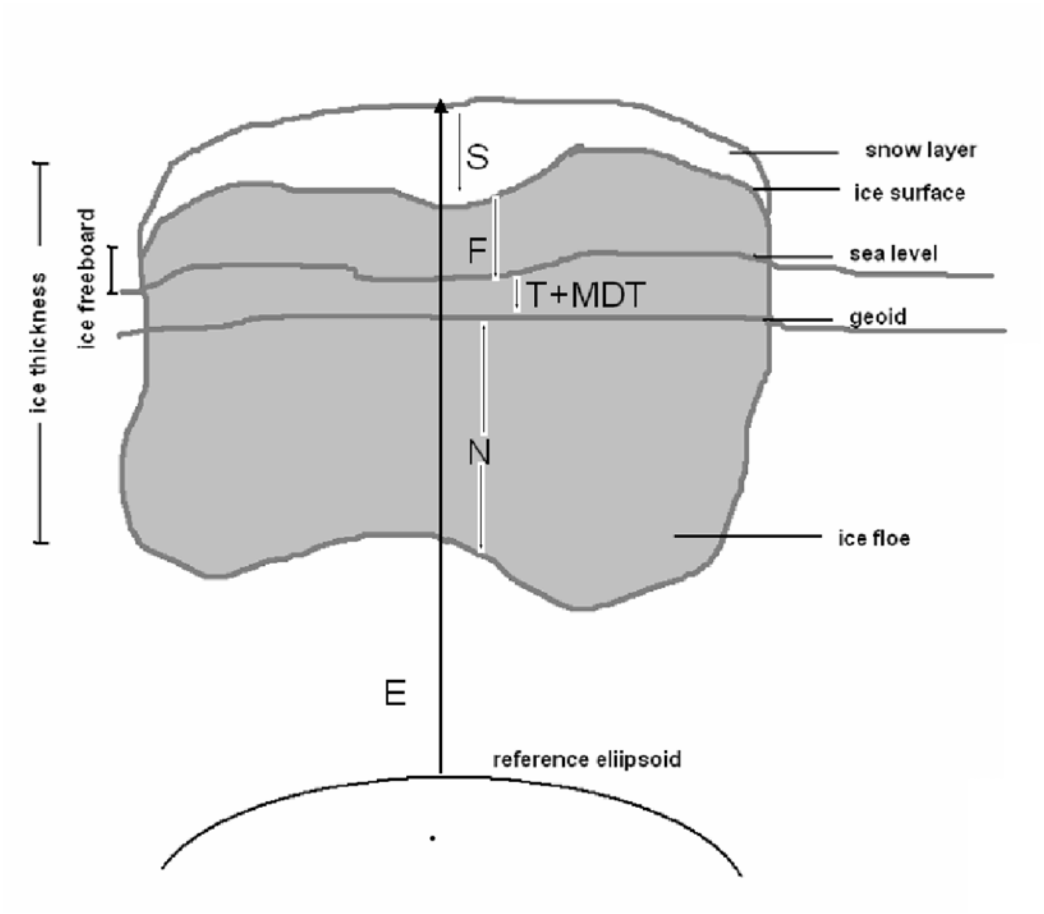

Figure 4.4: Sea ice freeboard height estimation principle. F is the sea ice freeboard, E is the ellipsoidal height of snow surface, N is the geoid undulation, T and MDT are the ocean tides and mean dynamic topography, S is the snow thickness.

4.4.1 Sea ice surface heights

ICESat/GLAS geolocated GLA-13 products contain the geodetic latitude, longitude and the height of the snow or ice surface above a reference ellipsoid. ICESat uses the same reference ellipsoid as the TOPEX/Poseidon and Jason-1 satellites. The elevations with respect to the T/P ellipsoid need to be transformed into elevations with respect to the WGS-84, in order to maintain a consistent reference system in the sea ice freeboard retrieval procedure (*e.g.*, the geoid model used in this study is referenced to the WGS-84 ellipsoid). The differences between the T/P ellipsoid and the WGS-84 ellipsoid are summarized in Table 4.2 below.

Table 4.2: Topex/Poseidon ellipsoid and the WGS-84 ellipsoid parameters

Parameter	T/P	WGS-84
Equatorial radius (a)	6378136.300000	6378137.000000
Polar radius (b)	6356751.600563	6356752.314245
Reciprocal flattening (1/f)	298.25700000	298.25722356
Eccentricity (e)	0.081819221456	0.081819190843

Based on these parameters, the T/P ellipsoid is $\sim$ 70 cm lower than the WGS-84 ellipsoid. Therefore, the GLAS elevations tend to be higher than the elevations measured with respect to the WGS-84 system. The ellipsoidal differences cause only a few centimeters of displacement in the geodetic latitude and longitude that is well below the GLAS accuracy in geolocation and the GLAS footprint size. Therefore, the geolocation values need not be transformed. For a particular latitude, the change in elevation between ellipsoids can then be approximated using the empirically derived formula (implemented by NSIDC),

$$\delta_h = h_2 - h1 = -((a_2) * cos(\phi)^2 + (b_2 - b1) * sin(\phi)^2 \tag{4.4}$$

where ϕ is latitude, h_1 and h_2 are elevations for ellipsoids 1 and 2 (T/P and WGS-84), respectively, a_1 and a_2 are the equatorial radii of ellipsoids 1 and 2, respectively, and b_1 and b_2 are the polar radii of ellipsoids 1 and 2, respectively.

NSIDC distributes ITT Visual Information Solutions (ITT VIS) IDL (Interactive Data Language) tools to perform the elevation transformation between the two ellipsoids. The elevation conversion equation (Eqn. 4.4) shows that the transformation is a function of latitude – 70 cm at the equator and 71.3682 cm at the poles. The NSIDC tool was implemented in this study to calculate the transformation values for one ICESat mission phase. As the study area is above the Arctic Circle, the transformation values only ranged from 71.10 cm to 71.36 cm. Since the difference ($\sim$ 0.25 cm) is well below the ICESat/GLAS elevation precision ($\sim$ 2 cm, *Zwally et al.* (2002)), a fixed value of 71 cm was used in this study to perform the transformation. That is, 71 cm was removed from GLAS elevations to reference them to the WGS-84 ellipsoid. The next step is, as mentioned earlier, the determination of sea surface height.

4.4.2 Geoid Heights

Geoid is an equipotential surface of the gravity field, sometimes approximated as the mean sea level. From Fig. 4.5, it can be seen that the geoid height (measured with respect to the WGS-84 ellipsoid) in the Arctic Ocean ranges from -30 m (near the Canadian Archipelago) to 66 m (near the Fram Strait). It is the dominant signal in the determination of SSH.

The different geoid models available for the region of study include ArcGP, Arctic Gravity Project (*Forsberg and Kenyon*, 2004), and EIGEN-GL04c, GRACE-LAGEOS

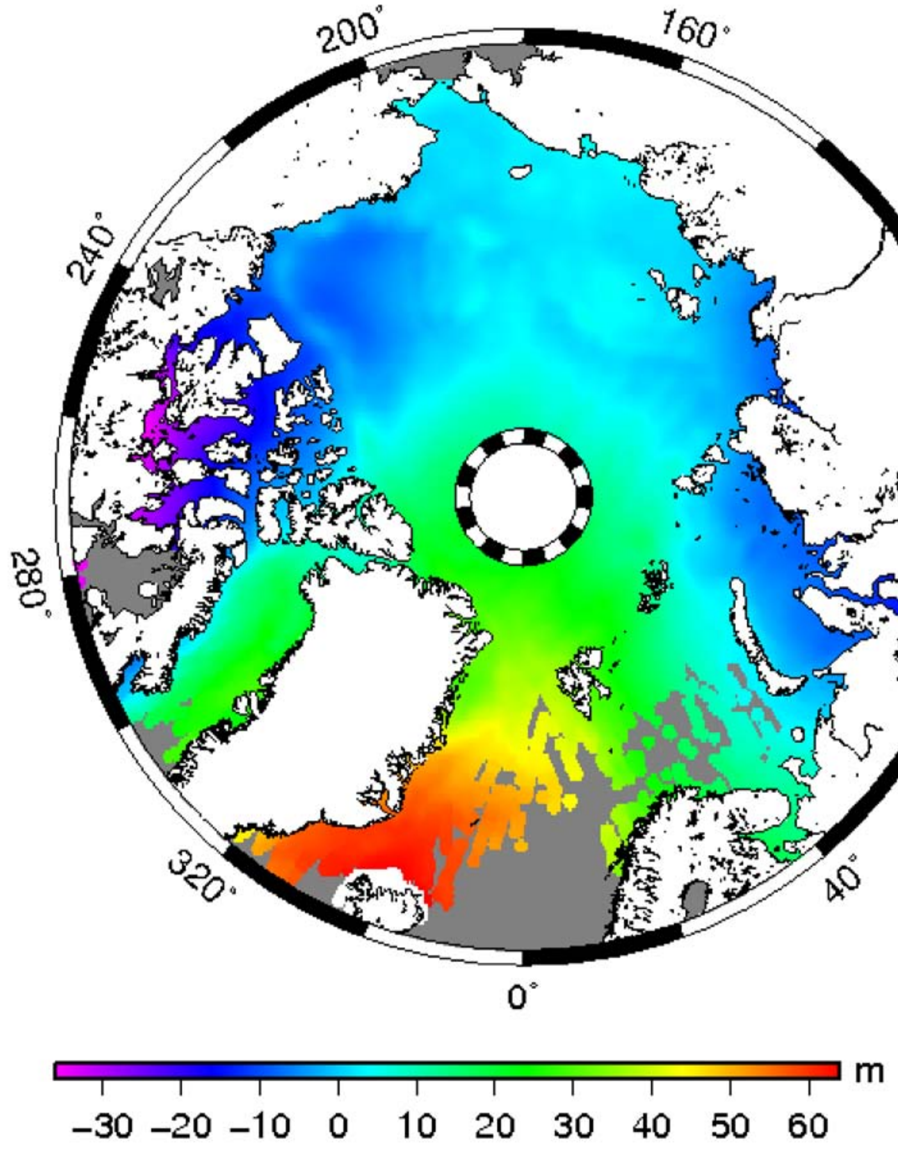

Figure 4.5: The geoid heights (N) at each ICESat footprint location (February 2005 epoch) obtained from the EIGEN-GL04c model. N ranges from -30 m (near the Canadian Archipelago) to 66 m (near the Fram Strait).

2004 Combination (*Foerste et al.*, 2008) models. The Arctic Gravity Project, since 1998, collected gravity field data that were available for the Arctic region, north of 64° N. *Forsberg et al.* (2007) summarized the list of data that were compiled in the ArcGP study. (i) Airborne gravity data – over Greenland collected by US Naval Research Laboratory, near coastal regions around Greenland, Svalbard and parts of Canada collected by Denmark-Norway, Fram Strait and north of Greenland collected by Germany, and Russian survey data from north of Frans Josef Land. (ii) Surface gravity data – Gravity data collected by Canada (Natural Resources Canada), Scandinavia, US, Germany, and Russia on land, sea, and sea ice. (iii) Submarine data – SCICEX US gravity data. (iv) Satellite altimetry – Retracked ERS altimetry gravity anomalies that filled a major gap in the Ocean, north of Siberia, as well as ICESat data (see *Forsberg and Skourup* (2005)).

Since the launch of GRACE (*Tapley et al.*, 2004) and the CHAllenging Minisatellite Payload (CHAMP), a number of new generation global gravity field models were developed. The EIGEN-GL04S1, a satellite-only model (GRACE-LAGEOS) complete to degree and order 150, was combined with the surface gravity (altimetry and gravimetry) data to compute the new high-resolution more accurate global gravity field model, EIGEN-GL04c (*Foerste et al.*, 2008). The newer surface gravity data sets in the Arctic (ArcGP data sets as mentioned above), Antarctica and North America, and a new mean sea surface height model from altimetry processing developed by GFZ were used in the development of the EIGEN-GL04c model. The shortest wavelength of this model is 110 km and it is complete to degree and order 360 in spherical harmonic coefficients (*Foerste et al.*, 2008). The authors state that the long- to medium-wavelength ($\sim$ 400 km) model accuracy was improved by one order of magnitude ($\sim$ 3 cm) in geoid heights when compared with models from pre-CHAMP generation and that the model accuracy at its full-spatial resolution was estimated as $\sim$ 15 cm. In this study, the EIGEN-GL04c model developed by Geo Forschungs Zentrum (GFZ) was used in the sea ice freeboard retrieval procedure (Fig. 4.5).

ICESat/GLAS data products provide the geoid height for each footprint (not applied to the data) using the Earth Gravitational Model 1996 (EGM96 model), which is a pre-CHAMP generation model. Therefore, in this study, the geoid height was calculated for each footprint using the EIGEN-GL04c model. The permanent-tide reference system in this model is the tide-free system. But a mean-tide system is more suitable for oceanographic applications (*Hughes and Bingham*, 2008). Therefore, the geoid heights were transformed from a tide-free permanent tide system into a mean-tide system. The procedure is explained in more detail in the following section.

Permanent tides in Geoid models

The long-term average of the tide-generating potentials (ocean and Earth tides) for the Sun and the Moon are not *zero* because of the permanent deformation caused by these potentials. Conventionally, in the definition of the geoid, the periodic component of these potentials are averaged out. The non-zero average results in an increase in the Earth's equatorial bulge. This permanent deformation is treated in three different ways when calculating the 3-D positions and the gravity field – mean-tide, tide-free and zero-tide. These concepts are discussed in detail in *Ekman* (1989). The pros and cons of each of these systems are discussed in *Makinen and Ihde* (2008). The permanent effect is either retained or removed from the computations of the geoid and the topography.

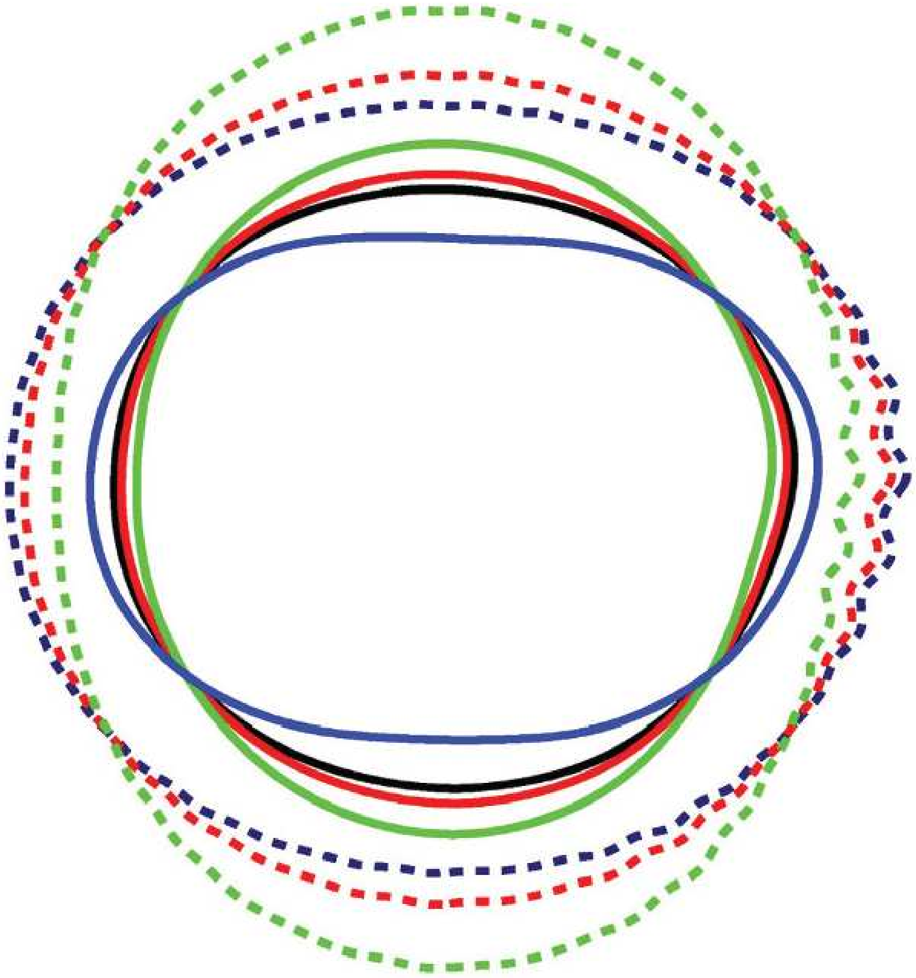

Figure 4.6: Schematic illustration of different tidal concepts for the crust/topography (dashed lines) and the geoid (solid lines), as sections in a meridional plane. The crusts are from largest to smallest flattening: mean, conventional tide-free, fluid tide-free (not discussed here). The geoids are from largest to smallest flattening:mean, zero, conventional tide-free, fluid tide-free (*Makinen and Ihde*, 2008).

1. *Tide-free system* – In this system, the representation is a tide-free crust (topography) over a tide-free geoid (Fig. 4.6). In other words, the effect of permanent deformation is removed from both the topography and the potential. As a result, the equatorial bulge is allowed to relax as a response to the absence of the extra potential. However, this is only a theoretical construct as the extent of the relaxation to such a perturbation is not known and therefore assumptions have to be made (*Hughes and Bingham*, 2008). This system is the present realization for 3-D positioning (*Makinen and Ihde*, 2008).

2. *Zero-tide system* – In this system, the representation is a mean crust over a zero-tide geoid. That is, the tide-generating potential is removed from the potential and retained in the topography. In current practice, this system is widely used in fields related to absolute gravity.

3. *Mean-tide system* – In this system, the effect of the permanent deformation is retained in the shape of the Earth (topography and the geoid). Therefore, the potential field in this system contains not only the masses of the Earth but also the time-average of the tide-generating potential. Because the Ocean settles down according to the total potential it can sense, irrespective of where it originates from, the mean-tide system is appropriate for oceanographic applications. Hence, this system was recommended to be used in calculations with T/P GDRs (Geophysical Data Records) to get sea surface with respect to a mean geoid (*Rapp et al.* (1991)). Mean sea level by definition is in the mean-tide system. Hence, the EIGEN-GL04c model geoid height have to be transformed from tide-free to mean-tide system.

The transformation from a tide-free permanent tide system to a mean-tide system is given by (*Ekman* (1989), and *Lemoine et al.* (1998)),

$$N_m = N_{tf} + (1 + k)(9.9 - 29.6 * sin^2\phi)cm, \tag{4.5}$$

where N_m is the geoid height in the mean-tide system, N_{tf} is the geoid height in the tide-free system, k is the Love number taken as 0.3 (see Chapter 11 in *Lemoine et al.* (1998)) and ϕ is the geodetic latitude.

The transformation was carried out for geoid heights at each ICESat/GLAS footprint. Fig. 4.7 shows the difference between the two permanent tide systems in the study area, approximately from -29 cm to -17 cm. The differences are significantly large and illustrates the importance of adopting the correct reference system for this study.

4.4.3 Tides

Ocean tides and ocean loading tides are removed from the sea ice surface height in order to estimate the sea ice freeboard. GLAS-13 data products contain sea ice surface heights where the ocean and loading tides were already accounted for. NSIDC uses a GOT0.99 ocean and loading tide model for release 28 data. However, in this study, it was found that the AOTIM-5 model was the best available model for the Arctic Ocean. Hence, it was used in the sea ice freeboard retrieval algorithm to calculate ocean tides (see Chapter 5 for more details). Loading tides, since it is a small signal which does not change significantly between tide models, were not replaced with the AOTIM-5 model. The difference was insignificant for this study. The average amplitude of ocean tides in the Arctic Ocean is about 20 cm with extreme values of +/- 50 cm in coastal areas (Fig. 4.8).

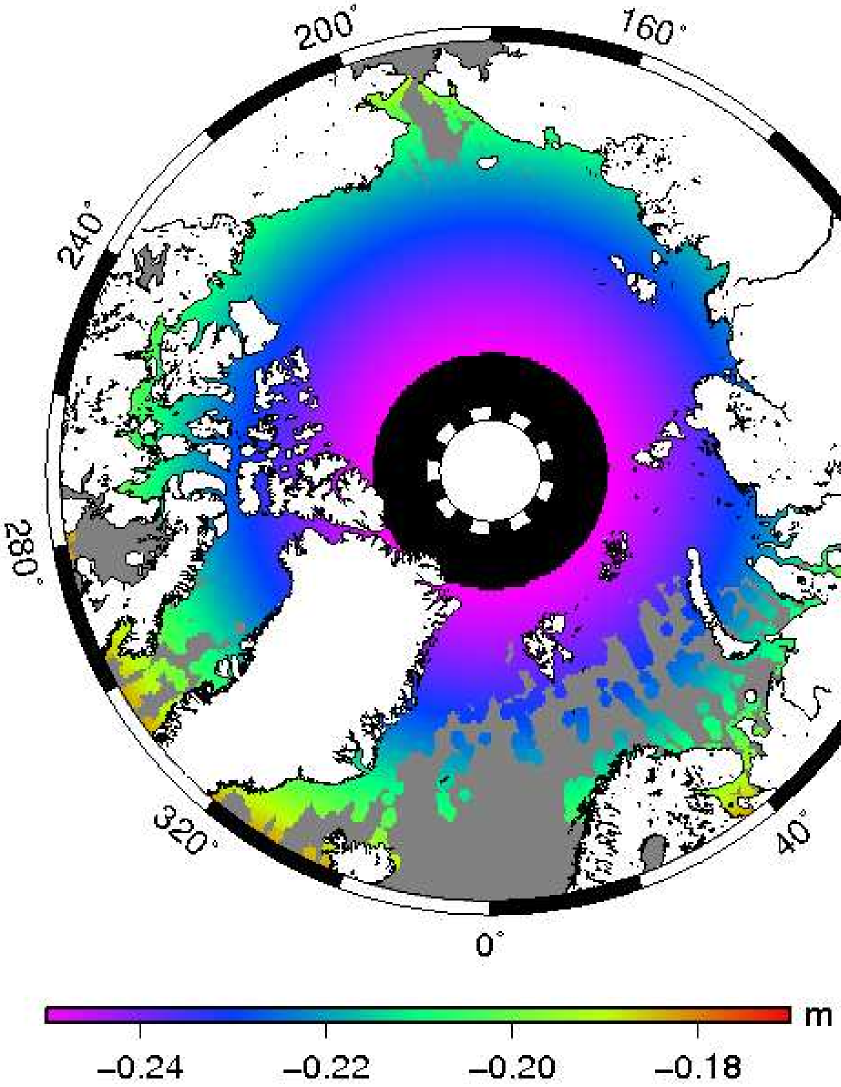

Figure 4.7: The permanent-tide transformation correction (from tide-free to mean-tide) for geoid heights at each ICESat footprint location (November 2005 epoch). The corrections range from −29 cm to −17 cm with larger values towards the poles.

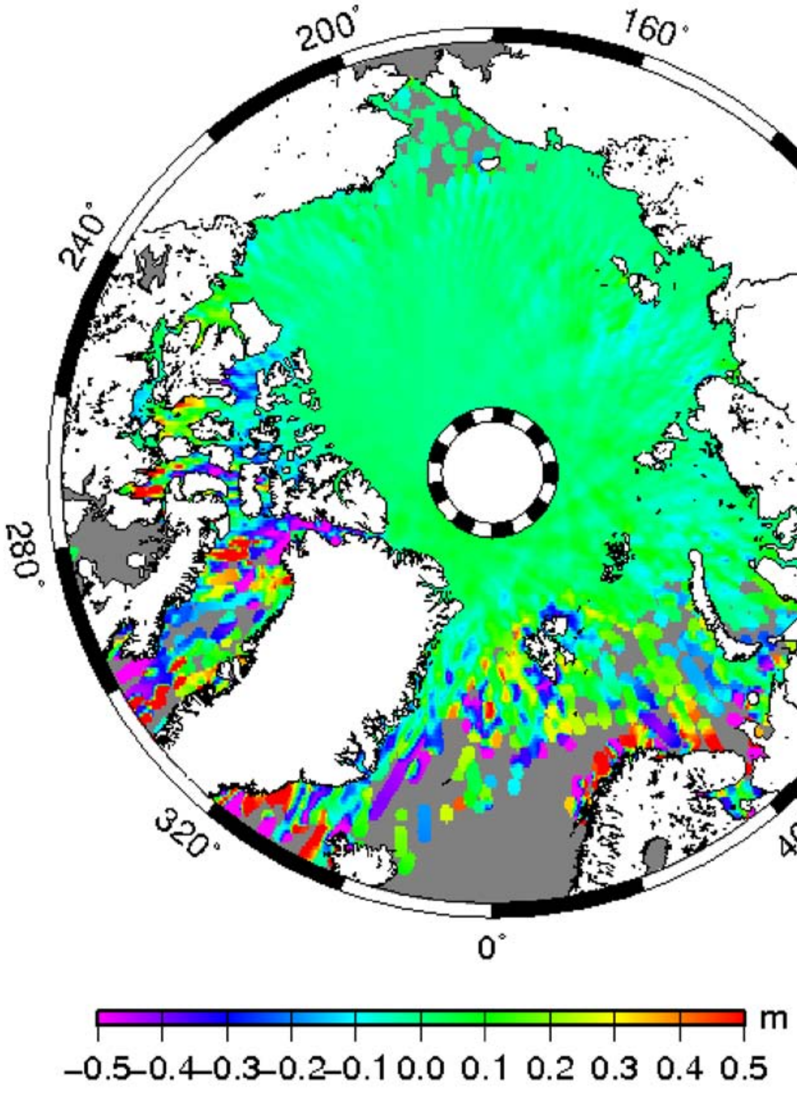

Figure 4.8: Ocean tides at each ICESat footprint (October 2004 epoch) derived using the AOTIM-5 model. The tide values range from -30 cm to +30 cm in the Arctic Ocean. Larger tide values are seen near the marginal seas.

4.4.4 Mean Dynamic Topography

Ocean dynamic topography is defined as the height of the sea surface above a gravity equipotential surface (*e.g.*, the geoid). The ocean surface deviates from the geoid (which is the ocean surface at rest) due to the forcing from winds, geostrophic surface currents, ocean circulation, etc. Mean dynamic topography (MDT) is a long-term average of the sea surface that excludes short-term changes, such as ocean tides or atmospheric pressure effects. It mainly represents the large-scale thermohaline ocean circulation (driven by temperature and salinity gradients), and is an important signal for climate studies as it moderates the Earth's climate. In the Arctic Ocean, MDT has a range of up to $\sim$ 60 cm. For example, in the University of Washington MDT model (UW), it ranges from –30 cm (near the Fram Straight) up to + 30 cm (in the Beaufort gyre) (Fig. 4.9). The major signal is around the Beaufort polar anticyclonic gyre. In the northern hemisphere, anticyclonic gyres have a convergent motion due to the Coriolis effect (the opposite is true for cyclonic gyres) and, therefore, a large positive MDT is seen near the Beaufort gyre (Fig. 4.9). The difference between the dynamic topography and mean dynamic topography is known as the sea level anomaly (SLA). It is an important parameter for studying phenomena such as the *El Ninõ*. Satellite altimetry data have been used to derive estimates of SLAs and, recently, even to predict SLA's from altimetry data (*Niedzielski and Kosek*, 2009).

One of the simple approaches to determine the MDT is to calculate the dynamic heights using the Levitus climatology of temperature and salinity (*Levitus*, 1982). Dynamic height is the difference between two pressure surfaces, p_1 and p_2, usually

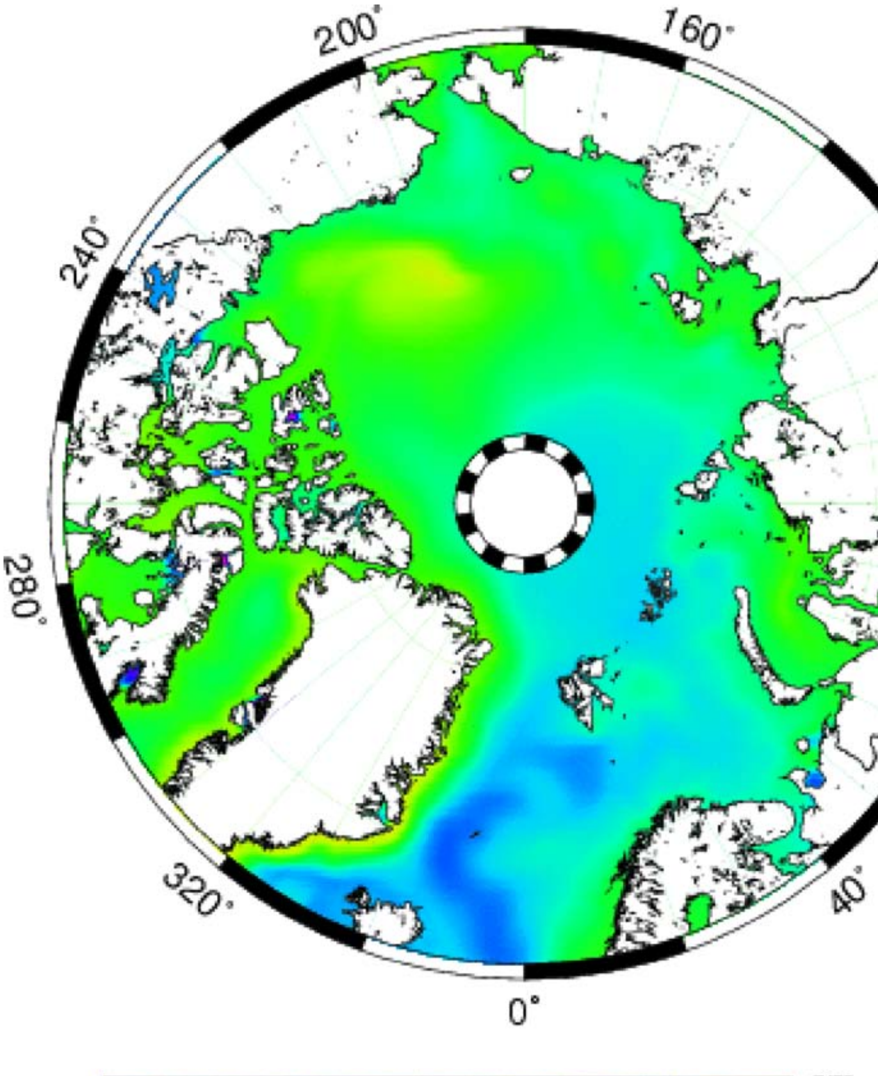

Figure 4.9: The mean dynamic topography (MDT) in the Arctic Ocean obtained from the University of Washington model (UW) (*Steele et al.*, 2004). A larger MDT signal (+30 cm) is seen around the anticyclonic Beaufort gyre.

measured with respect to a zero-level surface (z = 0),

$$D(p_1, p_2) = \int_{p_1}^{p_2} \alpha dp, \tag{4.6}$$

where α is the specific volume (density) distribution within the water column. The density is measured *in situ* by measuring the temperature and salinity profiles as a function of pressure (depth). Comparing dynamic heights at two points is equivalent to comparing their horizontal pressure gradients (*Knauss*, 1978). Levitus estimated a dynamic height of up to 2 m in the equatorial oceans.

However, even under barotropic conditions (where the isobaric surfaces are parallel to the isopycnic surfaces) the dynamic heights and dynamic topography may not be equivalent because the gravitational equipotential surface that is used as a reference in dynamic topography may not be parallel to the isobaric or isopycnic surface. Refinements were made to the Levitus method by applying an inverse model with dynamical constraints to derive the barotropic signal in *LeGrand et al.* (1998). Near-surface drift velocities have also been used to derive MDT (*Niiler et al.*, 2003). However, these methods are limited by the inhomogeneous hydrographic data. Hydrographic data, drifter velocities and coincident altimeter measurements were combined in a number of studies (*Rio and Hernandez* (2004), *LeGrand et al.* (2003)) to determine the MDT. In order to overcome the limitations of inhomogeneous spatial and temporal data distribution, *Bingham and Haines* (2006) derived MDT by assimilating hydrographic data into the Ocean General Circulation Model (forcing the model with realistic winds, fluxes of heat and freshwater), thereby producing uniform sampling for any required time period. *Bingham and Haines* (2006) concluded that this method offers the most effective way of combining observations and the physical understanding of the ocean.

Vossepoel (2007) evaluated the accuracy of a number of MDT models based on observations (such as altimetry and hydrographic data) and numerical modeling. The estimated RMS difference between five different observational MDT models was ~ 10 cm at a spatial scale of 167 km. The RMS differences between modeled and observed MDT were ~ 8.8 cm (at a spatial scale of 167 km). Besides quantifying the mutual differences, the regions of largest uncertainties were also identified. A similar study is needed for regional analysis in the Arctic Ocean.

In the ArcGICE project (*Forsberg et al.*, 2007), four oceanographic MDT models were compared with the MDT derived from altimetry: MICOM (Miami Isopycnic Coordinate Ocean Model, *Bleck et al.* (1992)), OCCAM (Ocean Circulation and Climate Advanced Modeling Project developed by Southampton Oceanographic Center in UK), PIPS (Polar Ice Prediction System developed by the US Naval Postgraduate School) and UW (University of Washington, *Steele et al.* (2004)). It was found that the models differ from each other, probably due to the differences in the ice-ocean interaction physics that was assumed or the forcing parameters. The differences were of the order of 50 cm, which is comparable to the MDT signal and the freeboard signal itself. Therefore, MDT is the major source of error and uncertainty in this method of sea ice freeboard retrieval using models. However, these errors are expected to improve greatly with the new generation of MDT models. When these MDT models were compared with the altimetry-based MDT in the ArcGICE study, the UW model showed the best agreement. In this study, therefore, the UW model was used to derive MDT for each ICESat/GLAS footprint in the sea ice freeboard retrieval algorithm.

Outlook As the modeling of mean dynamic topography continue to improve, the best modeling can be achieved by assimilating all available hydrographic data, altimetric data and gravimetric data (*e.g.*, *Maximenko and Niiler* (2004)) rather than based on pure hydrodynamics and air-ice-ocean physics, *i.e.*, by creating a hybrid model (similar to ocean tide models). However, deriving an accurate model for the Arctic Ocean based on this method can still be a challenge due to limitations in hydrographic data availability for this region. Since, the geoid model has improved in accuracy for the Arctic Ocean (see section 4.4.2), altimetry data can be used to derive observational MDT for this region to be assimilated in the hybrid model. *Forsberg et al.* (2007) (ArcGICE project) demonstrated the possibility of deriving MDT from ERS and ICESat altimetry data. With the launch of European Space Agency (ESA) Gravity field and steady-state Ocean Circulation Explorer (GOCE) satellite mission, the geoid and MDT are expected to improve immensely. The main objective of GOCE is to determine the geoid with an accuracy of 1–2 cm at 100 km spatial resolution and, to determine the mean ocean circulation (*Drinkwater et al.*, 2007).

4.4.5 Inverse Barometric Effect

The inverse barometric effect is the hydrostatic response of the sea surface to the changes in atmospheric pressure (or atmospheric loading). In general, for an increase in the atmospheric pressure of ~1 mbar, the sea surface is depressed by ~1 cm. The surface pressure in the Arctic Ocean is, spatially, a smooth surface ranging from 1006 mbar when there is low pressure up to 1020 mbar when there is high pressure (Fig. 4.10). The IBE corrections are only of the order of 15 – 20 cm (1 cm/mbar).

GLAS-13 data products also distribute the atmospheric pressure values at the Earth's surface (sea surface), that were derived from the National Center for Environmental Prediction (NCEP) global numerical weather analysis fields. These fields

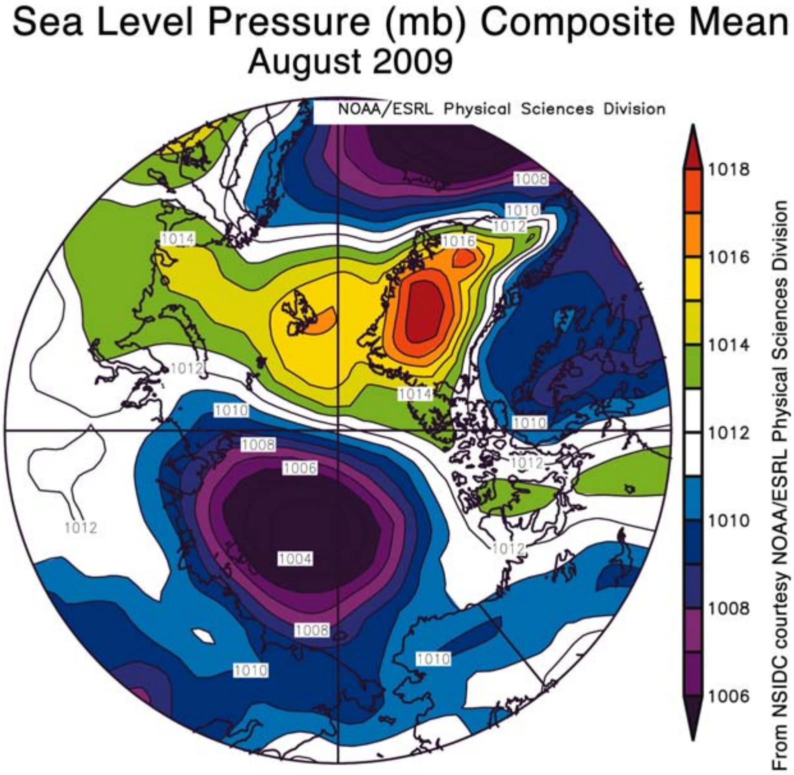

Figure 4.10: The sea level pressure (in mbar) variability in the Arctic Ocean obtained from the Physical Sciences Division, Earth System Research Laboratory, NOAA, Boulder, Colorado.

are on a 2.5° × 2.5° grid every 6 hours that includes temperature, geopotential height, surface pressure and relative humidity at standard atmospheric pressure levels. Although the NCEP analysis fields provide surface pressure, their accuracies were not acceptable. Hence, the GLAS team (*Herring and Quinn* (2001), Algorithm Theoretical Basis Document) developed a procedure to reduce the upper atmospheric NCEP fields down to the surface height (GLAS height at that location) by assuming a horizontally stratified atmosphere, that is in hydrostatic equilibrium. The pressure is related to height by the hydrostatic equation,

$$\partial p = g(Z)\rho(Z)\partial Z, \tag{4.7}$$

where Z is geometric height, p is pressure, g is gravity, and ρ is density.

The correction for the inverse barometric effect (in mm) can be computed using the linear formula (from (*AVISO*, 2008) Handbook),

$$IBE = -9.948 * (P_{atm} - P), \tag{4.8}$$

where P_{atm} is the instantaneous surface atmospheric pressure, P is the time-varying mean of the global surface atmospheric pressure over the oceans (taken as 1013.3 mbar), and 9.948 is a scale factor (in mm/mbar) that was adapted from *Wunsch* (1972). According to this equation, a 1 mbar error in the sea level pressure will lead to a 10 mm error in the IBE correction.

In this study, the IBE correction was calculated using a similar formula as above (Eqn. 4.8), where the constant was replaced by 11.2 mm/mbar. This constant was computed by *Kwok et al.* (2006) for the Arctic region by analyzing the repeat ICESat tracks (Fig. 4.11). The constant is slightly higher than the AVISO value and the ideal 1 cm/mbar value. *Kwok et al.* (2006) attribute a part of this difference to the response of sea level to wind stress (*Fu and Pihos*, 1994), *i.e.*, atmospheric loading contains two components – surface pressure and wind stress. Because the effect of the wind stress on the ice-covered sea level is not understood in detail, it is not possible to separate these two signals.

In the ArcGICE project (*Forsberg et al.*, 2007), 11.2 mm/mbar was used as the constant to determine the IBE correction. The same procedure was followed in this study as well. The sea level pressure was linearly interpolated from the NCEP reanalysis fields for each ICESat/GLAS footprint and the IBE correction was calculated using the procedure described above. The IBE correction is important for two reasons: (i) the spatial variations lead to a correction of magnitude ~ 15 cm which is significant for this application, and (ii) the temporal variations in the atmospheric pressure lead to variations in the GLAS measured sea (ice) surface heights between different ICESat tracks and, therefore, this correction reduces those variances.

4.4.6 Snow depth

ICESat/GLAS is a laser sensor and does not penetrate through the snow layer. However, under cold and dry conditions, snow layer becomes transparent to radar (*Onstott*, 1992). Radar can penetrate through several decimeters into the low-salinity multi-year ice (MYI) at just $-5\,^{\circ}$C (at $> -5\,^{\circ}$C, melting occurs. The presence of water decreases the penetration depth). In contrast, over a saline new or first-year ice (FYI) the penetration depth is only few centimeters (*Hallikainen and Winebrenner*, 1992). Snow depth must be known in order to convert the ICESat-derived total freeboard into sea ice freeboard. Besides snow thickness, snow density must also be

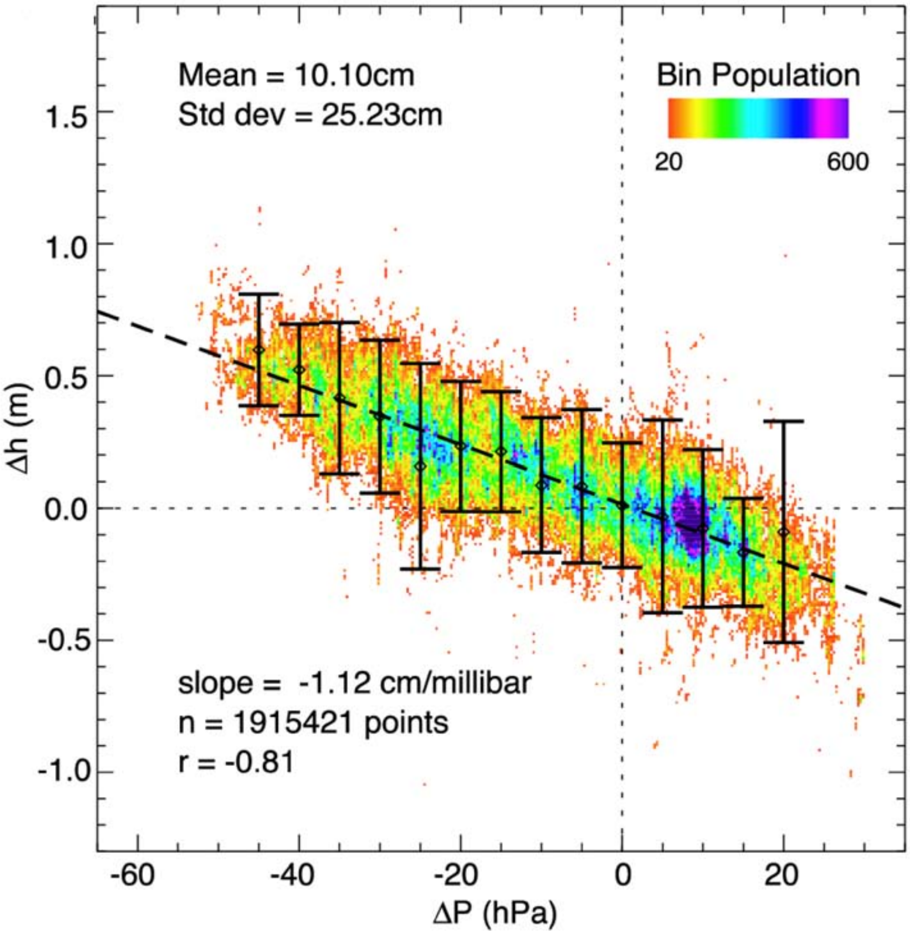

Figure 4.11: The regression of ICESat elevation differences (Δh) and sea level pressure differences (ΔP) (*Kwok et al.*, 2006). The differences are between two 8-day exact repeat cycles during February-March 2003 ICESat mission phase.

known in order to derive sea ice thickness from sea ice freeboard (see section 4.4.7).

Factors that affect the snow distribution on sea ice are ambient temperature, precipitation, wind direction, thermodynamics, ice type or ice surface topography, geographic location and season. The precipitation is higher in the Antarctic than in the Arctic due to the presence of nearby moisture source. Hence, thicker snow is observed over Antarctic sea ice. Strong winds prevailing over sea ice redistribute the snow depending on ice type or surface roughness. This results in the formation of sastrugi (compressed and deformed snow) and balcan dunes on snow (*Massom et al.*, 2001). Snow on FYI is easily redistribute by winds due to smaller surface roughness on FYI. Deformed ice types, such as MYI and pressure ridges, create snow catchment structures, hence thick snow is observed over these ice types. Thus, addition of snow increases the surface elevation and decreases the ice surface roughness.

Snow cover observations Basin-scale snow cover observations are very limited in the Arctic. *Warren et al.* (1999) and *Massom et al.* (2001) compiled all in situ observations of snow depth in the Arctic and Antarctic. These observations, however, have poor spatial and temporal resolution. *Warren et al.* (1999) used a statistical method to model snow climatology from in situ observations. A two-dimensional quadratic function was fitted to all data for a particular month, irrespective of the year in order to represent the geographical and seasonal variation of snow depth. These data may not be representative of the present day conditions. *Iacozza and Barber* (1999) used a geostatistical technique known as a variogram, to model the statistical distribution of snow depth. The model provided a good representation of variability of snow depth with ice type. Remote sensing techniques can provide large-scale snow cover observations over longer time periods. However, there are no existing algorithms to derive snow depth with reasonable accuracy (better than 5 cm). *Chang and Chiu* (1990) derived snow depth from Scanning Multi-channel Microwave Radiometer (SMMR) data at 25 km resolution. *Bindschadler et al.* (2005) estimated the snow accumulation from satellite laser altimetry. They used passive microwave data to identify the extent and timing of new snow on the Antarctic ice sheets, and used cross-over elevation measurements from GLAS/ICESat to estimate the amount of new snow over ice sheets. The total snow depth over sea ice, however, cannot be discerned from this technique. *Comiso et al.* (2003) used the measured radiances from Advanced Microwave Scanning Radiometer for EOS (AMSR-E) data to derive snow depth among other parameters in the Arctic and the Antarctic.

New missions, ICESat-2 and Cryosat-2, are expected to be launched in the next few years. Co-incident laser and radar altimeter measurements have the potential to provide snow depth in the Arctic at basin-length scales under cold, dry conditions. The laser altimeter measures the elevation of the air-snow interface due to the high optical reflectivity of the snow surface, while the radar altimeter measures the elevation of the snow-ice interface under cold, dry conditions. When the snow is wet, the penetration depth of the radar pulse through the snow layer decreases and backscatter originates from the snow medium. *Leuschen et al.* (2008) carried out a similar study to estimate snow depth in the Antarctic, but with airborne data. Data collected with Applied Physics Laboratory's Delay-Doppler Phase Monopulse (D2P) radar and NASAs Airborne Topographic Mapper (ATM) scanning lidar were used in their study.

Kwok and Cunningham (2008) developed a new procedure to construct daily fields of snow depth on a 25 km grid using the climatological and meteorological data.

The daily actual snowfall data (snow water equivalent) from European Centre for Medium-Range Weather Forecasts (ECMWF) products were combined with the modified seasonal snow density from *Warren et al.* (1999) to construct the daily Arctic snow depth. The detail procedure is described in *Kwok and Cunningham* (2008). Initial conditions of snow cover over MYI are obtained from *Warren et al.* (1999). Daily snow accumulation (constrained by temperature conditions and concentration) from ECMWF SWE is done on a 25 km grid beginning September 15, along the drift trajectories of sea ice constructed from AMSR-E sea ice motion fields (in order to keep track of the advection of the sea ice parcels and the corresponding snow cover on top). The sources of error (limitations) are from the frost deposition, snow sublimation and wind redistribution because these factors were not considered in this procedure. Other sources of error in their snow depth estimation procedure are discussed below.

Fig. 4.12 shows the constructed snow depth by *Kwok and Cunningham* (2008) for the ICESat mission phases of October 2005 and February 2006. Using a spatial mask for MYI and FYI ice fractions, the snow cover within those regions were separated. The mean snow depth over MYI was – 29.3 cm (σ 5.7 cm) in October 2005; 45.0 cm (σ 5.6 cm) during February 2006; over FYI – 13.0 (σ 9.1 cm) during October 2005; 29.1 cm (σ 8.2 cm) during February 2006.

It can be noted that the standard deviation of the constructed snow depths are low, $\sim$ 5.5 cm over MYI cover regions and $\sim$ 8.5 cm over FYI cover regions. This is well below the accuracy of ICESat/GLAS elevation that have uncertainties of about $\sim$ 14 cm over the 70 m footprint area (*Zwally et al.*, 2002). Moreover, the accuracy of the Kwok method is probably also on the same level as, or more than, the standard deviation. This is because there is a number of sources of error in their procedure:

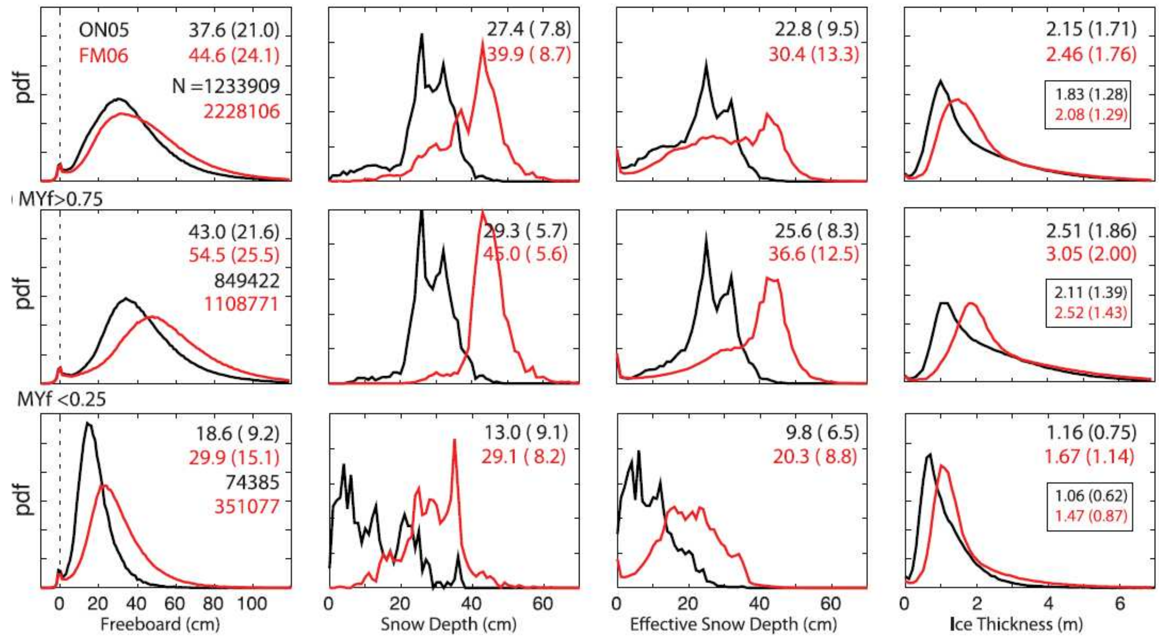

Figure 4.12: The distributions of the sea ice freeboard, constructed snow depth, effective snow depth (after adjusting the actual snow depth when larger than the total freeboard), and ice thickness for October-November 2005, February-March 2006 from *Kwok and Cunningham* (2008). a) first-row: Distribution in the entire Arctic Ocean. b) second-row: Distributions over multi-year ice regions. c) third-row: Distributions over first-year and second-year ice zones. N is the number of ICESat freeboard samples in the distributions. Mean and standard deviations for each ICESat mission phase are also provided.

the uncertainties in the SWE estimation, ECMWF fields, and sea ice advection from AMSR-E, deriving snow density values from the seasonal estimates from 1999 that are not representative of present day conditions, ignoring the effects of wind redistribution and snow sublimation, accuracy of the conversion from SWE/snow density to snow depth, etc. When the uncertainties are added together, it is likely that they are the same or more than the standard deviation of the snow depth estimates.

4.4.7 Sea ice freeboard to thickness conversion

The ratio of the freeboard to thickness depends on the physical properties (density) of the ocean, sea ice and the overlying snow layer. Under hydrostatic equilibrium, the relationship between sea ice thickness h_i, snow depth h_s, and the total freeboard h_{tf} is given by

$$h_i = \frac{\rho_w}{\rho_w - \rho_i} h_{tf} - \frac{\rho_w - \rho_s}{\rho_w - \rho_i} h_s \tag{4.9}$$

where ρ_i is the density of sea ice, ρ_s is the density of snow, and ρ_w is the density of seawater.

Table 4.3: List of models used in the sea ice freeboard retrieval from GLAS elevations and, their range and uncertainties

Parameter	Model used	Range	Uncertainty
Geoid (N)	EIGEN-GL04c	-30 to +66 m	$\sim$ 15 cm
Ocean tides (T)	AOTIM-5	-30 to +30 cm	$\sim$ 10 cm
Mean dynamic topography (MDT)	UW	-30 to +30 cm	$\sim$ 15 cm
Inverse barometric effect (IBE)	NCEP/NCAR	-10 to +10 cm	$\sim$ 5 cm

4.5 Summary

The method of determining sea ice freeboard heights from ICESat GLAS sea ice altimetry products was described. The instantaneous sea surface height at each footprint will be modeled using a number of geodetic and oceanographic models. A summary of those models, and their range variability in the Arctic Ocean and uncertainty, is presented in Table 4.3.

Chapter 5

Ocean Tide Models in Freeboard Estimation

In the sea ice freeboard retrieval process, ocean tide elevations need to be estimated for each ICESat footprint in order to model the true instantaneous sea surface height. ICESat data products use the GOT00.2 model to correct for the ocean and loading tides (*Ray*, 1999). However, this model and other available global/regional tide models have poor accuracy in the Arctic Ocean mainly because (i) the governing hydrodynamic equations in these models are not parameterized for the presence of sea ice (*King and Padman*, 2005), (ii) observations from ice-covered oceans were not assimilated into these models, and (iii) lack of high resolution, highly accurate bathymetry data especially under ice shelves (needed to model the tidal energy dissipation). Using such an erroneous model in the sea ice freeboard estimation, may sometimes seem like the ice is growing during the melting season or vice versa. In other words, it will introduce errors in the freeboard estimates. Tide models assimilate two types of observations: (i) satellite altimetry, and (ii) tide gauge records.

5.1 Motivation and objective

The ocean tides change in the Arctic Ocean when compared to tropical and subtropical open ocean, due to the presence of sea ice cover. For example, the tidal amplitude changes by up to 3% and the phase changes by about 1 hour (*Kowalik and Proshutinsky*, 1994). Although this change is small in the open ocean, locally it can occur at a wider range. Since the GOT model and other global and regional tide models are not constrained to include this ice-tide interaction, they have poor accuracy in the Arctic Ocean. Moreover, the *in-situ* data and altimetry data from the Arctic region that are needed for assimilation into these models are very limited. There are only a few long-term tide gauge stations that sparsely cover the polar coastal regions. Although there are more than 60 tide gauge stations along the Russian territory, these records are not publicly available. The latitudinal cutoff of Topex/Poseidon (T/P) altimetry data (up to 66° N/S) also limits the observations from ice-covered oceans. In addition, data from the winter months are not assimilated as they are not available as standard products (Fig. 5.1). The ERS missions, launched in 1992 and 1995, provided coverage up to 81.5° N/S. However, because of the sun-synchronous orbit of the ERS satellites, the aliasing of errors of the solar tidal constituents into the zero frequency limits their contribution to ocean tide modeling (*Andersen and Knudsen*, 1997). Hence, very limited observations from ice-covered oceans are available for the Arctic region that can be used to constrain the model and to include the presence of sea ice. As a result, these models can either overestimate or underestimate tides and perform poorly in the Arctic Ocean. Therefore, an accuracy assessment of the global and regional tide models needs to be carried out. The accuracy assessment is needed for identifying the best Arctic tide model, and also in the sensitivity analysis of the freeboard estimation. So far, the accuracy assessments of the ocean tide models were carried out generally for the global ocean (*Shum et al.*, 1997) or specifically for some regional studies (*e.g.*, *King and Padman* (2005)). A study focusing specifically on the Arctic Ocean is, thus, needed.

The objectives of this tide model assessment were the following:

1. To identify the best available tide model for the Arctic Ocean to be used in the

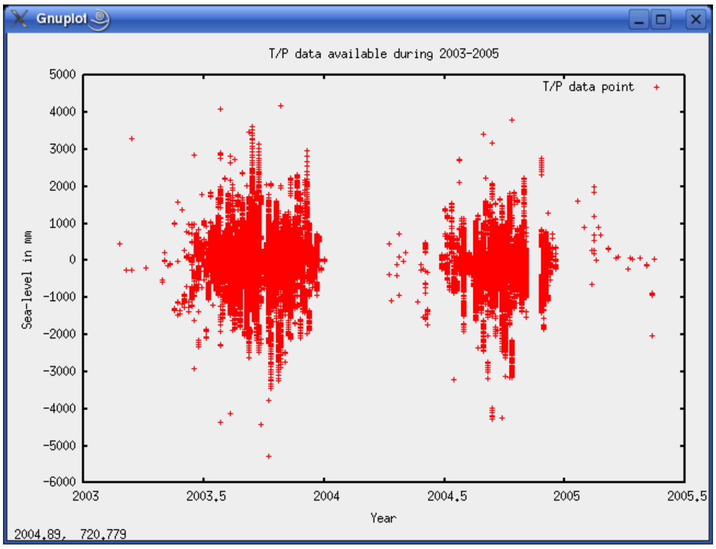

Figure 5.1: T/P data available between 2003–2005 near Churchill. A gap in the available data during the winter months is evident.

freeboard retrieval algorithm.

2. To study the influence of sea ice on the amplitude of ocean tides.

3. To study the effect of sea ice on the amplitude of major tidal constituents.

4. To evaluate the accuracy of the global and regional models in the Arctic Ocean.

The tide model assessment was carried out in different stages in this research: (i) assessment in Churchill, Manitoba, Hudson Bay by comparison with tide gauge data; (ii) assessment in the Arctic Ocean by comparison with tide gauge data; and (iii) assessment in Churchill, Manitoba, Hudson Bay by comparison with satellite altimetry data. In the following sections, an overview of (i) the existing ocean tide models, (ii) tide gauge and sea ice concentration data used in this study, (iii) ice-tide interaction processes, and (iv) accuracy assessment procedure and results is presented.

5.2 Ocean tide models

During 1994, about 12 new global ocean tide models were released after the availability of high precision T/P data whose aim was to improve tide models among other objectives. The ocean tide models that were evaluated in this study are mostly an updated version of these original models namely, CSR4.0, GOT00.2, TPXO6.2 and AOTIM-5.

5.2.1 CSR 4.0

The Center for Space Research global ocean tide model (CSR 4.0) was developed by Richard Eanes at the University of Texas. It is an updated version of the CSR 3.0 (*Eanes and Bettadpur*, 1996) and CSR 2.0 (*Eanes*, 1994) models. CSR 4.0 is an empirical model based on assimilation of 6.4 years of sea-surface height data from the TOPEX/Poseidon (T/P) altimetry mission with CSR 3.0 as reference model. CSR 3.0 is based on long-wavelength adjustment to the AG95.1 model (*Andersen et al.*, 1995) for the semi-diurnal tides and the FES94.1 model (*LeProvost et al.*, 1998) for the diurnal tides. The FES94.1 model is a purely hydrodynamic finite element model based on non-linear formulation of the shallow water equations and does not include any satellite altimetry data in its solution.

The corrections to the CSR 3.0 orthoweights (in $2^\circ \times 3^\circ$ spatial bins) were computed using the T/P altimetry data. These corrections were smoothed by convolving them with a two-dimensional Gaussian filter which has a full-width-half-maximum of 2.3 degrees. "The smoothed orthoweight corrections were output on the $0.5^\circ \times 0.5^\circ$ grid of CSR 3.0 and then added to the CSR 3.0 values to obtain the new CSR 4.0 model" (*Eanes*, 2002). CSR 4.0 follows the FES94.1 model beyond ± 66 latitude (as this is the cutoff for T/P data). It does not include any corrections to the long-period tides, even though the tides in long-period band were adjusted simultaneously with the tides in diurnal and semi-diurnal bands. Using the tidal orthoweights, ocean tides and loading tides can be synthesized for a given latitude, longitude and time. Necessary Fortran subroutines are available at (*Eanes*, 2002). The model can also be used for deriving tidal harmonic constants at a particular location.

5.2.2 GOT 00.2

The Goddard/Grenoble Ocean Tide Model (GOT00.2) , an updated version of GOT99.2 model (*Ray*, 1999), was developed by Richard Ray at NASA's Goddard Space Flight Center. This model is based on the assimilation of more than six years of T/P data, 81 cycles of ERS-1 and ERS-2 data, and a long wavelength adjustment of hydrodynamic models in shallow and inland seas and the FES94.1 model. It has a resolution of $0.5° \times 0.5°$. Since both T/P and ERS data were used in the assimilation process, this model is expected to perform better than CSR 4.0 in polar regions (66° N – 81.5° N) because the ERS tracks converge towards the poles and, therefore, provide dense measurements. Data from ice-covered regions were not assimilated into the model, therefore GOT00.2 will follow FES94.1 in those areas. *Ray* (1999) reports that the GOT99.2 model has an accuracy of < 1.5 cm in the deep ocean for the main semi-diurnal lunar constituent (M_2) when compared with deep-ocean tide-gauge measurements. More details about the model development and comparisons of the model with tide gauge records can be found in *Ray* (1999). The ICESat elevation product GLA13, used in this study, is already corrected for ocean tides and loading tides using this GOT00.2 model.

5.2.3 TPXO 6.2

The TOPEX/Poseidon crossover solution version 6.2 (TPXO6.2) is a medium-resolution (smaller than CSR 4.0 and GOT00.2), $0.25\,^{\circ}\times0.25\,^{\circ}$ fully global assimilation model developed by *Egbert and Erofeeva* (2002) at Oregon State University. It is a global model which best-fits, in a least-squares sense, the Laplace Tidal Equations and along track averaged data from T/P and Jason satellites. The methods used to compute the model are described in detail in *Egbert et al.* (2004) and *Egbert and Erofeeva* (2002). The model domain includes ocean cavities under the floating ice shelves. The principal assimilated data set in this model is T/P altimetry between 66° N/S latitude. However, ERS data and coastal and benthic tide gauge data from the Arctic and Antarctic were also assimilated into the model. Thus, TPXO6.2 is one of the most accurate global tidal solutions, particularly for high latitudes (*King and Padman* (2005), *King et al.* (2005) and *Padman and Fricker* (2005)).

TPXO 6.2 model is based on the generalized inverse (GI) modeling of the barotropic ocean tides approach. *Egbert and Erofeeva* (2002) state that this method has a number of significant advantages over other tidal data assimilation methods as it allows for the computation of a-posteriori error bars, testing of the hypotheses, and complete control over conditioning of the inverse solution, but has a main disadvantage of demanding heavy computations. *Egbert and Erofeeva* (2002) developed and implemented an efficient and feasible method for GI-based global and regional barotropic tidal modeling.

The latest version of the TPXO model (TPXO 7.1) is also currently available from *Egbert* (2009). Improvements in this model are due to the assimilation of longer time series of altimetry data, improved bathymetry, and improved resolution of global and local grids. This model was not available at the time of this research work.

5.2.4 AOTIM-5

The Arctic Ocean Tide Inverse Model (AOTIM-5) was developed by *Padman and Erofeeva* (2004) at the Oregon State University. It is a regional high-resolution (5-km regular grid) inverse model of Arctic Ocean barotropic tides. The authors also developed a Arctic Ocean linear-dynamics based tide model (AODTM). The AOTIM-5 model assimilated a number of coastal and benthic tide gauges (about 250 to 310 tide gauges per constituent) and T/P and ERS altimetry data (about 364 cycles and 108 cycles, respectively) for further improvements of the dominant constituents. It uses the open boundary forcing from the TPXO.6.2 solution, and a newer bathymetry from the International Bathymetric Chart of the Arctic Ocean (*Jakobsson et al.*, 2000). Data assimilation was done only for the four most energetic simulated tidal constituents (M_2, S_2, K_1 and O_1): TG+T/P+ERS for M_2 and O_1, TG+T/P for K_1 and TG only for S_2.

This model is significantly better than other global models mainly in the Canadian Arctic Archipelago, Nares Strait, and the Baffin Bay and Labrador Sea, and can be explained by the higher resolution of the new model in these topographically complex regions (*Padman and Erofeeva*, 2004). The authors suggest that the model can be significantly improved by further increasing model resolution, adding ice-ocean interactions, and increasing the sophistication of dissipation parameterizations, including benthic friction and the conversion of barotropic tidal energy to internal tides. They also suggest that the dynamics-only model (AODTM) should be developed with comparable accuracy as the AOTIM-5. AODTM will significantly perform better than AOTIM-5 in regions where no tide gauge records are available, *i.e.*, in the central deep Arctic basins, due to the accurate modeling of dynamics. In contrast, AOTIM-5 is simply an extrapolation of a solution that is constrained by coastal tide gauge data. AOTIM-5 is used in this research work and it is available for downloading through the Oregon State University website.

5.3 Tide Gauge Records in the Arctic Ocean

In most parts of the Arctic, there has been a rapid reduction in the number of operational Arctic tide gauges. *Plag* (2000) reported the current status of Arctic tide gauges and made recommendations to improve the spatial and temporal coverage of the Arctic observing system. For example, (i) organizing the Arctic tide gauges into a more homogeneous regional network, (ii) co-locating tide gauges with space-geodetic receivers, (iii) performing zero-epoch absolute gravity measurements at these tide gauge stations.

Table 5.1: List of Arctic tide gauge stations analyzed in this study and their record length

Station Name	Latitude	Longitude	Record Length
Prudhoe	70.40000	211.47333	Jul 1, 1993 - Oct 31, 2004
Churchill	58.76667	265.81667	Jan 1, 1940 - Dec 31, 2005
Alert	82.49186	297.68267	Nov 1, 1961 - Jul 31, 1979
Tuktoyaktuk	69.43826	227.00560	Nov 1, 1961 - Sep 30, 1991
Resolute	74.68333	265.11667	Nov 1, 1961 - May 31, 1977
Cambridge Bay	69.11667	254.93333	Nov 1, 1961 - Aug 31, 1981
Cape Parry	70.15000	235.33333	Aug 1, 1966 - Jul 31, 1981
Sachs Harbour	71.96667	234.75000	Sep 1, 1971 - Jul 31, 1982
Cornwallis	75.38333	236.05000	Nov 1, 1986 Sep 30, 1994

In this study, the Tide Gauge Records (TGR) for 9 stations (Fig. 5.2) were obtained from Marine Environmental Data Services (MEDS) and Joint Archive for Sea Level (JASL). The station name, location and record length are listed in Table 5.1. MEDS, Canada, maintains an inventory of tide and water level (TWL) for about 966 stations all over Canada, however, most of them are located outside the Arctic basin and thus do not contribute to the knowledge of ocean tides in the Arctic ocean (open ocean). Hourly, daily and monthly TWL data are available from the Canadian Hydrographic Service's water level gauging network. JASL, a collaboration between the University of Hawaii Sea Level Center, the World Data Center-A for Oceanography, the National Oceanographic Data Center, and the National Coastal Data Development Center, provides a research quality database for about 330 stations. It is the largest global collection of quality-controlled hourly sea level data. JASL provides hourly, daily mean and monthly mean TWL.

5.4 Sea ice concentrations

Sea ice concentrations (SIC) were obtained from the SSM/I passive microwave sensor (*Comiso*, 1990) and weekly ice charts provided by the Canadian Ice Services.

5.4.1 SSM/I

The National Snow and Ice Data Center (NSIDC), Boulder, Colorado provides SSM/I daily and monthly polar gridded SIC. SSM/I sea ice products are in polar stereographic projection, gridded at a resolution of 25 km × 25 km, beginning 25 June 1987. Two sets of SSM/I SIC grids have been formulated. The first data set was generated using the NASA Team algorithm (*Cavalieri et al.*, 1996) and the second

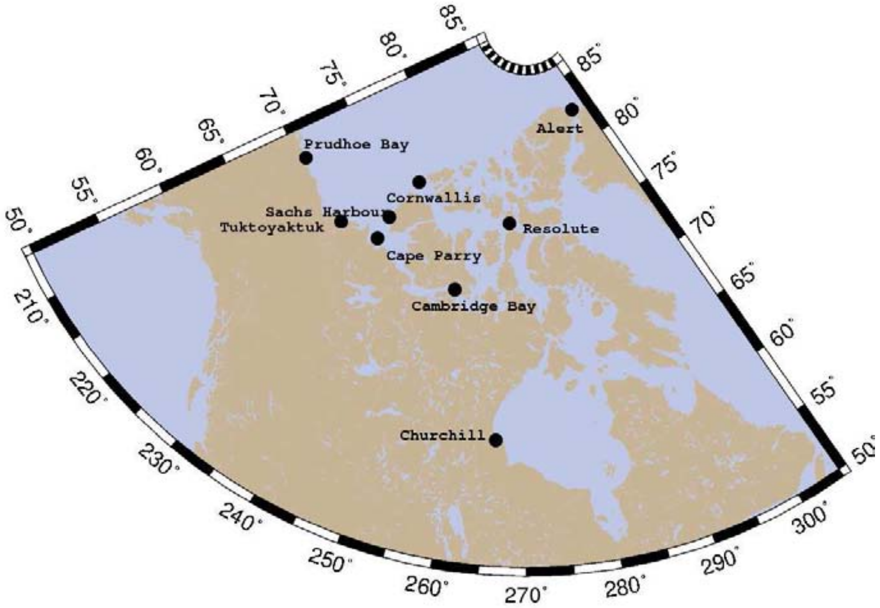

Figure 5.2: Arctic tide gauge stations

using the Bootstrap algorithm (*Comiso* (1990), which was used in this study). The SSM/I-derived ice concentrations are daily total and monthly averaged ice fractions for both hemispheres. Both the NASA Team and Bootstrap data are provided in Hierarchical Data Format.

5.4.2 Ice Charts

SIC were provided by Canatec Associates, Calgary, Canada, using their Ice Statistics Program (ICE '06). ICE'06 was recently upgraded in November 2006 with a new worldwide ice data set (years 1972–2005). ICE '06 generates statistical output based on over 30 years of continuous weekly ice charts. The source data are in the SIGRID gridded ice format standard of the World Meteorological Organization (WMO). The nominal resolution of SIGRID is 25 km in latitude (and the longitudinal resolution varies with latitude).

As the interaction of sea ice and tidal constituents must be discussed at the same time and location, it is noted that the SIC data are available only from 1972 (Ice Charts) and 1987 (SSM/I). However, the TGR at most of the stations (*e.g.*, Alert, Resolute) are available from 1961 and at some stations they end in the late 1970's. Hence, the SIC data were not available for comparison at all stations/times.

5.5 Ice-tide interactions

5.5.1 Effect of tides on sea ice

The ice-tide interactions affect the air-sea-ice interaction, and hence play an important role in the climate regime in ice-covered areas. They influence the heat exchange from the ocean to the atmosphere through formation of tidal leads (see, *Holloway and Proshutinsky* (2007)). Tidal currents induce stress at the ice-water interface and increase tidal mixing at the bottom of the ice layer. This causes more heat to be transported from the deep ocean into the surface mixed layer that can result in formation of polynyas (*Martin et al.*, 2004). The magnitude of the stress that is induced depends on the relative velocity between the sea ice layer and the ocean (*Pease et al.*, 1983). During winter, when the ice formation is complete and packed, the sea ice mobility is confined and the relative velocity between the ice layer and the tidal current increases, which exerts more stress at the ice-ocean interface. This can lead to increased turbulent heat fluxes and reduce the thermodynamic ice growth.

Koentopp et al. (2005) ran a dynamic-thermodynamic sea ice model with and without adding the tidal stress. Their results showed that the tidal currents reduce the expansion of sea ice cover (15 to 25% in marginal ice zones), speed up the retreat process and alter the evolution of sea ice both locally by 5% (and at basin-wide scales, although, to a lesser extent).

Tides also cause lateral shear and strain on the ice cover. This can cause the ice layer to fracture and lead to more open water formation. *Eisen and Kottmeier* (2000) show that tides enhance the lead formation in the western part of the Weddell Sea which increases the heat exchange between the ocean and the atmosphere, affect the salt mass released into the ocean and the thermodynamic ice growth rate. *Heil et al.* (2008) found that the sea ice velocity variance near the continental shelf in the Weddell Sea was dominated more by semi-diurnal processes such as tides rather than low-frequency atmospheric changes.

5.5.2 Effect of sea ice on ocean tides

The effect of ocean tides on sea ice has been studied extensively in the past, while the influence of sea-ice cover on the ocean tides is yet to be explored in detail. Although the tidal variations have been studied, the seasonal variations due to the presence of sea ice cover have not been analyzed (*Kagan et al.*, 2008). The precise role of the ice-ocean stress in the observed tidal variations is thus unclear.

Sea ice cover dampens the tidal amplitude and affects the phase of the tidal wave. Fig. 5.3 shows a negative correlation between the tide water level from TGR and sea ice concentration that was observed at the Churchill tide gauge station in Hudson Bay. A minimum water level is measured during winter months when there is a maximum SIC, and a maximum water level is measured during the summer months when ice-free conditions prevail. The decreased water level is due to the damping mechanism to dissipate the tidal energy that also induces friction at the ice-ocean interface. Such decrease in tidal elevations were also observed by *Murty* (1985). *Godin and Barber* (1980) summarized the variability of tides in the Canadian Arctic tide stations. They found that the variability of tides induced by the ice cover were more detectable in Hudson Bay and the Amundsen Gulf, whereas around Resolute the effect was not detectable. They also noted that the arrival time of the tides at the sites was altered both ways during the ice-free months, *i.e.*, arrived early and delayed. *St-Laurent et al.* (2008) also measured this influence of sea ice on the tidal amplitude and phase in the Hudson Bay System (Fig. 5.4) using a numerical model and observations from moorings. They noted that the tidal range both increased (Hudson Strait) and decreased (Hudson Bay, Foxe Basin) in different areas of the Hudson Bay System. Through numerical simulations, they demonstrated that the seasonal variability of the M_2 amplitude in some stations was caused by the under-ice friction.

5.6 Accuracy assessment of Ocean tide models using tide gauge records

5.6.1 Accuracy assessment in Churchill, Hudson Bay

The accuracy assessment of the ocean tide models were carried out first in Churchill because Hudson Bay exhibits a seasonal ice cover. Therefore, it is ideal for evaluating the performance of tide models in the presence and absence of ice cover.

The Hudson Bay System

Hudson Bay is the largest inland sea in Canada, extending from 51° N to 70° N and 78° W to 95° W. The total area of the enclosed sea is about 800,000 km^2. Together

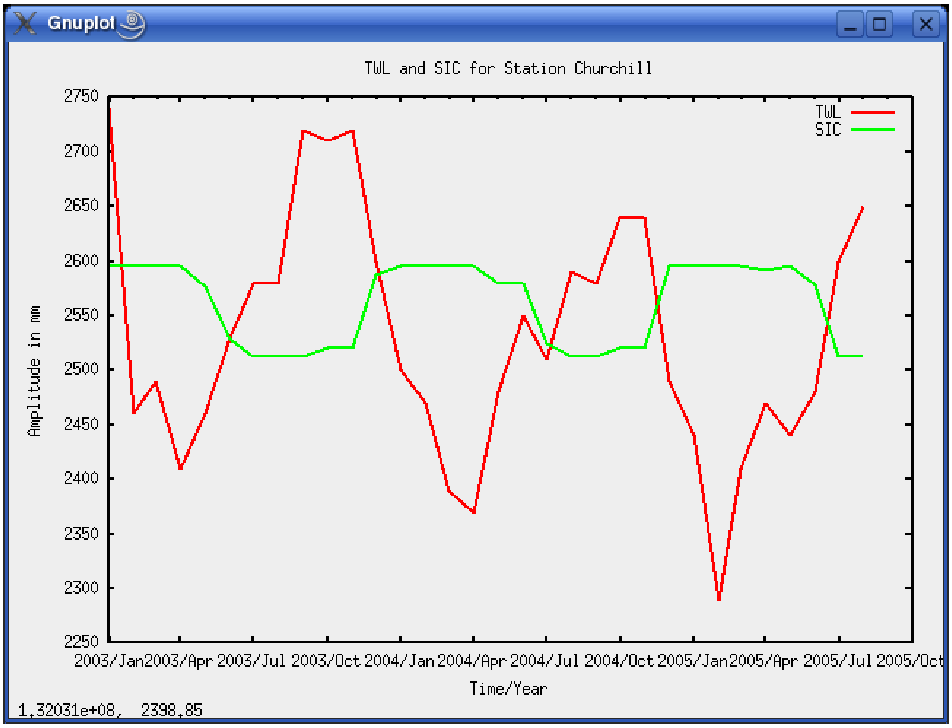

Figure 5.3: A time-series of tide water level (red curve) and sea ice concentration (green curve) indicates they are negatively correlated.

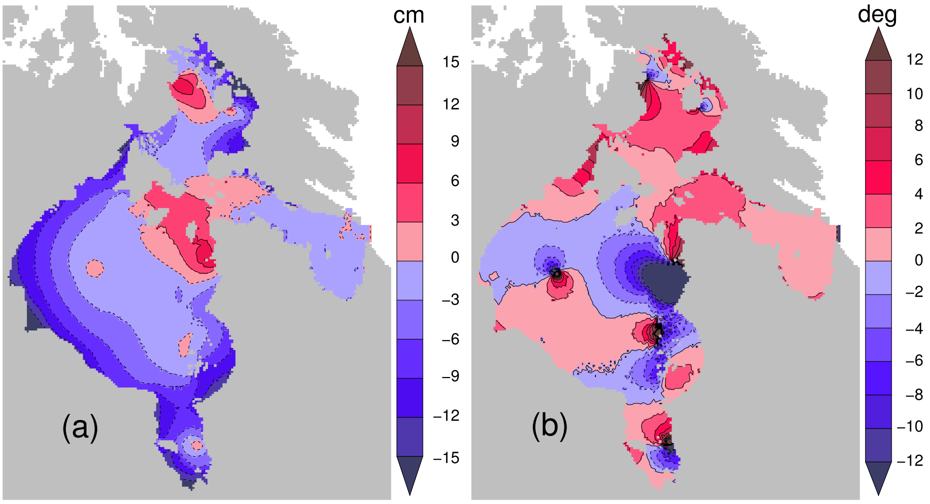

Figure 5.4: The amplitude and phase anomaly in the M_2 constituent between (a) March and (b) September, derived by *St-Laurent et al.* (2008) using numerical simulations.

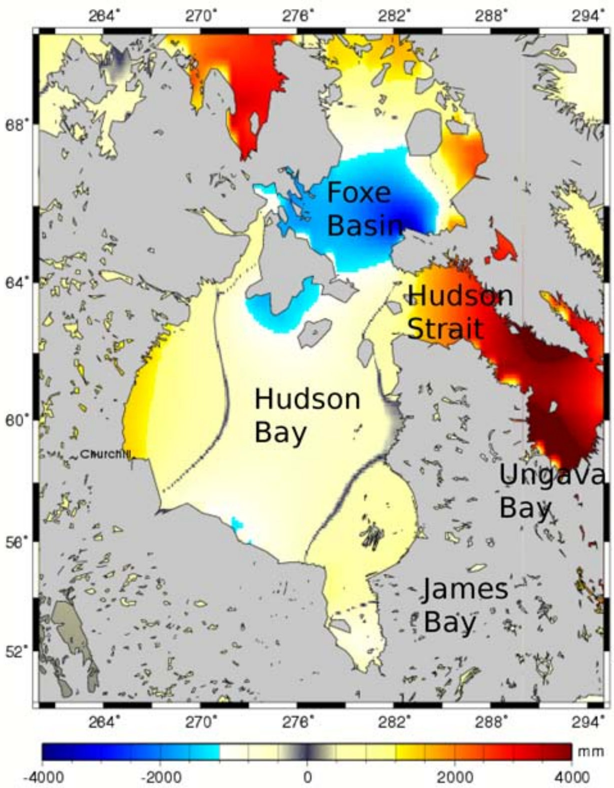

Figure 5.5: Ocean tides in the Hudson Bay System predicted using the CSR 4.0 model (January 1, 2006).

with James Bay, Foxe Basin, Hudson Strait, Ungava Bay and other adjacent basins, the area of the Hudson Bay System is about 1,200,000 km^2 (Fig. 5.5). It is a shallow basin with maximum water depth of about 258 m (or 867 m including other basins). Hudson Bay is essentially a closed system (exchange of waters only through Foxe Basin and Hudson Strait) that is isolated from the open-ocean circulation. Hence, the change in sea level (or sea ice surface height) is mainly due to atmospheric pressure loading and ocean tides. The tidal range is about ∼4 m (Fig. 5.5). Tides enter through the Hudson strait and travel along the south-west coast in the Hudson Bay.

Annual sea ice concentration

Hudson Bay is usually 100% ice-covered during the winter months from January to March and completely ice-free during the summer months from August to September. During the melt onset in April, the sea ice concentration (SIC) along most of Hudson Bay is $\sim$ 70–90%, whereas in the northwest it is only about 40–60% due to the strong northwesterly winds in that region that drive the sea ice offshore (*Mysak et al.*, 1996). In July, most of Hudson Bay is ice-free except along the southern shore where the SIC is $\sim$ 20–40%. This is due to piling up of sea-ice pushed southward from the North. In this study, SIC data were obtained from SSM/I passive microwave sensor measurements distributed by NSIDC (section 5.4).

Churchill Tide Gauge Station

Churchill is the only major, currently operational tide gauge station in Hudson Bay with more than 65 years of data. Other tide gauges such as Inukjuak, Coral Harbour and Moosonee operated only for few months during 1972–1980. The time series of monthly tide water level in Churchill (Fig. 5.6) shows a decrease in sea level of $\sim$ 1 m in 60 years, *i.e.*, $\sim$ 15 mm/year. This is an evidence of post-glacial rebound occurring around Churchill. Until 1940, the TGRs were available only for the summer months and they were not representative of the tides occurring during other seasons. The tide gauge station was initially located close to the mouth of the Churchill River (*Wolf et al.*, 2006), therefore, it was influenced more by the river inflow rather than the dynamics in the open ocean. In addition, the TGR contains errors in the calibration of the tide gauge during the early 1940's. *Tushingham* (1992) speculated other complications in the Churchill TGR due to the Churchill River Diversion Project in 1975–1977 that resulted in a drastic reduction of the outflow. Although, there were

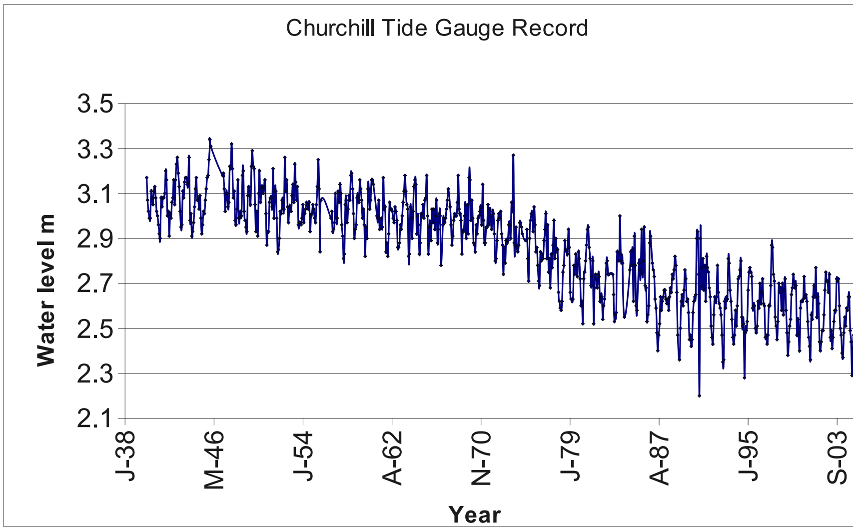

Figure 5.6: Churchill tide gauge record between 1938–2003 indicating a decrease in sea level of approximately ∼15 mm/year.

problems with the Churchill TGR during the early years, it is the only long-term TGR available for the Hudson Bay System. In this study, the hourly TGRs from January 2003 to September 2005 were analyzed.

Analysis of Tide Gauge Records

TGRs were analyzed using the software package developed by *Foreman* (1977). Tidal constituents can be derived from the input tide water levels, which can be unevenly spaced in time. Hence, old tide gauge records consisting of only the daily extreme values can be analyzed as well. Using the derived tidal constituents as an input, tide water levels can be predicted. When the predictions were made for the same time period as the input tidal constituents, the predicted tide water levels are referred to as *synthetic* data. Real observations and synthetic data are not identical, as the synthetic tides only consider the major constituents, although the number of constituents can be freely selected. However, predictions can also be made for future months and years using the derived tidal constituents.

Analysis of major tidal constituents

In section 5.5.2, it was shown that the tide water level is negatively correlated with the sea ice concentration. Although, both ocean tides and sea ice cover exhibit a seasonal/annual cycle, this negative correlation between them is *not* a coincidence. In order to demonstrate that this correlation is due to the ice-tide interaction, and not entirely due to the annual period of the astronomical tide-generating forces, tidal constituents (especially semi-diurnal and diurnal) were analyzed separately in this study.

Hourly TWL were predicted using the global and regional tide models CSR 4.0, GOT00.2, and TPXO6.2 described in section 5.2. Using Foreman's software, the tidal constituents were derived from the (i) TGRs, (ii) Synthetic data, and (iii) three global tide models. In this study, a time series of four tidal constituents were derived: M_2 (semi-diurnal lunar), S_2 (semi-diurnal lunar), K_1(diurnal lunisolar), O_1 (diurnal lunar), similar to *Andersen et al.* (1995). A three-month window of TWL data was used to derive the tidal constituents representative for the central month. Then, the window was moved forward by one month to calculate the next set of tidal constituents that again refers to the central month, *i.e.*, the following month when compared to the previous three-month window. Thus, a monthly time-series of tidal constituents were derived. The time-series was then compared with the sea ice concentration values in order to assess the effect of sea ice on the tidal constituents amplitude.

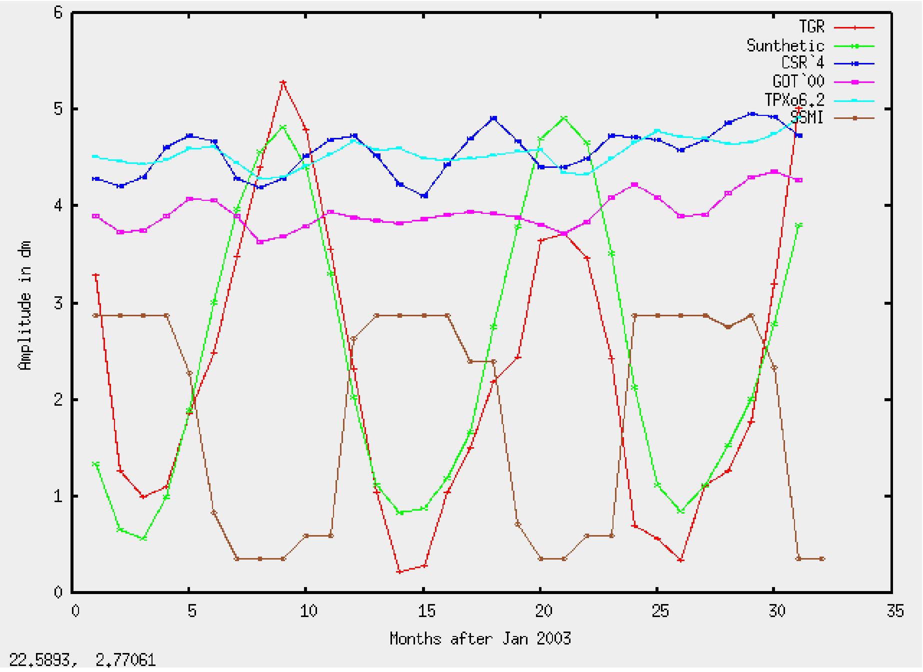

Figure 5.7: A time-series of M_2 tidal amplitude in Churchill were derived using i) tide gauge records (red curve), ii) synthetic data (green), and iii) CSR 4.0 (blue), iv) GOT ‘00 (purple), v) TPXO6.2 (cyan) ocean tide models and compared with SSM/I sea ice concentrations that were scaled down from 0–100% to match the scale of the tidal amplitude (brown). A negative correlation is observed between the sea ice concentration and the M_2 tidal amplitude derived from TGR and synthetic data.

The comparison of the M_2 tidal amplitude from TGR and models with the SIC is shown in Fig. 5.7. SIC is scaled down from 0–100% to match the scale of amplitude values. During winter, when the SIC is high, the TGR M_2 amplitude is minimum indicating the damping mechanism. The synthetic data also exhibit similar behavior because they were derived using the constituents from TGR data. The global tide models CSR 4.0, GOT 00 and TPXO6.2 agree with each other, mainly because they have assimilated similar altimetry data sets during the model development, and are based on similar hydrodynamic principles - all excluding the ice-tide interaction processes. Therefore, they do not exhibit seasonal behavior or agree with the *in-situ* TGR that records the real tidal amplitude under the influence of sea ice cover. The difference between model prediction and TGR in Churchill is approximately 35 cm for the M_2 component alone. This is an indicator that these models are not constrained to include the ice-ocean frictional processes.

The results from TGR analysis indicate the effect of sea ice on tides. These results can be verified with the findings from *St-Laurent et al.* (2008) who were the first to show the significant seasonal variability of M_2 occurring throughout the Hudson Bay System (HBS). The authors analyzed data from eight moorings distributed throughout the HBS. They found that the M_2 amplitude both increased (near Hudson Strait) and decreased (Hudson Bay and Foxe Basin) at different stations in HBS. Using numerical experiments, they were also able to demonstrate that these seasonal variations (modification of winter M_2 elevation) were caused by the under-ice stress that modifies the amphidromic points and accounts for both the increased and decreased winter elevations.

In summary, the time-series analysis of the M_2 amplitude from TGRs shows the damping mechanism near Churchill. The global models do not agree with TGRs and are not able to include this effect in their tidal predictions as the ice-tide frictional processes are not parameterized in the models. A similar analysis was carried out for the most energetic tidal constituents, M_2, S_2, K_1, O_1, with the TGR in the Canadian Arctic where a similar damping effect on the tidal constituent amplitude was detected. This indicates that the negative correlation between the SIC and tidal constituent amplitude is not caused by annual climate variations, but is due to the sea ice-tide interaction processes. The findings from this analysis are presented in the following section.

5.6.2 Accuracy assessment in the Arctic Ocean

Tide gauge records from a number of stations were analyzed in this study in order to determine the accuracy of the global and regional ocean tide models in different parts of the Arctic Ocean. Predictions of tide water levels at nine tide gauge stations (Table 5.1, Fig. 5.2) were made using the tide models CSR 4.0, GOT00.2, TPXO6.2, and AOTIM-5. Time-series of tidal constituents were derived from TGR and tide model predictions, following the same procedure as described in section 5.6.1. These constituents were compared with each other and with the SIC from SSM/I and ice charts whenever available. The findings are summarized as follows:

1. All tidal constituents derived from TGR were negatively correlated with the sea ice concentration. The M_2 constituent exhibits the most variability (damping) due to sea ice cover, *e.g.*, in Churchill (Fig. 5.17), Cambridge Bay (Fig. 5.12) and Cape Parry (Fig. 5.15). This is in agreement with the results from *Godin*

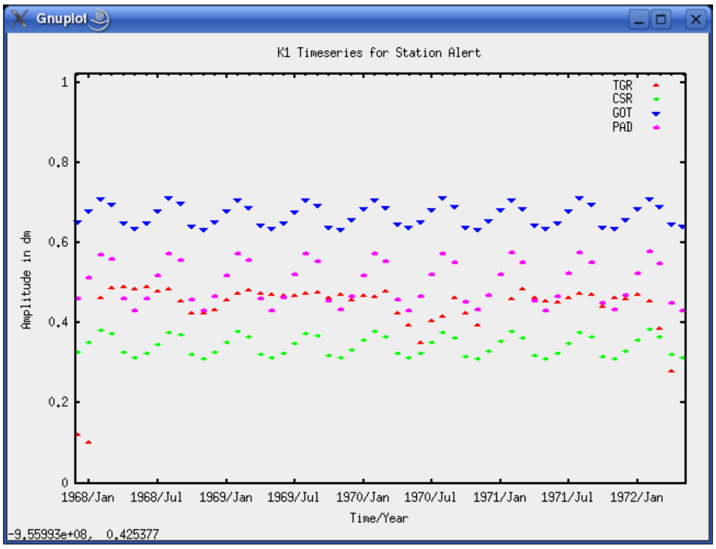

Figure 5.8: A time-series of K_1 tidal amplitude at Station Alert derived from i) tide gauge records (red curve), ii) CSR 4.0 (green), iii) GOT '00 (blue), iv) AOTIM-5 (purple) ocean tide models. AOTIM-5 model shows good agreement with the TGR.

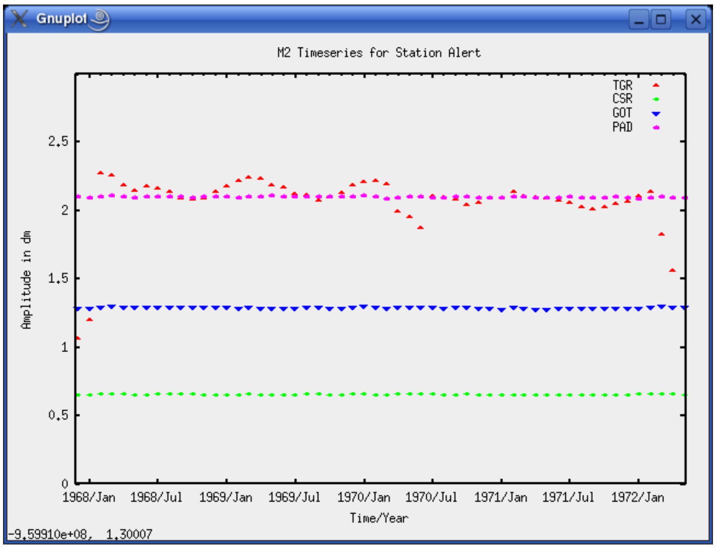

Figure 5.9: A time-series of M_2 tidal amplitude at Station Alert derived from i) tide gauge records (red curve), ii) CSR 4.0 (green), iii) GOT '00 (blue), iv) AOTIM-5 (purple) ocean tide models. AOTIM-5 model shows good agreement with the TGR.

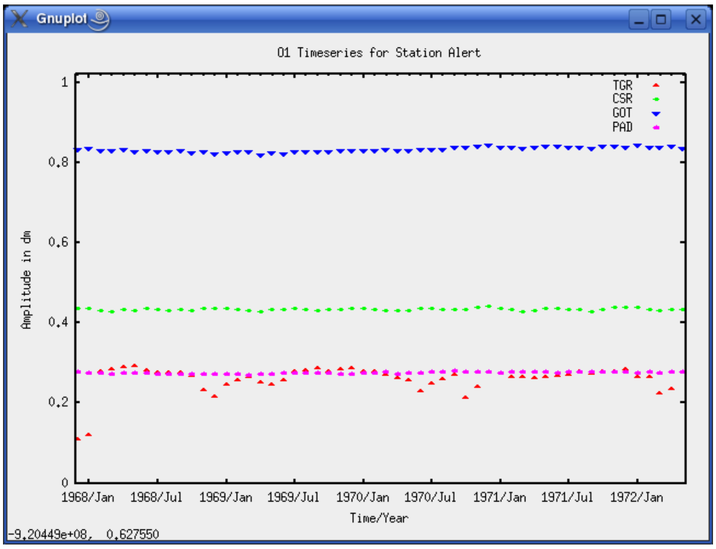

Figure 5.10: A time-series of O_1 tidal amplitude at Station Alert derived from i) tide gauge records (red curve), ii) CSR 4.0 (green), iii) GOT '00 (blue), iv) AOTIM-5 (purple) ocean tide models. AOTIM-5 model shows good agreement with the TGR.

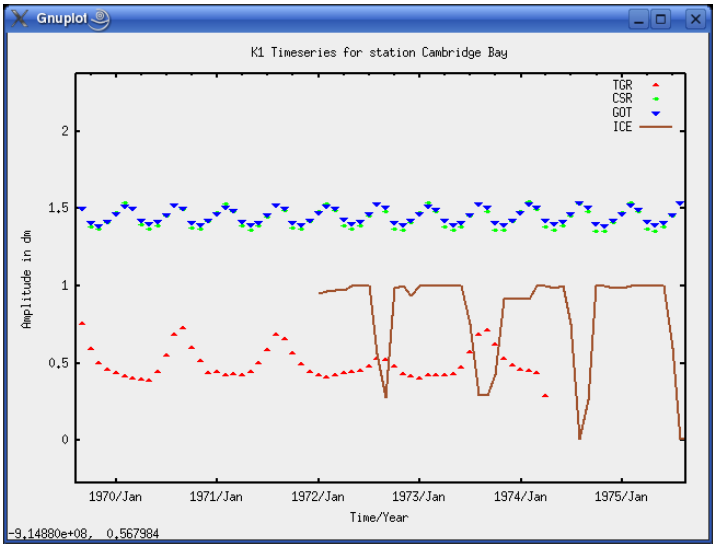

Figure 5.11: A time-series of K_1 tidal amplitude at Station Cambridge were derived from i) tide gauge records (red curve), ii) CSR 4.0 (green), iii) GOT '00 (blue) ocean tide models and compared with sea ice concentrations (brown). TGR and SIC show a negative correlation. The global models and TGR show poor agreement (in amplitude).

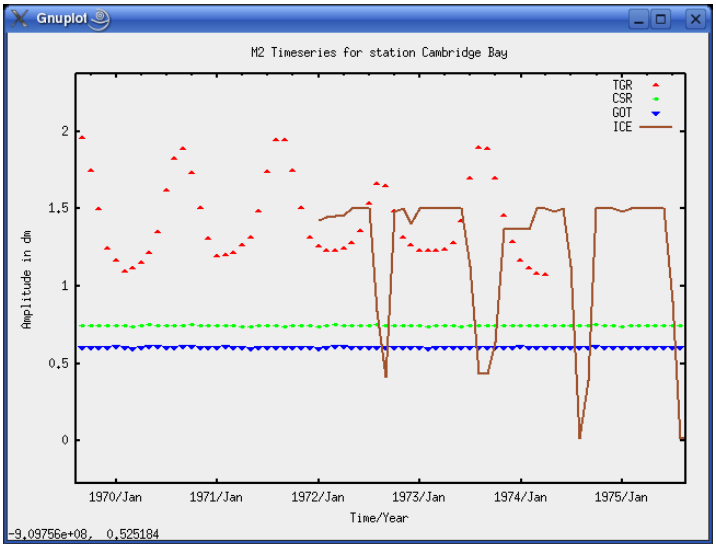

Figure 5.12: A time-series of M_2 tidal amplitude at Station Cambridge were derived from i) tide gauge records (red curve), ii) CSR 4.0 (green), iii) GOT '00 (blue) ocean tide models and compared with sea ice concentrations (brown). TGR and SIC show a negative correlation. The global models and TGR show poor agreement (in amplitude).

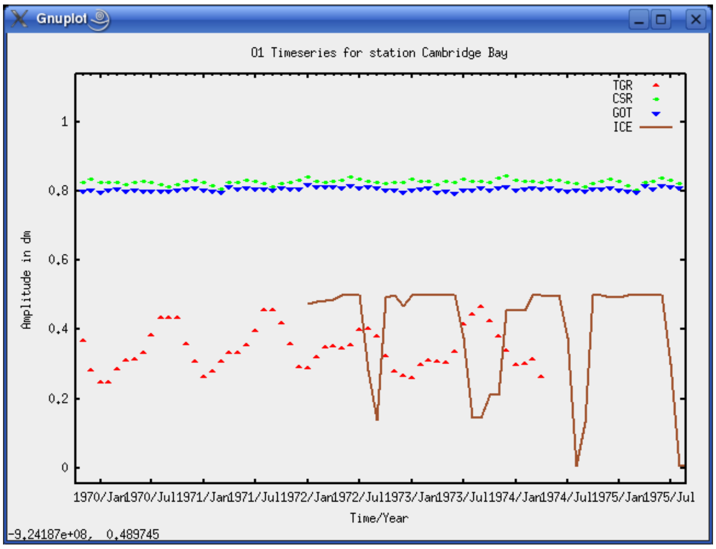

Figure 5.13: A time-series of O_1 tidal amplitude at Station Cambridge were derived from i) tide gauge records (red curve), ii) CSR 4.0 (green), iii) GOT '00 (blue) ocean tide models and compared with sea ice concentrations (brown). TGR and SIC show a negative correlation. The global models and TGR show poor agreement (in amplitude).

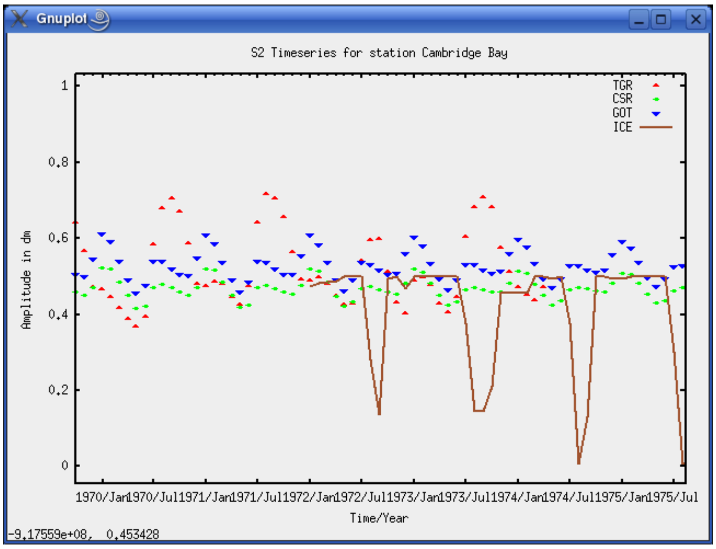

Figure 5.14: A time-series of S_2 tidal amplitude at Station Cambridge were derived from i) tide gauge records (red curve), ii) CSR 4.0 (green), iii) GOT ‘00 (blue) ocean tide models and compared with sea ice concentrations (brown).

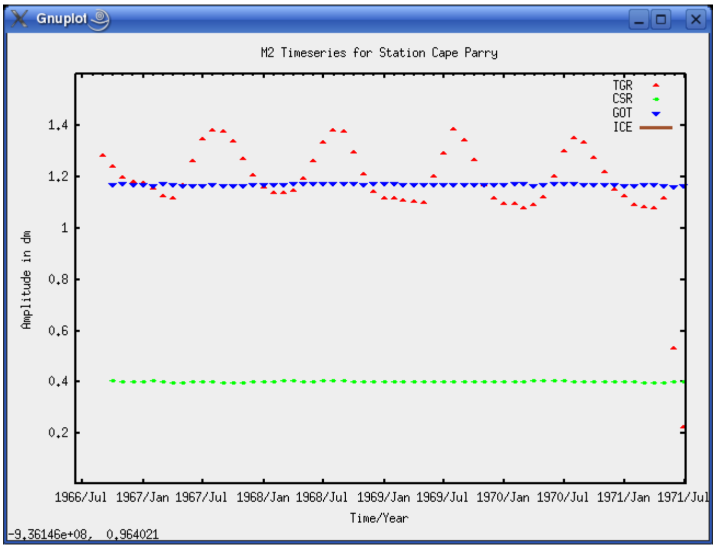

Figure 5.15: A time-series of M_2 tidal amplitude at Station Cape Parry were derived from i) tide gauge records (red curve), ii) CSR 4.0 (green), iii) GOT ‘00 (blue) ocean tide models and compared with sea ice concentrations (brown).

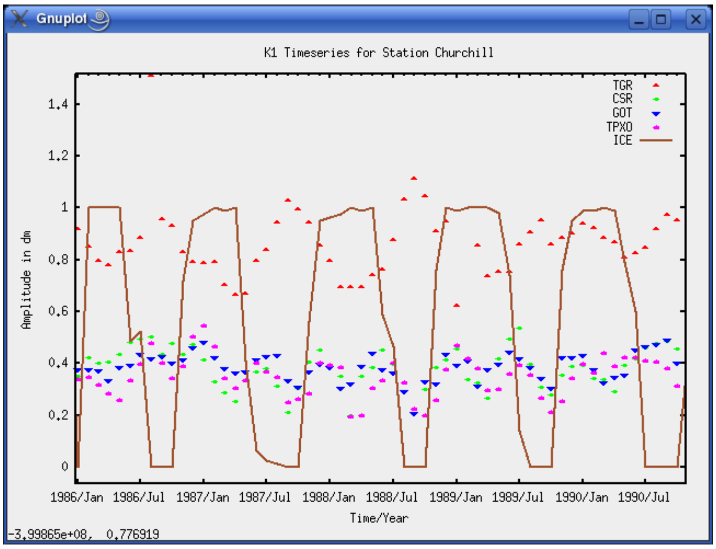

Figure 5.16: A time-series of K_1 tidal amplitude at Station Churchill were derived from i) tide gauge records (red curve), ii) CSR 4.0 (green), iii) GOT '00 (blue), iv) TPXO6.2 (purple) ocean tide models and compared with sea ice concentrations (brown).

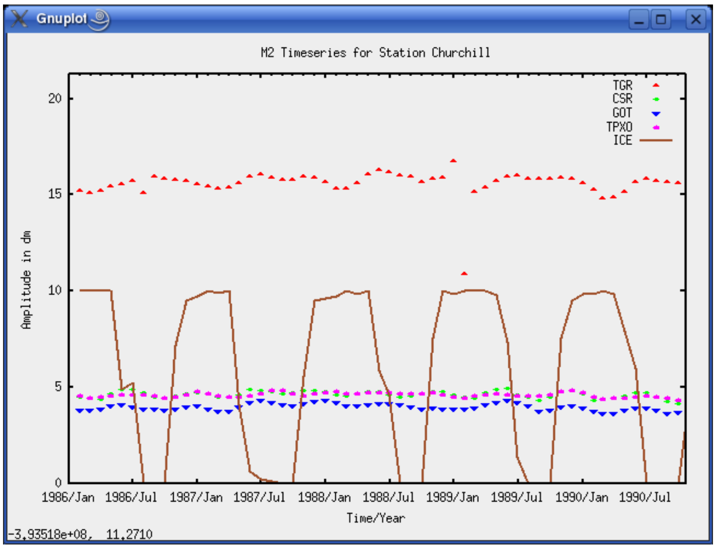

Figure 5.17: A time-series of M_2 tidal amplitude at Station Churchill were derived from i) tide gauge records (red curve), ii) CSR 4.0 (green), iii) GOT '00 (blue), iv) TPXO6.2 (purple) ocean tide models and compared with sea ice concentrations (brown).

and Barber (1980). Although they did not analyze the tidal constituents, they found an increase in the tidal range during open water conditions at stations Churchill, Cambridge Bay and Coral Harbour during 1971–1975. They also found that the variability in the tidal range was not detectable in the Resolute TGR.

2. The global ocean tide models are not correlated to the sea ice dynamics (Fig. 5.12, 5.13 and 5.11). For example, these models do not exhibit similar seasonal behavior as the TGR. An explanation is clearly that these models do not assimilate data from the sea ice covered areas and winter months, hence, the models are not sensitive to sea ice–tide interactions.

3. Amplitude of the tidal constituents are either overestimated (in Alert and Cambridge Bay; Fig. 5.13, 5.11, and 5.10) or underestimated (in Alert, Churchill and Cambridge Bay; Fig. 5.12, 5.17, 5.9 and 5.16) by the global models when compared to TGR. The differences are of the order of 1 to 10 cm.

4. The difference between TGR and global models, including the high-resolution TPXO6.2 model, is particularly large (10 cm) in Churchill (Fig. 5.17) where the tidal ranges are generally high (∼4 m) compared to the open ocean.

5. The AOTIM-5 regional tide model is found to perform the best of all models in areas where the AOTIM-5 is defined (Fig. 5.9, 5.8 and 5.10) in terms of tidal amplitude prediction, that is if the TGR is considered to be absolute. At most of the stations, the AOTIM-5 model prediction and the TGR agree well and match in amplitude (Fig. 5.9) while the global models overestimate or underestimate the constituent. The main reason for this excellent agreement is

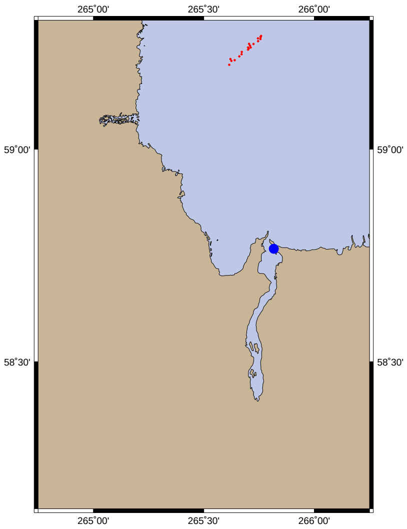

Figure 5.18: The amount of T/P available within a 50 km distance from the Churchill tide gauge station.

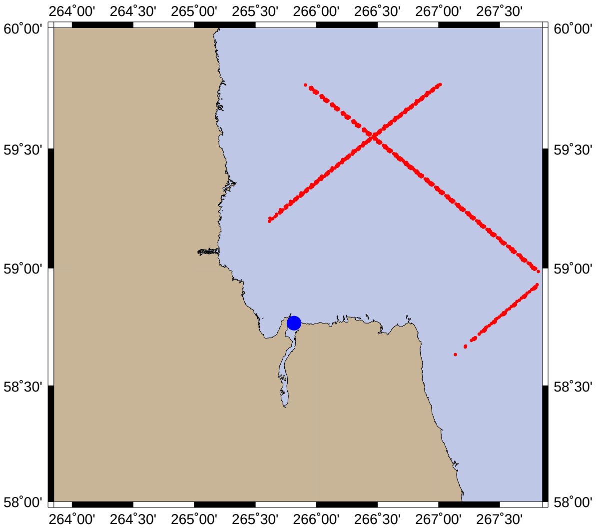

Figure 5.19: The amount of T/P available within a 100 km distance from the Churchill tide gauge station.

because these data were already assimilated into the model (see section 5.2). However, the AOTIM-5 does not show the annual variability as the TGR but only matches in the amplitude.

5.7 Accuracy assessment of Ocean tide models using Satellite Altimetry data

The assessment of global tide models by comparison with TGRs only indicates the accuracy of these models near the coast where tide gauge stations are situated. However, the performance of the global tide models in the open ocean must also be assessed in order to obtain a comprehensive analysis of their accuracy in the entire Arctic basin, including open ocean and coastal areas.

As a preliminary analysis, T/P altimetry data from January 2003 and September 2005 were compared with the global tide models and TGRs near Churchill. Fig. 5.18 and 5.19 shows the T/P data that were available for the time period of this study. The comparison was done using two data sets: (i) data available within a 50 km radius from the Churchill tide gauge station, and (ii) data available within a 100 km radius from the Churchill station. The differences T/P – models and T/P – TGR are summarized in Table 5.2 and 5.3. The results are discussed as follows:

Table 5.2: Mean and standard deviation of the differences between T/P and global ocean tide models near the Churchill tide gauge station within a 50 km radius.

Comparison	Mean (m)	Std.Dev.(m)
T/P – TGR	-0.02	0.34
T/P – CSR 4.0	-0.02	0.16
T/P – GOT 00.2	0.02	0.14
T/P – TPXO6.2	-0.05	0.32

Table 5.3: Mean and standard deviation of the differences between T/P and global ocean tide models near the Churchill tide gauge station within a 100 km radius.

Comparison	Mean (m)	Std.Dev.(m)
T/P – TGR	0.01	0.53
T/P – CSR 4.0	-0.01	0.31
T/P – GOT 00.2	0.03	0.40
T/P – TPXO6.2	0.02	0.43

The mean of the difference between the T/P data (within 50 km of Churchill station) and the global models (CSR and GOT) was ∼2 cm and the standard deviation was ∼15 cm. The differences between the T/P data (from 50 km radius) and TPXO6.2 data were larger, having a mean of ∼5 cm and a standard deviation of ∼35 cm. This might be due to the higher resolution of the TPXO6.2 model, 25 km × 25 km (*i.e.*, only 25 km from the Churchill station). Because the footprint size of T/P is ∼2–20 km, it will lead to differences in the location where the tidal values are compared. The mean of the difference between T/P data (within 100 km radius) and the global tide models was ∼2 cm and the standard deviation was ∼35 cm. Here again, the larger differences are due to discrepancies in the resolution of the two data sets and tides vary significantly within this distance.

The mean of the differences between T/P data (within a 50 km radius) and TGR was ∼2 cm and the standard deviation was ∼34 cm. The mean of the difference between T/P data (within 100 km radius) and TGR was ∼1 cm and the standard deviation was ∼53 cm. TGR and T/P data show large differences because the tide gauge station is on land while the closest altimetry data points are about 50 km offshore. Tides in this region change within this 50 km distance.

The T/P data near the coast are not accurate because they have large footprint sizes (∼2 – 20 km) and the return from these areas are not necessarily purely from the ocean or land. Similarly, the global tide models also perform poorly near the coast because only a limited amount of altimetry data were available for assimilation near the coast. Secondly, the high-resolution high-accuracy bathymetry data needed to model the tidal energy dissipation through baroclinic tides were limited. Hence, the differences between the T/P and global models indicate errors in both T/P data and global tide models. Padman and Fricker (2005) compared ICESat crossover elevations with global and regional tide models for the entire Ross Ice Shelf. R.M.S. differences between ICESat and regional model (RIS_2002) were about 20 cm and differences between ICESat and global models (FES 2004 and GOT 99.2) were about 30 cm, which is consistent with our results.

5.8 Summary and Outlook

The findings from this study are summarized as follows:

1. A number of global and regional ocean tide models were evaluated to assess their accuracy in the Arctic Ocean by comparing their predictions with tide gauge records. Results indicate that the *AOTIM-5 model* performs the best and agrees well with the tide gauge records.

2. The results confirm that the global tide models perform poorly in sea ice-covered areas because the ice-tide interaction were not considered in the model development.

3. The results also confirm that the sea ice does affect the amplitude of major tidal constituents, indicating the ice-tide interaction process rather than the annual period of the astronomical tide-generating forces.

4. The global tide models were assessed by comparing them with satellite altimetry data (T/P) near Churchill. The main source of the differences in the comparison is the ocean tide models. The models have not assimilated altimetry data from the coast and, because of poor bathymetry information, these models have poor accuracy near the coastal regions.

Few recommendations for improving this analysis in the future are given as follows:

1. The AOTIM-5 model was evaluated only near the coast where tide gauge records were available. However, the performance of this model in the ice-covered open ocean still needs to be assessed.

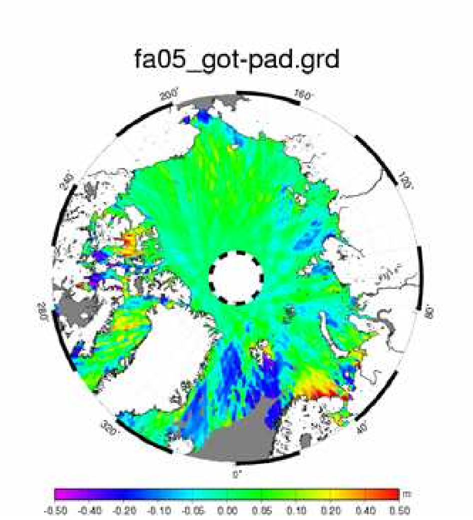

Figure 5.20: Difference between GOT '00 and AOTIM-5 ocean tide models in the Arctic Ocean at each ICESat footprint – Fall 2005 epoch (ArcGICE study).

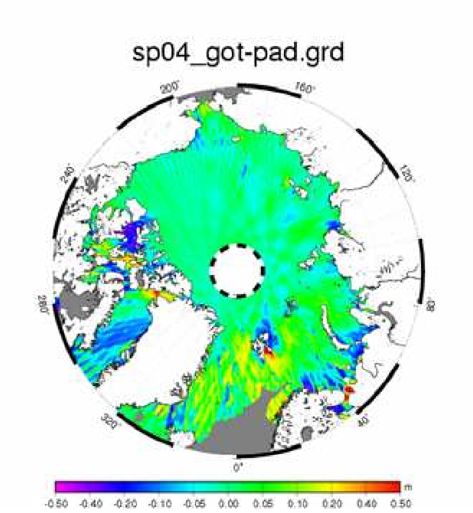

Figure 5.21: Difference between GOT '00 and AOTIM-5 ocean tide models in the Arctic Ocean at each ICESat footprint – Spring 2004 epoch (ArcGICE study).

2. In this study, as a preliminary analysis, global tide models were compared with T/P altimetry data near Churchill. However, satellite altimetry provides a means to evaluate the global tide models in *the entire Arctic basin* (except the polar gap), where the *in-situ* observations are limited to the ocean bottom pressure gauges and moorings. For example, crossover elevation differences from ICESat data can be used to evaluated these models (similar to *Padman and Fricker* (2005)), as it is an independent data set that were not assimilated into these models.

3. Access to *in-situ* data such as ocean bottom pressure gauges or moorings would be valuable to this research. However, multiyear data from such instruments were not available. *Morison et al.* (2007) had deployed two Arctic bottom pressure recorders in the Arctic Ocean, but did not have multiyear data available

at the time of this research. In the future, such an analysis can be carried out to study the effect of ice-tide interaction on the tidal amplitude in the open ocean. This would be an extension of the study carried out by *St-Laurent et al.* (2008) who analyzed data from one year in the open waters of Hudson Bay.

4. The spatial and temporal coverage of the Arctic tide gauge stations must be improved.

5. The TPXO 7.1 model can be used in the future analysis, however, a newer version of the *regional* Arctic Ocean model is expected to have better accuracy.

An outlook into the future generation of Arctic Ocean tide models and recommendations for improving the existing models is given below.

1. *Kowalik and Proshutinsky* (1994) added the ice-tide interactions into their model, KP-94. But they were unable to produce the phase lag and amplitude change due to inaccurate bathymetry in narrow bays at 14 km resolution. *St-Laurent et al.* (2008) carried out a numerical simulation experiment by adding and excluding the under-ice friction in the sea ice-ocean coupled model and found good agreements with moorings data in Hudson Bay. Similar parameterizations could be introduced in the new generation of tide models. However, the effect of ice-ocean stress on the tidal amplitude is still unclear. The physical non-linear interaction between the ice-ocean stress and the ocean tides must be understood in detail before they can be added into the governing hydrodynamic equations. For example, will the tidal range increase or decrease in the presence of sea ice? *St-Laurent et al.* (2008) and *Godin and Barber* (1980) both reported that the tidal range both increased and decreased depending on the location.

Under what conditions (*e.g.*, shape of the bathymetry, type of circulation in the region) will the tidal amplitude be damped and by how much? Under what conditions will the tidal phase be affected (delayed or arrive early)? These questions must be addressed before the models can be constrained by using special hydrodynamic equations that represents the type and extent of modification on the tidal amplitude and phase, under various ice-conditions, bathymetry and circulation patterns.

2. Data from sea ice altimetry can be assimilated into the new generation tide models to constrain the model for the presence of sea ice. ICESat products are available up to 86° N from 2003 to present. (similar to *Padman et al.* (2008)). The data from winter months (Fig. 5.1) could be made available for assimilation into the tide models.

3. The model resolution could be refined similarly to the regional model AOTIM-5 that has a 5-km regular grid resolution. The resolution and accuracy of the Arctic Ocean bathymetry, especially under ice shelves need to be improved to understand tidal mixing and baroclinic tides in these areas.

4. *Padman and Erofeeva* (2004) suggest that the linear-dynamics based model (AODTM) should be developed with comparable accuracy as the AOTIM-5. It is expected to perform significantly better in regions where no tide gauge records are available, *i.e.*, in the central deep Arctic basins, due to the accurate modeling of the dynamics. Such linear-dynamics based modeling should be developed in the future, in contrast to a simple extrapolation of a solution that is constrained by coastal tide gauge data and altimetry.

5. It is possible to define a sea ice flag for a given location based on the sea ice concentration at a particular time of the year. However, care must be taken before defining such flags, as it is only clear that tides are affected by sea ice and *not how* the tides are affected by sea ice cover. *Godin and Barber* (1980) discuss general observations on the modification of tides in different parts of the Canadian Arctic. This can be used as a reference to derive a sea ice flag and first-order corrections for each analyzed tidal constituent.

Conclusion It was shown that the GOT00.2 model has poor accuracy in the Arctic Ocean, and the AOTIM-5 model has the best accuracy under the conditions outlined herein. The differences between these models are large (Fig. 5.20 and 5.21), at ~ 30 cm in coastal areas. Hence, the AOTIM-5 model will be used to replace the GOT00.2 model, which was applied to the GLAS-13 data, to compute the instantaneous sea surface heights. This model has reasonable accuracy for estimating sea ice freeboard heights from ICESat, better than 5 cm in the Arctic Ocean in regions where observations were available for assimilation.

Chapter 6

Validation of ICESat Elevations in Churchill, Manitoba

6.1 Motivation and Objective

Satellite altimetry data are used in a wide range of applications in oceanography (for example, monitoring sea level change, modeling ocean tides, ocean currents and ocean dynamic topography), glaciology (monitoring polar ice sheets), marine geophysics and marine geodesy (see *Fu and Cazanave* (2001)). Such applications require highly accurate and precise altimetric data. Absolute calibration of satellite radar altimeters have been carried out for various missions such as Topex on the Harvest oil platform, off the California coast (*Menard et al.*, 1994), Jason in Aspretto (Ajaccio, southern Corsica) and Cap Senetosa (southern Corsica) (*Bonnefond et al.*, 2003), ERS-1 in Venice, Poseidon in Lampedusa (*Menard et al.*, 1994). As it is evident from the above examples, most of these calibration sites are situated in the low-latitude regions. Hence, they cannot assess the accuracy and precision of those missions (*e.g.*, ERS that covers up to 81° N) over snow and sea ice.

ICESat orbits cover up to 86° N/S that include sub-polar and polar regions. Therefore, altimetry data over ice or sea ice from these missions must be validated at a site that is located at high latitudes. Existing calibration sites are not suitable for this purpose, as they are situated in low-latitude regions. This study, therefore, proposed the area around Churchill, Manitoba as a validation site as it exhibits diverse land cover, lake and sea ice, and ocean.

The primary objective of ICESat is to determine the inter-annual and long-term changes in the polar ice-sheets (mass and volume changes) with high accuracy and precision to assess their impact on global sea level (*Zwally et al.*, 2002). A more specific objective was to reduce the uncertainty in the ice sheet mass balance estimates by achieving an accuracy of better than 2 cm/year over a 100 × 100 km area, averaged over three or more years of seasonal and interannual variability (*Schutz et al.*, 2005). Arctic sea ice freeboard estimation from ICESat, the objective of this research, also requires similar high accuracy, because an error in freeboard estimation translates approximately to a $\sim$6 to 10 times error in sea ice thickness. In order to achieve these ambitious objectives, and in order to ensure that the satellite is continuing to meet those science objectives, dedicated precise calibration and validation experiments must be carried out *throughout* the ICESat missions.

ICESat, and upcoming altimetry missions such as Cryosat-2, measure over a diverse and complex terrain such as snow, sea ice, wetlands, rivers and lakes, forest and vegetation cover, land, and mountains. Although, ICESat was primarily designed to meet the demands of cryospheric research, the GLAS products have a wide range of applications in land topography, hydrology, oceanography, vegetation canopy heights, and atmospheric aerosol distributions. It is important to know the accuracy of ICESat elevations over these surface types before they can be meaningfully used in any application. Since the launch of the ICESat in January 2003, a number efforts have been made to calibrate the Geoscience Laser Altimeter (GLAS) instrument and to assess its accuracy and precision (see section 6.2). However, a comprehensive validation of the GLAS instrument, over such diverse terrain as in this study, has not been made in the past. It is important to note here that this is not an attempt to calibrate the ICESat instrument, but rather to assess the real differences between ICESat and in-situ measurements over very diverse terrain. This would allow us to better assess what is feasible with ICESat and what is not.

The objective of this study is to:

1. assess the accuracy of GLAS elevations over multiple surface types such as sea ice, open water, boreal forests, rock outcrops, tidal flats, and tundra vegetation; and
2. assess the Churchill site, Hudson Bay, as a validation site for multiple altimetry missions such as ICESat, Jason 1 and 2, and upcoming missions Cryosat-2 and ICESat-2.

6.2 Validation of the GLAS instrument

A number of cal/val experiments have been carried out for the GLAS laser altimeter. *Magruder et al.* (2005) validated the time tag and geolocation of the GLAS data in White Sands Space Harbor. They used an electro optical detection system to obtain an independent verification of the time tag, and a passive array of corner cube retro reflectors (CCR) to assess the laser geolocation accuracy. Their results indicate that the time tag accuracy was 3 μsec ± 1 μsec and the horizontal geolocation accuracy was $\sim$10.6±4.5 m.

Fricker et al. (2005) assessed the elevation accuracy of the GLAS altimeter. They conducted GPS ground surveys over the salar de Uyuni salt flats in Bolivia, and created a digital elevation model of the terrain. This DEM was compared with GLAS elevation from twelve ICESat epochs. Salt flats were chosen in their study as a reference target because they were large, stable surfaces and had an albedo similar to that of ice sheets. They found that, under ideal conditions, the GLAS elevations had an absolute accuracy (bias) of $<$2 cm and precision (standard deviation) of $<$3 cm. They also showed that the different environmental conditions (atmospheric forward scattering and surface reflectance) and instrument effects (laser transmit power, detector saturation) between different ICESat epochs impacted the measured elevation accuracy and precision. The ICESat accuracy degraded up to 20 cm, 40 cm and 80 cm under different cloud cover and surface conditions.

Martin et al. (2005) compared terrain models from NASA's Airborne Topographic Mapper (ATM) over the western United States and the Antarctic Dry Valleys with ICESat data to estimate the range bias and pointing errors. They calculated range errors over sloping irregular surfaces by comparing the expected GLAS waveform with the actual waveform. They found that the overall range bias was $\sim$2 cm, which showed no indication of variations between different lasers or ICESat epochs or geographic dependence.

Harding and Carabajal (2005) found good agreement between the received GLAS waveforms and the simulated waveform that was derived using an instrument model applied to a DEM. This analysis also provides information on forested areas and the contribution of canopy and ground to the received waveform. The differences between the two waveforms are possibly due to changes in vegetation cover between the DEM time and ICESat measurement time period such as deciduous leaf-off versus leaf-on conditions, and other instrumental effects such as range delay.

Shuman et al. (2006) performed a preliminary accuracy and precision assessment of GLAS data from Antarctic ice sheets. They showed that for low slopes under clear sky conditions the precision of GLAS data was ~2.1 cm and the relative accuracy was ~ ±14 cm based on crossover differences. *Zwally et al.* (2002) stated that the predicted accuracy for the GLAS elevations is ~ 15 cm on an average over the 70 m footprint area.

6.3 September 2006 Campaign

In this study, Churchill, Manitoba (58.766° N, 94.166° W), located on the south-western coast of the Hudson Bay, was chosen as the validation site. Churchill was chosen and proposed as a suitable site for two reasons. (i) It hosts a variety of surface types such as tidal flats, tundra vegetation, boreal forests, rock outcrops, rivers, sea ice, and open water. Validation of ICESat measurements over all those surface types can, therefore, be accomplished at *one* site. (ii) It is a unique site that maintains a long-term GPS station (~13 years), tide gauge records (~66 years), and absolute gravimetry data (~19 years). These geodetic data can be combined with field measurements such as precise leveling and GPS real-time kinematic survey along the altimeter ground tracks to validate altimetry data. Churchill, because of its unique characteristics described above, is therefore an ideal location for validation of multi-mission data over multiple surface types. It must be understood that this validation can only reach a level that takes into account the fact that the ICESat elevations are an average over a ~ 70 m footprint area, while the surveyed elevations are at a single point. The elevations derived from ICESat and precise leveling are, therefore, not the same physical quantities. Hence, the validation only shows how comparable ICESat and in-situ observations are.

In this research, two field campaigns were carried out in Churchill, Manitoba to determine the accuracy of ICESat over multiple surface types. The first campaign was conducted over land and water in September 2006, and the second campaign was conducted over sea ice in March 2008.

Precise leveling over land A precise leveling survey was conducted in Churchill, Manitoba, during September 3–10, 2006, using a Leica total station. The ICESat orbit information such as satellite overpass time and coordinates of tracks, was obtained from the NASA GLAS science team. The survey was carried out along two ICESat tracks. The spacing was between 50 – 500 m depending on the elevation variability (e.g. the survey measurements were taken at 400–500 m spacing over nearly flat terrain). The two ICESat tracks that were available near the study area are named here as Tidal Flats and Runway (Fig. 6.1 and 6.2). The precise leveling measurements were tied to the permanent GPS benchmark and other geodetic benchmarks that were available.

The elevations from ICESat elevations and precise leveling were transformed to refer to the same vertical datum. ICESat elevations refer to the Topex/Poseidon ellipsoid that was first transformed to refer to the WGS-84 ellipsoid. The transformation was done by subtracting 70 cm from the ICESat ellipsoidal heights (see also section 4.4.1). The geoid undulations were removed from these ellipsoidal heights using the EGM96 geoid model (distributed with the GLAS products) to obtain orthometric

Figure 6.1: ICESat footprints (in red) and leveling survey points (in green) along the TIDAL FLATS track in Churchill, Manitoba, Hudson Bay. ©Google Maps.

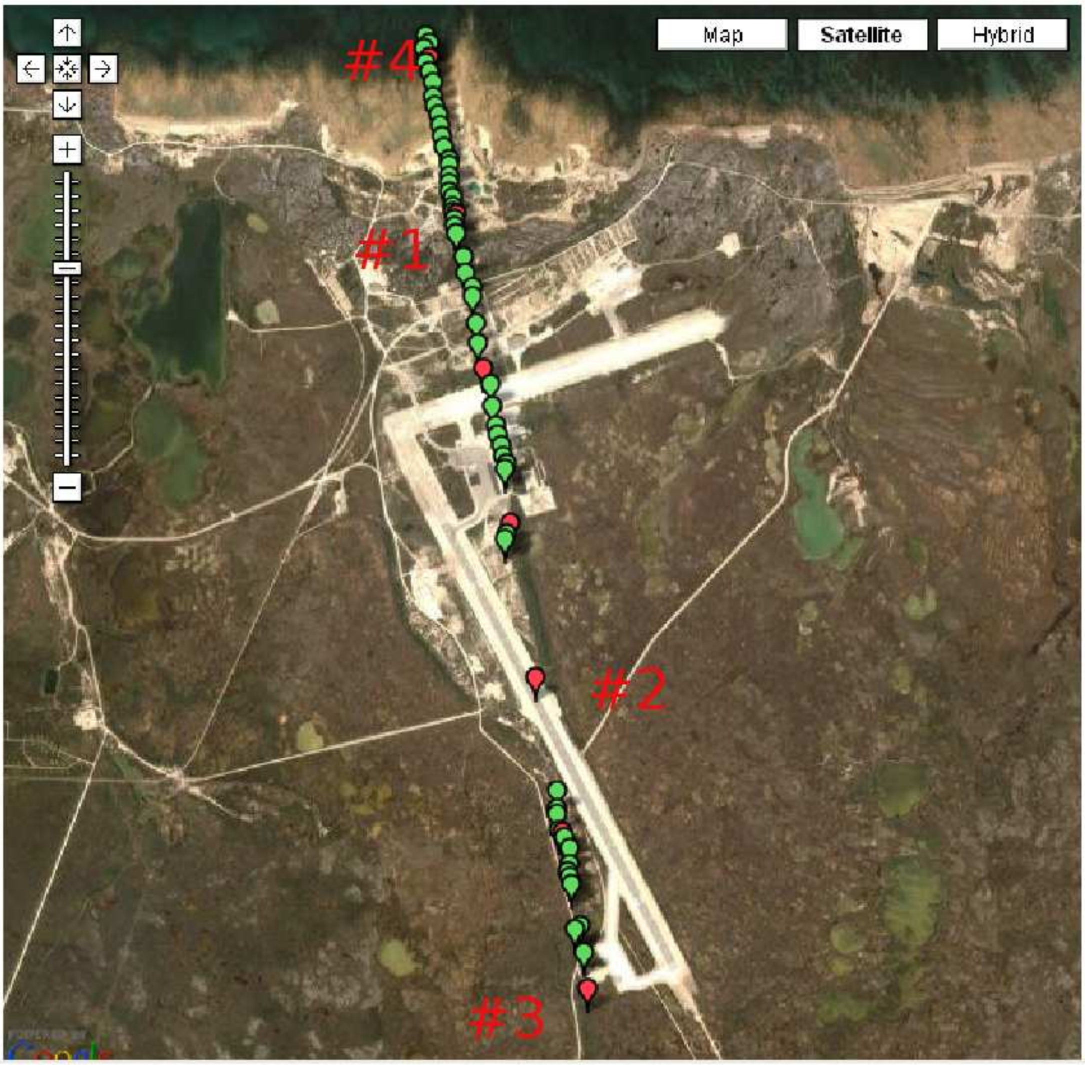

Figure 6.2: ICESat footprints (in red) and leveling survey points (in green) along the RUNWAY track in Churchill, Manitoba, Hudson Bay. #1- Boreal forest, #2-Runway, #3-Wetlands, #4-open water regions. ©2006 Google-Map data

heights. This was then compared with the orthometric heights obtained from the precise leveling survey. The accuracies of the precise leveling, ICESat elevations and the geoid model affect how well the two measurements agree. The ICESat footprint size is large, ∼70 m, and the variability of the vertical structure of the canopy and ground within this footprint area is expected to be on the same scale as the accuracies of the geoid model, leveling survey and ICESat. Hence, the comparison between the precise leveling measurements and ICESat elevations is reasonable, however, a cm-level agreement cannot be expected, as in some of the studies mentioned above (section 6.2) that were conducted in flat and homogeneous regions. The objective of this validation is to estimate the real differences between the ICESat measurements (at 70 m spatial resolution) and in-situ measurements (point measurements), over topographically complex surfaces.

6.3.1 Accuracy over land and water

The two ICESat tracks, referred to as (i) Tidal flats (Fig. 6.1) and (ii) Runway (Fig. 6.2) passed through various surface types such as tidal flats (Fig. 6.3), rock outcrops (Fig. 6.4), tundra (Fig. 6.5), boreal forests (Fig. 6.6), open water (Fig. 6.7) and the Airport Runway. ICESat data from all epochs that were available at the time of this study were used to compare the ICESat measurements with the field measurements. However, ICESat tracks from most of the epochs were more than 100 metres away from the surveyed track. The topography, especially near the Runway track, changes considerably within this 100 m distance. Hence, only March 2004 and March 2006 mission phase data were used in the analysis. The comparisons between the survey measurements from September 2006 and ICESat measurements from March 2004/2006 are expected to be valid as the study area is considered stable

Figure 6.3: Tidal flats.

Figure 6.4: Rock outcrops.

Figure 6.5: Tundra vegetation.

Figure 6.6: Boreal forests.

Figure 6.7: Open water.

at most of the regions – no change or developments in the surface topography except possible changes in the water levels in the tidal flats and vegetation growth.

The differences between the survey measurements and the ICESat data are plotted against the profile distance in Fig. 6.8 for the Tidal Flats track and Fig. 6.9 for the Runway track. Orthometric heights were used in the comparison. Along the Tidal Flats track, the two measurements agree within ~30 cm. Along the Runway track, the accuracy decreased as there were more complex surfaces.

Table 6.1: Mean differences in the orthometric heights obtained from leveling survey and ICESat over a variety of surface types.

Surface Type	Mean Difference (m)
Wetlands	0.60
Runway	0.20
Boreal forests	0.90
Open Ocean	>1.0
Tidal flats	0.30

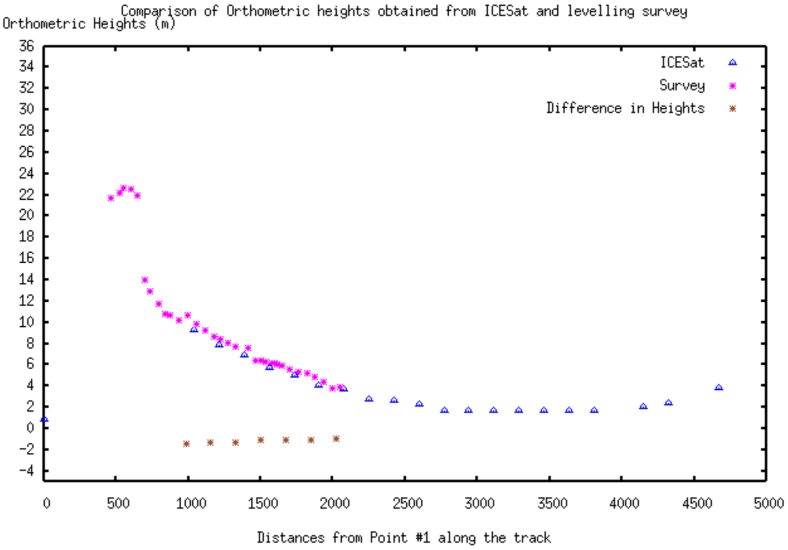

Figure 6.8: Differences (brown) between the orthometric heights obtained from leveling survey (purple) and ICESat (blue) along the TIDAL FLATS track.

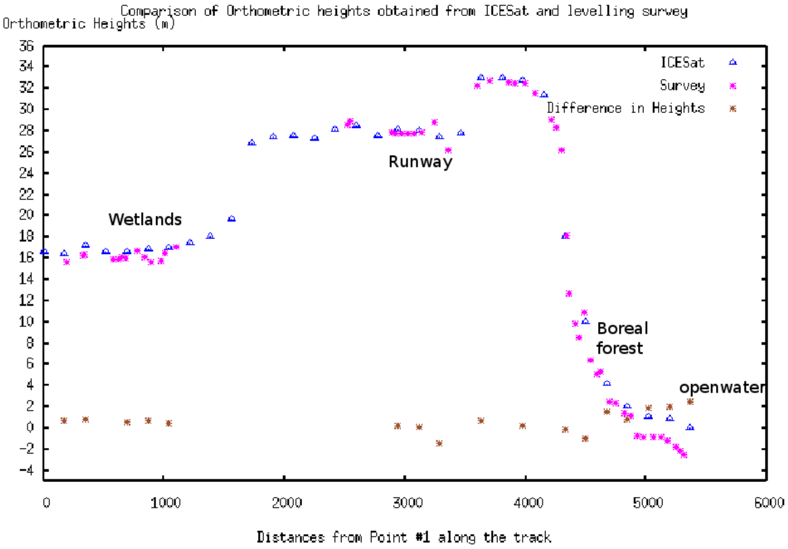

Figure 6.9: Differences (brown) between the orthometric heights obtained from leveling survey (purple) and ICESat (blue) along the RUNWAY track.

The results are summarized as follows (Table 6.1).

- Over flat areas such as the Airport runway, there was good agreement between the precise leveling measurements and ICESat. The differences were within ∼20 cm on average. Over complex surfaces such as boreal forests, the accuracy degraded to ∼90 cm. Backscatter from the ICESat probably originated from the tree canopy (branches, tree crown, etc.; tree height >3 m) because the laser altimeter does not fully penetrate through the vegetation cover. In contrast, the survey measurements were made on the ground. These differences could have caused the large ∼90 cm differences near boreal forests.

- The difference between the two data sets were the largest near the coast among all surface types, >1 m. This large difference can be explained by ocean tides. The tidal range near Churchill is approximately ∼4 m. Because the time of measurements for the two data sets are different (survey data – September 2006; ICESat data – March 2004), most of the differences can be explained by differences in the tide levels and piling up of sea ice cover near the coast in March. At the time of precise leveling survey (September 8, 2006 at 14:00 local time), the tide level was approximately 0.52 m (MEDS database) and the ICESat measurement (March 5, 2004 at 16:00 local time) 2.44 m. Hence, there was a 2 m difference in the tide water level between those measurement periods.

6.4 March 2008 Campaign

A GPS RTK (real-time kinematic) survey was carried out in Churchill, Manitoba during March 4-10, 2008. The ICESat orbit information was obtained from the NASA

GLAS science team. The expected ICESat overpass near Churchill (58.766° N, 94.166° W) was on March 5, 2008 at 22:32 UTC. RADARSAT ScanSAR Wide imagery, with a spatial resolution of 100 m and a scene size of 500 km, was acquired from the Canadian Ice Services (Fig. 6.10). The image was acquired for the Churchill study area in order to plan the survey based on the sea ice conditions. Fig. 6.11 shows the lead formation about 2 km from the Churchill coast. Therefore, it was possible to survey only about 1.5 km of the land-fast sea ice underneath the ICESat track (Fig. 6.12). This is a reccurring lead formation in this area. Therefore, in the future, a longer ICESat track beyond the lead formation can be surveyed by using the helicopter means of transportation to get across the lead. Although the field campaign was planned to carry out GPS survey for 8 days, the weather conditions were not ideal. Four days were lost due to a snow storm. In the end, the survey was carried out over only a three day period. This was just the amount of the time taken to survey along a 1.5 km stretch of the ICESat track (*i.e.*, only 20 or less ICESat footprints). The ICESat footprints that were within a 50 m distance from the surveyed points were used in the comparison.

6.4.1 Accuracy over sea ice

The measured GPS RTK elevations were then compared with the ICESat GLAS-06 elevation product that was acquired from NSIDC. The differences between these two data sets were approximately 2.0 m (Fig. 6.13).

The GPS RTK survey along this track was carried out on March 8, 2008 between 12:00 – 16:00 local time. ICESat overpass was on March 5, 2008 at ∼22:40 UTC. The two measurements were, therefore, taken under different environmental conditions

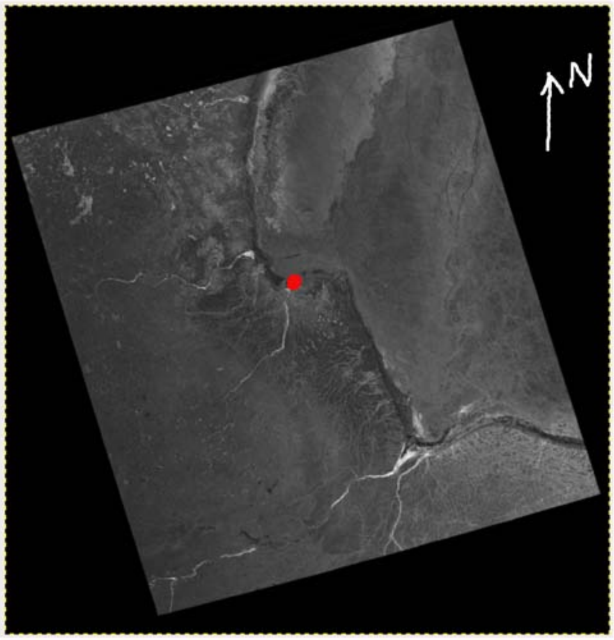

Figure 6.10: RADARSAT ScanSAR Wide scene showing the sea ice conditions in the Hudson Bay region (and Churchill (red)) on March 4, 2008. Spatial resolution – 100 m and scene size – 500 km. Image provided by the Canadian Ice Services.

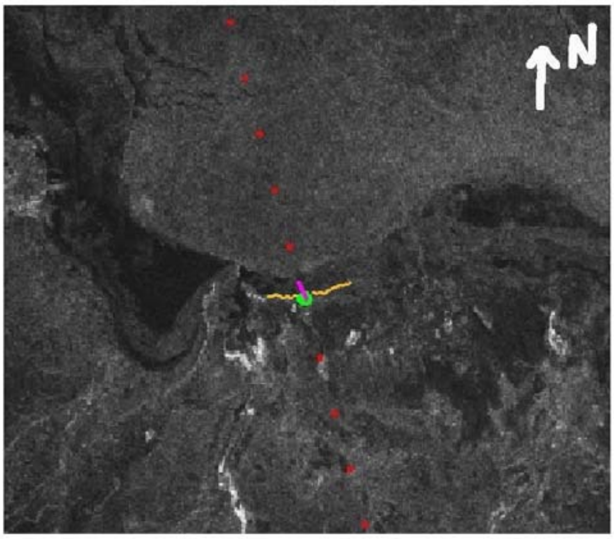

Figure 6.11: RADARSAT ScanSAR Wide scene showing the sea ice conditions on March 4, 2008 near Churchill (green). The ICESat track is plotted in red and the 1.5 km GPS RTK survey track is shown in purple. The Churchill coastline is marked in yellow.

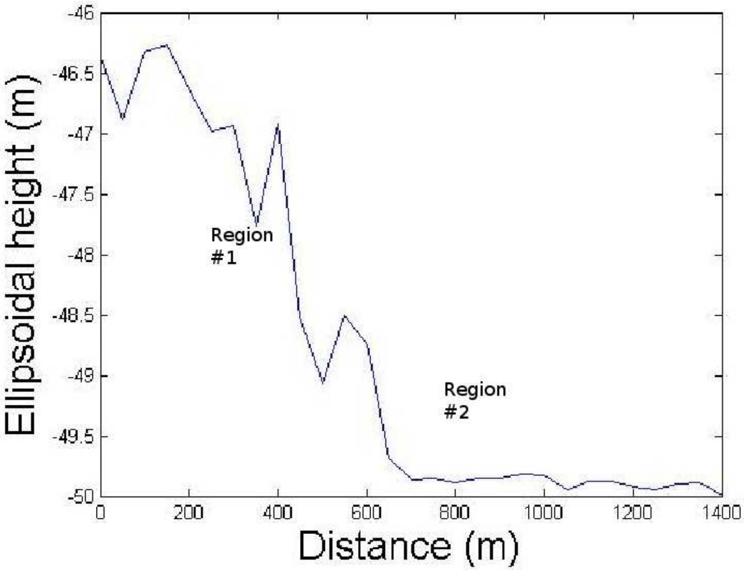

Figure 6.12: Ellipsoidal heights measured over the land-fast sea ice near Churchill, using GPS RTK survey along the ICESat track. #1 is a rougher fast-ice region that was within 400 m from the coast. #2 is a relatively flat fast-ice region approximately 800 m away from the coast.

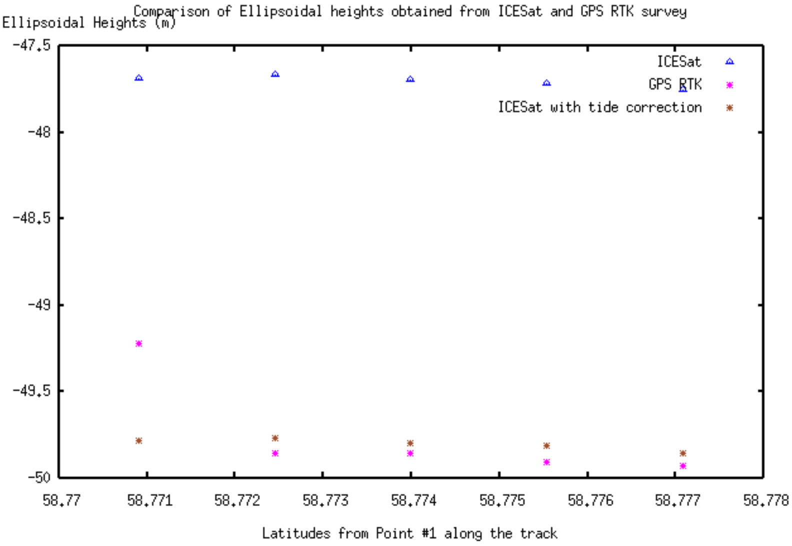

Figure 6.13: Comparison between the ellipsoidal heights obtained from GPS RTK survey (purple) and ICESat (blue) near Churchill. ICESat elevations after applying the tide-difference (between ICESat measurement and GPS measurement) correction are plotted in brown.

such as ocean tides and atmospheric pressure. These differences in the environmental conditions will be reflected in the differences between these measurements. Ocean tides are particularly large near the coast and must be measured along with the GPS RTK. Due to limitations in the equipment that was available, an extra station could not be set up to measure tides over the time period of the survey. However, tide water levels were obtained from MEDS. On March 5, 2008 at 22:40 UTC the tide water level was 3.4 m and on March 8, 2008 between 12:00 – 16:00 local time, the tide water level ranged from 1.3 m to 0.3 m and back up to 1.1 m. The difference in tide water levels between the two measurement time is $\sim$ 2.1 m.

In order to improve the comparison, the ocean tides must be removed from both data sets (GPS RTK and ICESat). The use of ocean tide models will only introduce additional errors as these models do not have acceptable accuracy near the coast and in the ice-covered oceans (see Chapter 5). Therefore, as a simple correction, the difference in the tide water level was applied to the heights measured from the GPS, *i.e.*, 2.1 m were removed from the GPS heights. After applying the corrections for ocean tides, the two data sets show good agreement with differences <10 cm. Other effects such as atmospheric pressure will also impact the comparison, particularly over sea ice. It is relevant to consider these effects for validation of ICESat over sea ice, because the satellite measures about 7 km per second. It would take approximately 3 days to measure over a 7 km distance with the GPS RTK depending on the ice conditions. Hence, the environmental conditions would be different between these data sets and should be corrected for or taken into consideration when analyzing the differences between them.

6.4.2 Sea ice roughness

Sea ice roughness estimates were also derived from the RTK measurements. The classical approach to measure the sea ice surface roughness is to compute the variance of the surface elevations around its mean value and to apply Fourier spectrum analysis to derive the roughness distribution at a range of wavelengths (*i.e.*, *Adolphs* (1999)). In this study, the roughness estimates were calculated by simply deriving the variance and standard deviation of the land-fast sea ice regions. As expected, the roughness was higher at regions closer to the coast, ~0.263 m (Fig. 6.16 and region 1 in Fig. 6.12). Sea ice roughness at regions about 1.5 km away from the coast was ~0.183 m (Fig. 6.17 and region 2 in Fig. 6.12).

Figs. 6.14 and 6.15 show the ICESat elevation profile and the received waveform characteristics. The sharp decline in elevation from the coast to the open ocean is the

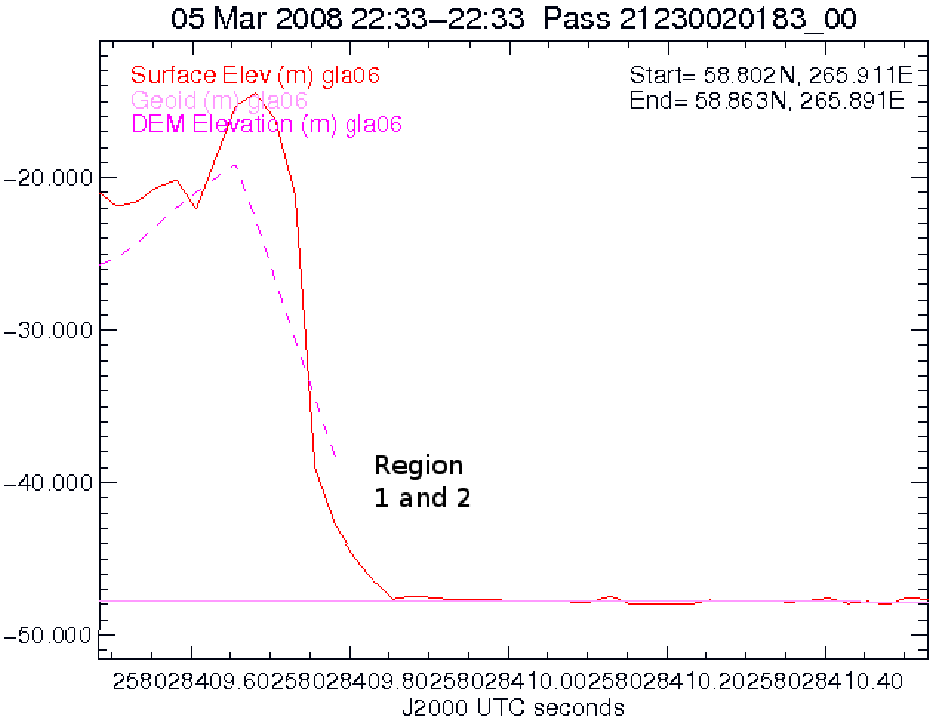

Figure 6.14: GLAS elevation profile (red) over land-fast ice (region of GPS RTK survey) near Churchill obtained using the NSIDC GLAS visualizer software.

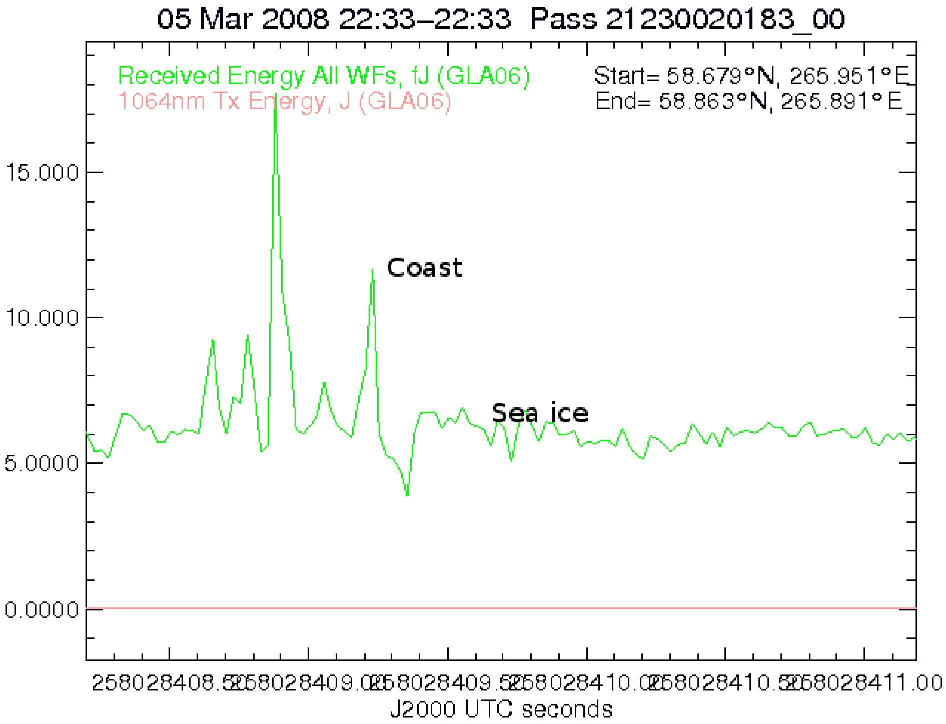

Figure 6.15: GLAS waveform characteristics (received energy in green) over land-fast ice (region of GPS RTK survey) near Churchill obtained using the NSIDC GLAS visualizer software.

Figure 6.16: A rougher fast-ice region approximately within a 400 m distance from the Churchill coast.

Figure 6.17: A relatively flat fast-ice region approximately 800 m away from the Churchill coast.

area that was surveyed with GPS RTK (see Fig. 6.12). The waveform characteristics show the stronger backscatter from the coastal regions (roughness 0.263 m, region 1 in Fig. 6.12) and a moderate backscatter corresponding to the relatively flat sea ice about 1.5 km away from the coast (roughness 0.183 m, region 2 in Fig. 6.12).

6.5 Summary and Outlook

ICESat laser altimeter measurements were validated over *multiple surfaces types* in Churchill, Manitoba for the first time. The findings from this investigative study are summarized below.

- The differences between the precise leveling and ICESat measurements were large in (i) topographically complex areas because ICESat did not reflect off the ground (rather from the tree canopy) while leveling measurements were taken on the ground, and (ii) the coastal areas due to differences in the surface characteristics (survey was carried out in September during open water conditions and ICESat measurements are from March mission phase under sea ice conditions).
- *Fricker et al.* (2005) carried out GPS measurements over salar de Uyuni salt flats, Bolivia. They surveyed a 54 km × 45 km area, created a digital elevation model and compared it with all the ICESat epochs that were available. A similar study can be carried out in Churchill both over land and sea ice. GPS RTK survey technique is less time consuming when compared to precise leveling and can be used to survey a larger grid area. Over land, because the topography does not change significantly, survey over a grid area will provide more ICESat

footprints for comparison, as more ICESat epochs (and more repeat tracks) will be available. Statistics can be derived based on more samples. Precision estimates can also be derived when more measurements are available. However, this technique cannot be followed over sea ice, because tidal variations will affect the comparison between ICESat and survey measurements. But, a larger width of the predicted ICESat track can be surveyed to ensure that the survey measurements are available along the *actual* ICESat track. In both field campaigns (land and sea ice), the actual ICESat track sometimes deviated from the predicted track by about $\sim$ 100 m. Hence, by surveying over a wider track, it can be ensured that GPS RTK survey measurements are available at the actual ICESat footprint/track. The differences in the time of measurements between RTK and ICESat will not impact the comparison significantly over land, as it would over sea ice, because the land is relatively more stable.

- In conclusion, Churchill is an ideal validation site for multiple satellite altimetry missions (current and upcoming) that will complement the traditional tide gauge-altimetry comparisons. The Churchill site is relatively easily accessible compared to the Arctic Ocean (which is an extreme challenging environment). Moreover, it is a host to a variety of complex surface types and long-term geodetic observation systems. Therefore, it is possible to carry out accuracy and precision assessment of altimetry measurements over many surface types, in *one* inexpensive and short-term planned campaign. This field work was an investigative analysis to assess the feasibility of such studies.

Chapter 7

Arctic Sea Ice Freeboard Heights from ICESat – Results

The sea ice freeboard heights derived from ICESat laser altimetry, using the method described in Chapter 4, are presented in this Chapter. The sea ice freeboards were derived from 10 ICESat epochs using the GLAS-13 release 28 data. The data analyses were carried out at different stages: (i) An examination of the regional, seasonal and inter-annual variability in the Arctic sea ice freeboards was performed. (ii) The freeboard maps were compared with other studies and a sensitivity analysis was performed to estimate the uncertainty in the freeboard retrieval procedure. (iii) The probability density distribution of the sea ice freeboards in the Arctic Ocean was also analyzed to determine the dominant ice type and the amount of significantly deformed ice cover. (iv) The sea ice growth during the freeze-up season was examined using GLAS-13 release 26 data from the ICESat October 2003 epoch. (v) A regional sea ice thickness distribution was computed from the sea ice freeboards and compared with the sea ice thickness distribution from the Helicopter-based Electromagnetic Induction technique. (vi) Finally, a sensitivity analysis was carried out to examine the uncertainty in the sea ice thickness estimates. The results from the above analyses are presented in the following sections.

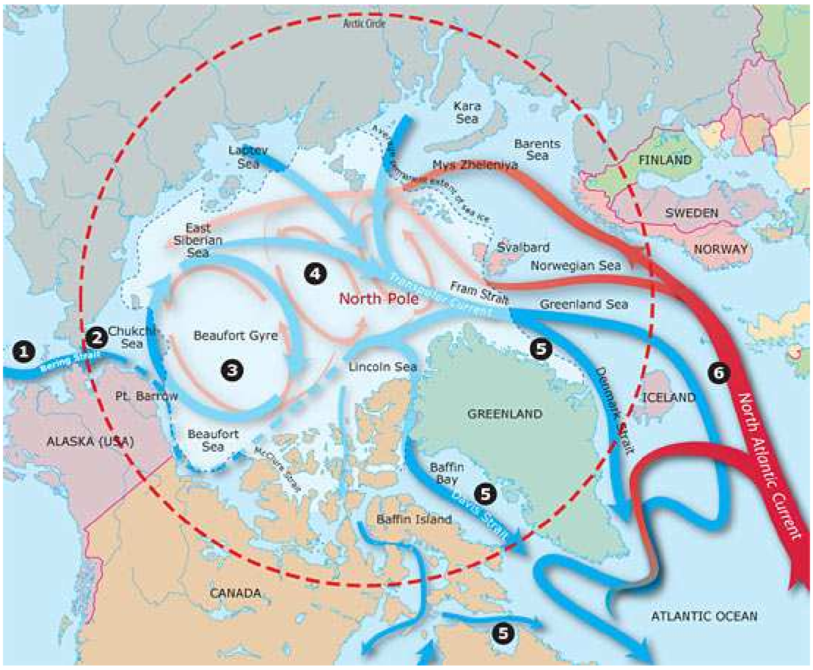

Figure 7.1: The Arctic Ocean including marginal seas and the Transpolar current. Credit: WHOI

The Arctic Ocean System

A brief overview of the different regions in the Arctic Ocean, which will be referred to in the following sections, is provided here. The Arctic Ocean has a total area of about 15 million km^2 that includes the Arctic basin and the marginal seas, namely Baffin Bay, Barents Sea, Beaufort Sea, Chukchi Sea, East Siberian Sea, Greenland Sea, Hudson Bay, Hudson Strait, Kara Sea, Laptev Sea, and the Northwest Passage (Fig. 7.1). It is essentially an enclosed basin, and the exchange of waters with the Pacific and the Atlantic Ocean occurs through the Bering Strait and the Fram Strait/Davis Strait/Norwegian seas, respectively. It has a coastline of about 45,000 km and an average depth of 4,600 m. The sea ice cover in the Arctic Ocean approximately reaches an area of about 15 million km^2 during the winter seasonal maximum, and reduces to $\sim$ 4 million km^2 during the Summer seasonal minimum (Fig. 1.1).

7.1 Arctic sea ice freeboards

The total freeboard in the Arctic Ocean were computed using data from 10 ICESat epochs. The most recent release 28 GLAS-13 data was available for only 10 epochs at the time of this study. In this freeboard retrieval, all corrections that were discussed in section 4.4 were applied, including the mean dynamic topography and inverse barometric effect (Fig. 7.4). Table 7.1 summarizes the mean and the standard deviation of the freeboard distribution for 10 ICESat epochs.

Table 7.1: Mean and standard deviation of the total freeboard for 10 ICESat mission phases

Month-Year	Mean (cm)	Std. dev. (cm)
Oct-Nov-03	35.7	26.7
Feb-Mar-04	38.7	28.1
Oct-Nov-04	35.9	28.0
Feb-Mar-05	39.1	31.1
May-Jun-05	46.2	31.9
Oct-Nov-05	34.7	27.5
Feb-Mar-06	40.2	30.6
May-Jun-06	43.1	31.4
Oct-Nov-06	40.6	29.1
Mar-Apr-07	35.7	28.2

The mean of the total freeboard was calculated excluding the negative freeboards that were present in the freeboard distribution. Because the instantaneous sea surface height is modeled in this method, at some ICESat footprint locations, the sea surface heights were higher than the GLAS elevations due to errors in the component models. As a result, the estimated freeboards were negative at those ICESat footprints (plotted in color blue, Fig. 7.2). These negative freeboards were removed in the calculation of the mean and standard deviation of the total freeboard distribution because they will erroneously lower the mean of the total freeboard. Similar issues occurred in other studies (*e.g.*, *Farrell et al.* (2009)) as well, where such negatives freeboards were ignored in the freeboard distribution.

In this study, the mean of the total freeboard seemed to increase from 34.7 cm in Fall (October 2005) to 40.2 cm in Winter (February 2006). This indicates a ∼5.5 cm growth in the total sea ice freeboard over the four month duration of October to February. The increase in the mean of the total freeboard can be attributed to (i) snow accumulation and (ii) ice growth (most likely in the seasonal ice zone rather than the multi-year ice zone, because the ice growth rate is higher over thin ice than thicker ice; see section 2.1.2).

7.1.1 Comparison of freeboard estimates with other studies

The freeboard results are compared to the findings from other studies. (i) *Kwok et al.* (2007) found a 7.5 cm increase in the mean freeboard. The mean freeboard was 27.5 cm in October 2005 and 35.0 cm in February 2006. (ii) *Kwok and Cunningham* (2008) found a 7 cm increase in the mean freeboard (also see Fig. 4.12). The mean freeboard was 37.6 cm in October 2005 and 44.6 cm in February 2006. (iii) *Farrell et al.* (2009) found a ∼ 10 cm increase in the total freeboard with mean freeboards of ∼ 25.4 cm in October 2005 and 35.3 cm in February 2006. Most of the studies have presented the total freeboard for only October 2005 and February 2006 epochs, as a reference, to demonstrate their freeboard retrieval procedure. Hence, the results from this thesis were compared with other studies for the same time period.

Discussion

The differences in the calculated mean of the total freeboard between different studies are due to the different procedures adopted to estimate the instantaneous sea surface height (SSH). *Kwok et al.* (2007) estimated the instantaneous sea surface height within every 25 km ICESat along-track distance. The sea surface height was derived by averaging three types of SSH estimates: (i) GLAS elevations from new openings and leads that were identified using coincident SAR imageries, (ii) open water and re-frozen leads identified using reflectivities that are lower than the background snow-covered sea ice, *and* data points whose elevations that are below a certain threshold when compared to the local mean surface, (iii) under the only condition that the elevations are below a certain threshold when compared to the local mean surface. *Kwok and Cunningham* (2008) used a similar method with an additional nominal adjustment for the presence of snow layer over the recently-refrozen thin ice in leads/open water regions. *Farrell et al.* (2009) developed a lead detection algorithm that identifies the ICESat waveforms that originate from leads and thin ice. Their method used a combination of surface elevations, surface reflectivity *and* the shape of the reflected waveforms. In this study, the instantaneous sea surface height was estimated using a combination of geodetic and oceanographic models (section 4.4). These differences in the method of SSH estimation led to differences in the derived freeboard distribution from GLAS data.

Another inference from the comparison of results with other studies is that the freeboard maps obtained from this study are more rough. Although the gridding of the freeboard heights smooths the data, the SSH was calculated at each ICESat-GLAS footprint ($\sim$ 70 m) in this study. Only the points where SSH exceeded the GLAS elevation were rejected. In contrast, the SSH was estimated at every 25 km along-track distance in *Kwok et al.* (2007) and *Kwok and Cunningham* (2008) and at every 50 km along-track distance in *Farrell et al.* (2009). Therefore, only 5073/7442 cells were available in *Kwok et al.* (2007), and 4973/5299 cells were available in *Farrell et al.* (2009) to derive SSH during October 2005 and February 2006. Hence, the SSH from these studies were smoother compared to this study. Because SSH can be computed at every ICESat footprint in this study, more data points were used in the calculation of the Arctic sea ice freeboard distribution, N = 2560643/5135014, whereas N was only 1233909/2228106 in *Kwok and Cunningham* (2008) and 2156429/3749082 in *Farrell et al.* (2009) for October 2005 and February 2006. The freeboard grids derived from this study are rougher because of the ICESat individual measurements ($\sim$ 70 m) and not because of the models used to derive the sea surface height (which have large spatial resolutions of $\sim 40km$). The SSH is derived at each ICESat footprint (70 m), consequently the derived sea ice freeboard maps from the ICESat data are also rough and, not due to the methodology adopted in this study.

In summary, the estimated sea ice freeboards in Oct-05/Feb-06 (mean: 34.7/40.2 cm) show good agreement with the *Kwok and Cunningham* (2008) method (mean: 37.6/44.6 cm). However, there are differences in the derived sea ice freeboard due to differences in the method used to estimate the SSH. In general, the derived freeboards in this study show reasonable distribution in the Arctic Ocean that is consistent with the expected values in the different parts of the Arctic Ocean. They are discussed in more detail in the following sections.

7.1.2 Comparison of freeboard with QuikSCAT backscatter fields

The derived freeboard heights at each ICESat footprint were gridded using Generic Mapping Tools (*Wessel and Smith*, 1991) onto a 10' × 5' grid. The freeboard grids were compared with the QuikSCAT backscatter fields. QuikSCAT is a polar-orbiting satellite that carries a Ku-band scatterometer, known as the SeaWinds instrument. The scatterometer provides daily coverage over the entire Arctic Ocean at H- and V- polarizations with a swath width of $\sim$ 1800 km. It was launched in June 1999. Centre ERS d'Archivage et de Traitement archives and distributes QuikSCAT Polar Sea Ice (PSI) backscatter fields with a uniform 12.5 km × 12.5 km grid resolution. A comprehensive description of the product formats and PSI grids can be found in the PSI user manual provided by the Department of Oceanography from Space (CERSAT) at IFREMER (*Ezraty and Piolle* (2001)).

Figs. 7.2 – 7.5 show the comparison between freeboard and QuikSCAT backscatter fields. There is a good agreement between regions with thicker freeboard ($>$ 40 cm) and regions with higher backscatter (> -14 dB). These regions (*i.e.*, North of the Prince Patrick Island, Ellesmere Island and Greenland) correspond to the multi-year ice zones in the Arctic Ocean. Higher backscatter in these regions can be attributed to the rough topography of the multi-year ice. First-year ice (seasonal ice zone) is relatively flat and smooth when compared to multi-year ice and, therefore, backscatter from these regions is relatively low. Such low backscatter can be observed in the Russian Arctic (North of the Barents and Kara seas), where the freeboards are thinner ($<$ 40 cm). The comparisons with the QuikSCAT backscatter fields in this study show that the ICESat-derived freeboard distribution are reasonable at basin-wide scales.

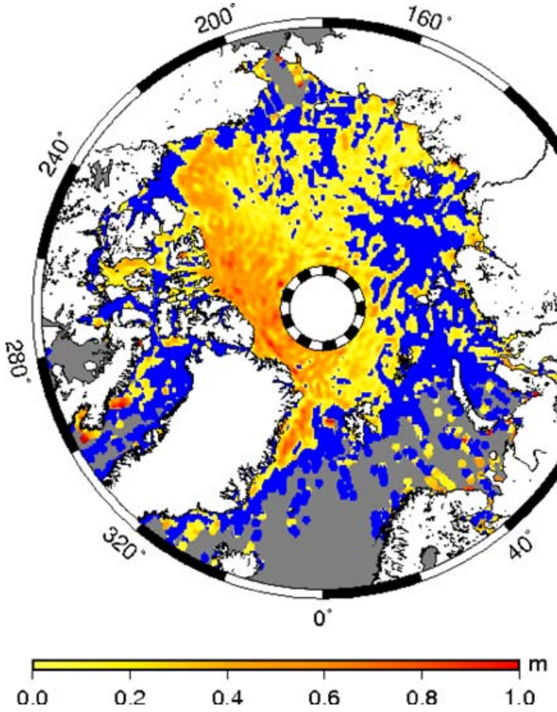

Figure 7.2: Sea ice freeboard during October-November 2005 ICESat phase

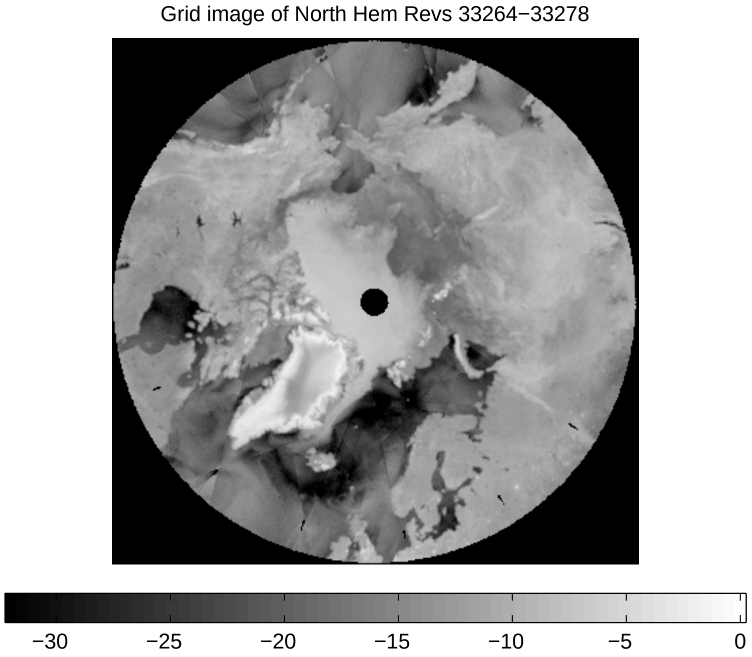

Figure 7.3: Sea ice backscatter field on November 11, 2005 from QuikSCAT

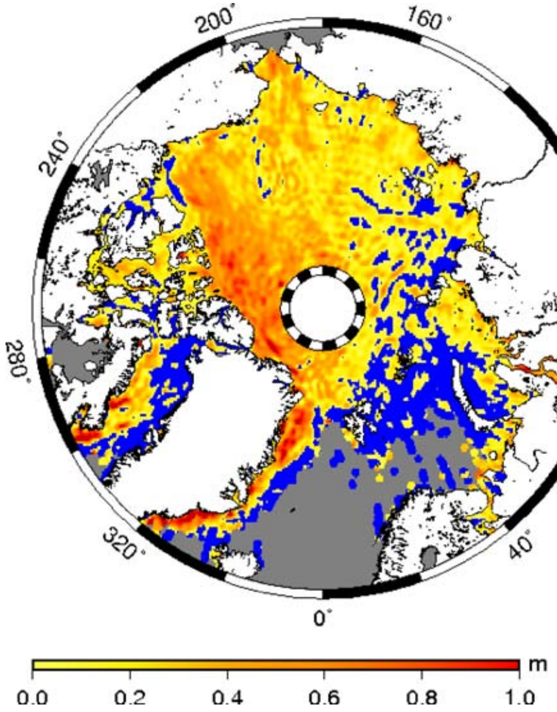

Figure 7.4: Sea ice freeboard during February-March 2006 ICESat phase

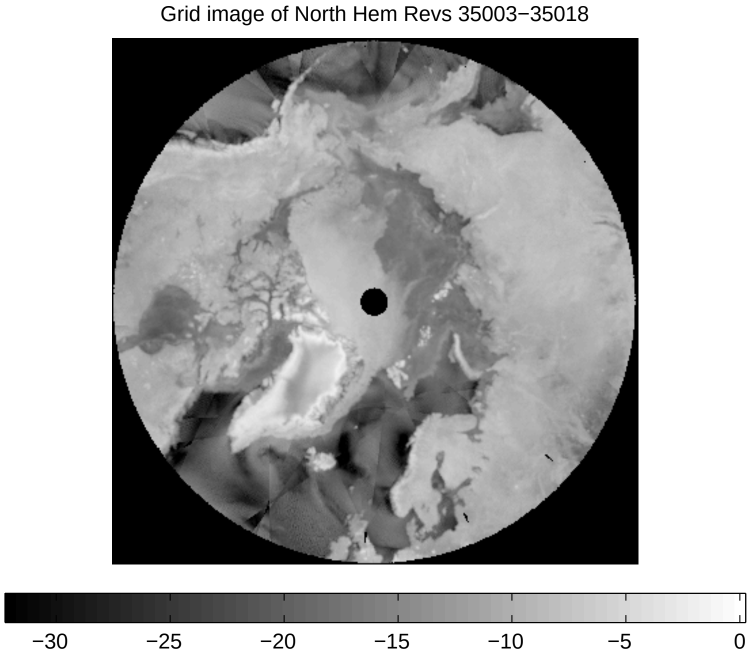

Figure 7.5: Sea ice backscatter field on March 10, 2006 from QuikSCAT

7.1.3 Regional, seasonal and interannual variations in the Arctic sea ice freeboard

Regional variations

1. From Fig. 7.4, it can be seen that the sea ice cover is concentrated in the Arctic basin. The ice cover advances southward through three meridional tongues in the Eastern parts of Greenland, Canada and Asia, where the cold currents (East Greenland, Labrador and Oyashio currents) flow. The ice cover retreats northward in the regions of warm currents (North Atlantic and Kuroshio currents). Hence, the sea ice extent in these regions exhibit major departure from the latitudinal zonality that is otherwise expected (*Mironov et al.*, 2007).

2. The marginal Arctic seas (Barents, Kara and Laptev seas) are the largest ice production regions in the Arctic Ocean (Fig. 7.4). These regions are seasonal ice zones (*i.e.*, ice-free during Summer, see the next discussion on Seasonal variations), hence, the ice grows at a faster rate in these regions ($\sim$ 10 cm over 10 days during Winter). Due to wind forcing in these regions, the newly formed young first-year ice (typically $\sim$ 20 cm in thickness (*Mironov et al.*, 2007) is continuously pushed northwards where it joins the sea ice exiting from the Transpolar Drift into the Greenland seas (see the mean ice drift pattern in Fig. 7.6 and 7.7). Hence, these regions exhibit thinner freeboards ($<$ 20 cm that includes the thickness of the overlying snow layer).

3. The Beaufort Gyre is an anti-cyclonic gyre, therefore, the sea ice circulation in this region has a convergent motion which leads to heavy ridging, and rubble ice formation. The sea ice exiting the Beaufort Gyre circulation joins the persistent Transpolar Drift. This circulation pattern pushes the sea ice towards north of

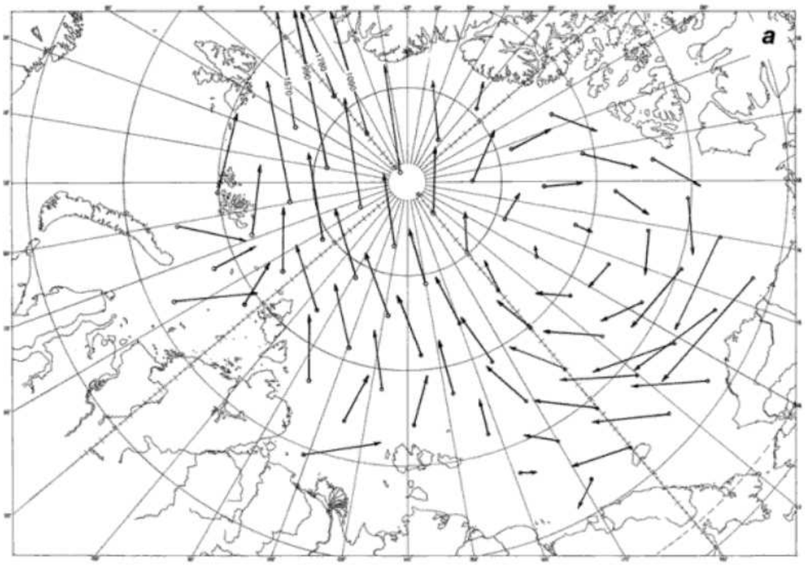

Figure 7.6: Mean ice drift pattern during Winter from *Mironov et al.* (2007)

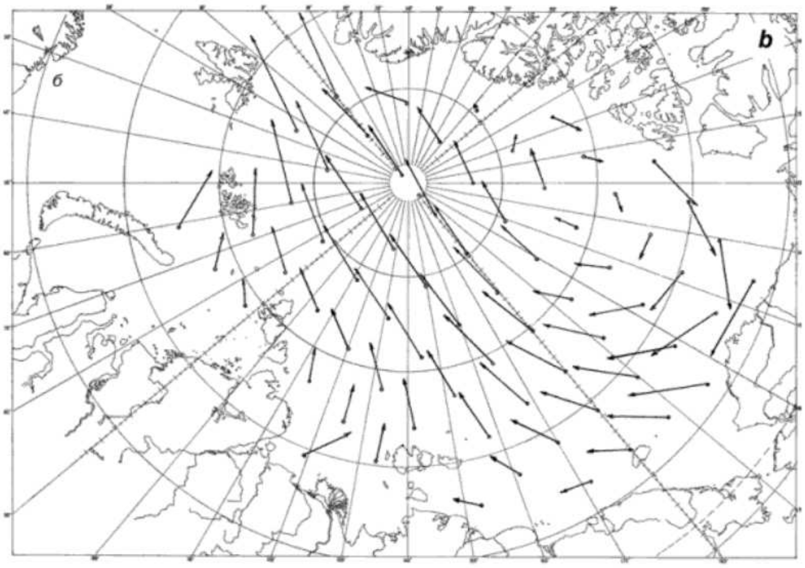

Figure 7.7: Mean ice drift pattern during Summer from *Mironov et al.* (2007)

Greenland and Canada. Hence, thicker total ice freeboards, $\sim 0.5 - 1.0$ m, can be seen in these regions. These are the perennial ice zones in the Arctic Ocean with multi-year ice cover (typically 7-8 m thick). The higher ice thickness in these regions is mainly due to sea ice dynamics rather than thermodynamical ice growth.

4. The sea ice exiting through the Fram Strait from the Arctic Ocean exhibits mixed ice types. The young first-year ice from the regions of ice production (Russian Arctic) and the multi-year ice that circulated in the Arctic basin and exiting through the Transpolar Drift can be found in the Greenland Seas and Fram Strait regions. The sea ice in these regions is typically thicker than the marginal Arctic seas and thinner than the perennial ice zones in the Arctic basin. Fig. 7.4 shows $>$ 40 cm total freeboard in these regions.

5. *Mironov et al.* (2007) summarized that first-year ice cover is predominantly found in the Northern Sea Route, and second-year ice in the East Siberian Sea. They also noted that a number of flaw polynyas (open water regions or young ice up to 30 cm thick, spanning about 1000 km^2 are formed between the fast-ice covered regions of the Russian Arctic and the drifting ice in the Central Arctic (Fig. 7.4). Most of these polynyas are stable with the frequency of occurrence $>$ 75 % (for more details on the number of polynyas, their average width/length/area, see Table 2.16 in *Mironov et al.* (2007)). Such features were also found in this study. In Fig. 7.4, the landfast-ice covered regions can be seen in Kara seas and East Siberian seas. A number of open water regions can also be seen north of these landfast-ice regions.

6. The regional variations in the total freeboard also includes the variations in the snow accumulation.

Seasonal variations

Figs. 7.8, 7.9, 7.10, 7.11, 7.12 and 7.13 show the seasonal differences in the total freeboard distribution in the Arctic Ocean observed using ICESat-GLAS data.

1. Figs. 7.9 and 7.12 shows the extent of sea ice cover since it reached its seasonal minimum (both in terms of thickness and area) in September. The sea ice begins to grow thermodynamically during the freeze-up period (see section 2.1.1) in October. Snow accumulation also begins to occur. The regions of seasonal ice zone show < 10 cm total freeboard. The typical ice thickness in these regions is ~ 20 cm (equivalent to 2 to 3.3 cm ice freeboard calculated using a conversion factor, $K = 6$ or 10, Eqn. 3.2).

2. The sea ice continues to grow in March-April (Fig. 7.10 and 7.13). The first-year ice is typically 1.2 – 1.6 m thick. For example, in some parts of East Siberian seas the freeboard is ~ 20 cm (equivalent to ~ 1.2 m thickness).

3. The melt onset begins in June when there is an increase in the incoming solar radiation and propagates from the South to North. Hence, the ice cover in marginal seas begin to melt first (Fig. 7.11). Significant reduction in the sea ice cover in the central Arctic can only be seen during September.

4. The ice conditions in the northwest Atlantic (Baffin Bay, Labrador Sea) and in far Eastern seas (Bering Sea) exhibit the largest seasonal changes in the sea ice area (*Mironov et al.*, 2007). These regions are nearly 100% ice-free during summer time. From Fig. 7.12, it can be seen that the freeboards in those regions

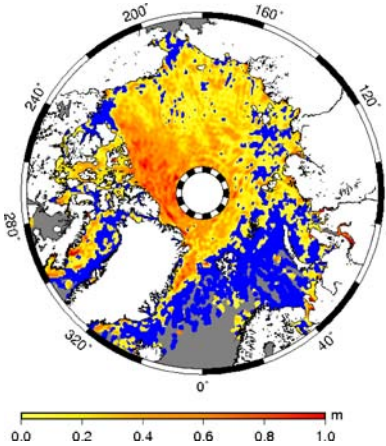

Figure 7.8: Sea ice freeboard maps – May–June 2005

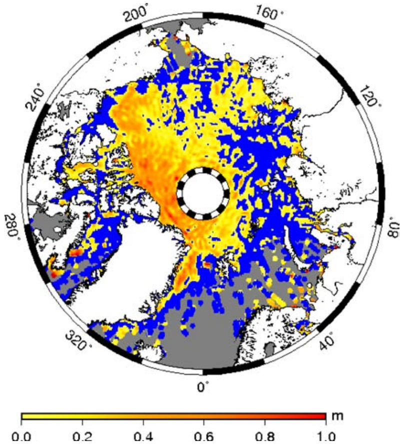

Figure 7.9: October–November 2005

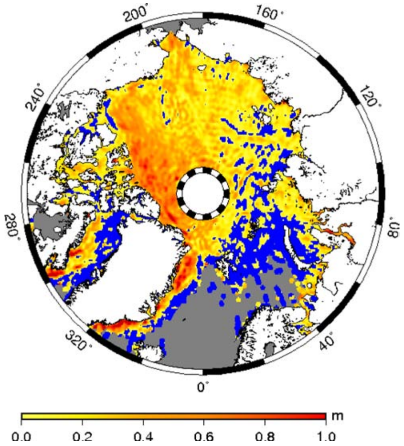

Figure 7.10: February–March 2006

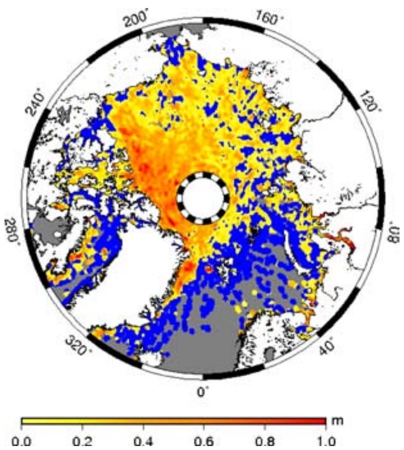

Figure 7.11: May–June 2006

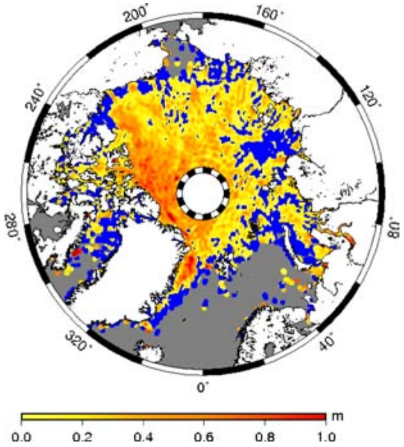

Figure 7.12: October–November 2006

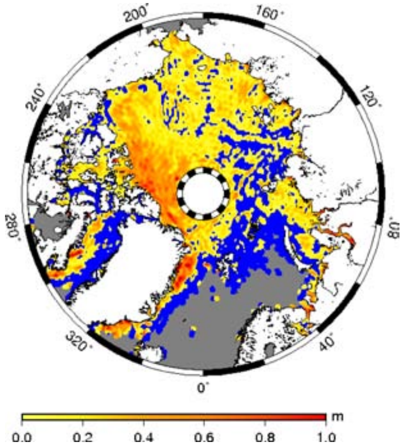

Figure 7.13: March–April 2007

are zero during the month of October a few days after the summer minimum. And thicker freeboards ($\sim 20 - 40$ cm) can be seen in those regions during the month of February, when the ice cover approaches its seasonal maximum in March–April.

5. The ice conditions in the Nordic Seas (Barents, Greenland, and Norwegian seas) show 65% seasonal changes in the ice area (*Mironov et al.*, 2007). Figs. 7.8 - 7.13 show that there is only limited data available around these regions. Hence, the seasonal changes in these regions cannot be studied in more detail.

6. *Mironov et al.* (2007) report that in the marginal Arctic seas (Kara, Laptev, East Siberian, Chukchi, and Beaufort Seas) the ice conditions decrease by about $20 - 30\%$ from March to September. Fig. 7.9 and 7.10 show that the ice cover has grown to its full extent in these regions during February–March (~ 20 cm freeboard, equivalent to $1.2 - 1.6$ m thickness) when compared to the conditions in October–November.

7. The ice conditions in the Arctic basin are more stable, exhibiting less ($< 20\%$) changes in the ice cover between Winter and Summer (*Mironov et al.*, 2007) which can also be seen in the results from this study.

8. Fig. 7.6 and 7.7 show that the ice drift velocity increases from Summer to Winter in the regions nearing the Fram Strait, and the Beaufort Gyre area decreases from Winter to Summer. These processes also cause seasonal variations in the sea ice cover.

9. The seasonal variations in the total freeboard also includes the variations in the snow accumulation. Fig. 4 in *Kwok and Cunningham* (2008) shows that

the snow accumulation between October–November 2005 and February–March 2006 is $\sim$ 15 cm over both multi-year ice and first-year ice zones.

Interannual variations

The causes of interannual variations in the Arctic sea ice cover are changes in the intensity of solar radiation that is absorbed by the ice, the ice age composition and the thickness of the ice formed during the freezing season (*Mironov et al.*, 2007).

1. Figs. 7.9 and 7.12 show the sea ice extent in the Arctic Ocean after the seasonal minimum in September. The second lowest minimum sea ice extent, since the satellite observation began in 1979, was observed in September 2005. Hence, Fig. 7.9 shows a lower sea ice extent when compared to October 2006. Most of the recovered sea ice cover is expected to be younger ice (first-year or second-year) rather than multi-year ice (see Fig. 2.1 in Chapter 2).

2. The interannual variations are also due to differences in the exact dates of freeze-up and melt onset. Since, ICESat only measures $\sim$ 33 days, three times a year and not always at the same 33 day time interval, the inter-annual variation signal is sampled irregularly. Hence, conclusions cannot be drawn about inter-annual variations with only 4-5 years of data.

3. *Mironov et al.* (2007) analyzed the contributions of the variability of sea ice cover in the marginal seas towards the variability of sea ice cover in the Arctic Ocean at different seasons. They found that the contribution from the Nordic seas is the largest during winter and the contribution from the Siberian shelf is largest during summer.

4. The sea ice circulation and advection causes interannual variability. The sea ice cover is constantly advected in the Arctic Ocean due to the Beaufort Gyre and the Transpolar Drift. The sea ice produced in the Russian Arctic joins the Transpolar Drift and ends up in the Greenland Seas. The sea ice is exported into the Greenland Seas from the Kara Sea in 1–2 years, Laptev Sea in 2–3 years, East Siberian Sea in 3–4 years, and Chukchi Sea in 4–5 years. The sea ice in the north of Greenland and Canada takes up to 7–8 years to reach the Fram Strait and Greenland seas. Hence, the ice parcel that was seen in the first year at a given location is not the same ice parcel seen in the following year due to sea ice circulation in the Arctic Ocean. This also leads to interannual variability.

5. The inter-annual trend in the freeboard is not studied in this work because of the uncertainties in the estimated freeboard. The accuracy of the freeboard results must improve before such analyses can be made.

7.1.4 Comparison of freeboard with the 'lowest level method'

Figs. 7.14 and 7.15 show the sea ice freeboards derived using geodetic models (used in this study) and the 'lowest level method' (implemented by Henriette Skourup at the Technical University, Denmark). The differences between the two methods are the (i) geoid model – ArcGP in 'lowest levels', EIGEN-GL04c in this study, (ii) MDT model – observed in 'lowest levels' by using the lowest elevation within a 25-km area, UW model in this study. These are the only main differences between the two methods. The comparison shows that the overall sea ice freeboard distributions from the two methods are in good agreement. From regional comparisons, it can be seen that

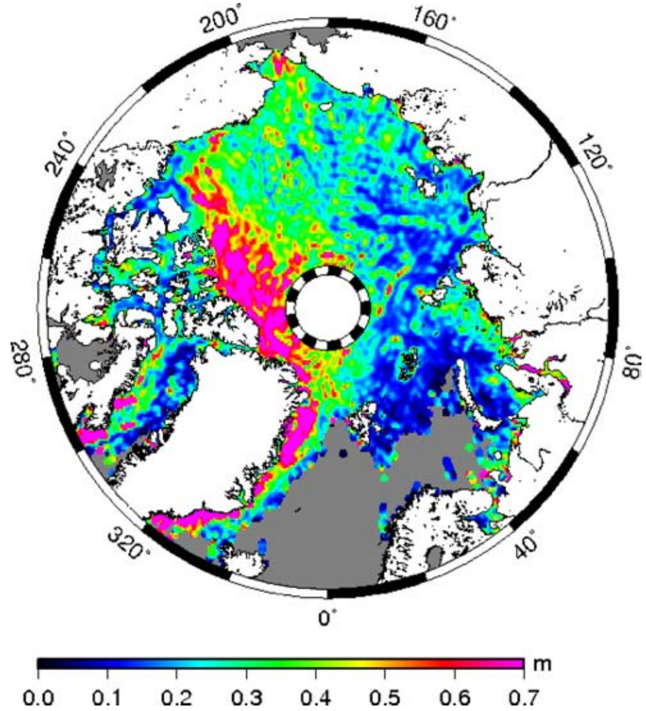

Figure 7.14: Arctic sea ice freeboards during the February 2006 ICESat epoch, computed from geodetic and oceanographic models

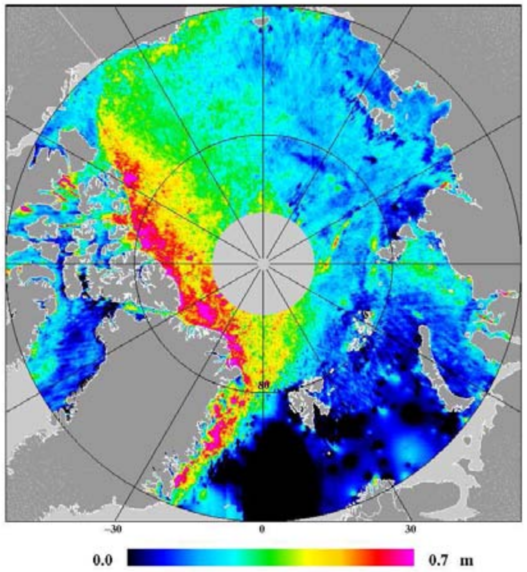

Figure 7.15: Arctic sea ice freeboards during the February 2006 ICESat epoch, computed using the 'lowest level' method by Henriette Skourup, Technical University, Denmark.

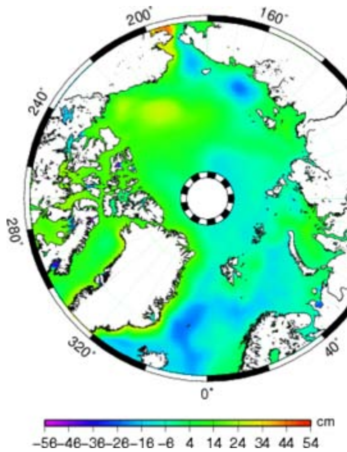

Figure 7.16: MDT – October 2004

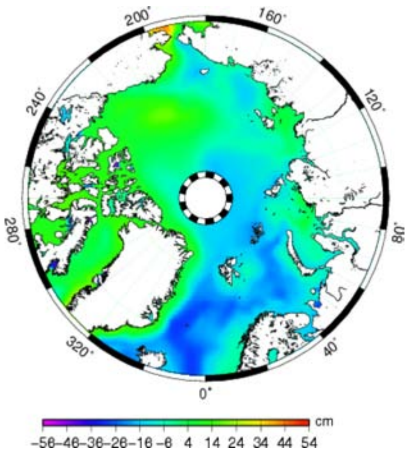

Figure 7.17: February 2005

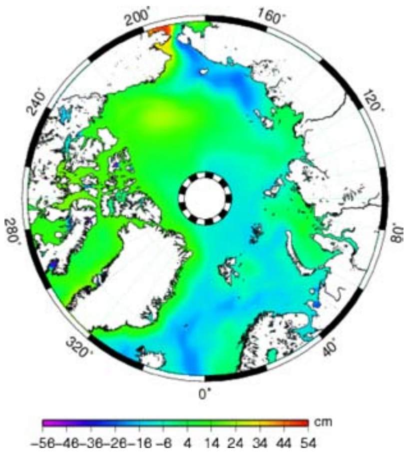

Figure 7.18: May 2005

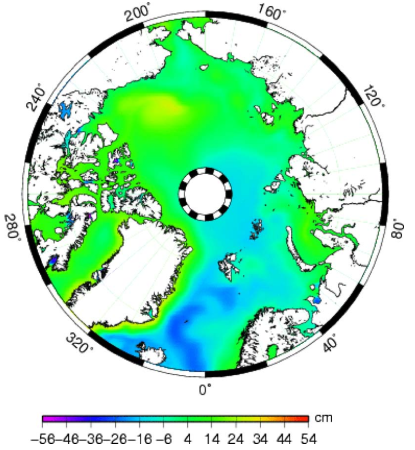

Figure 7.19: October 2005

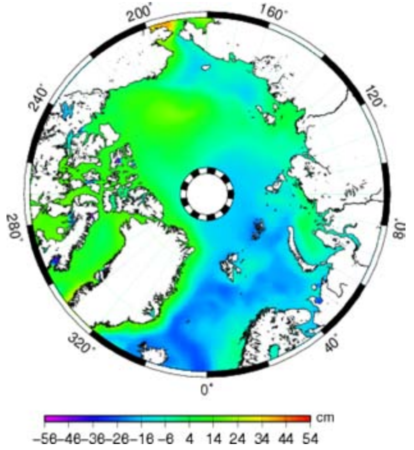

Figure 7.20: February 2006

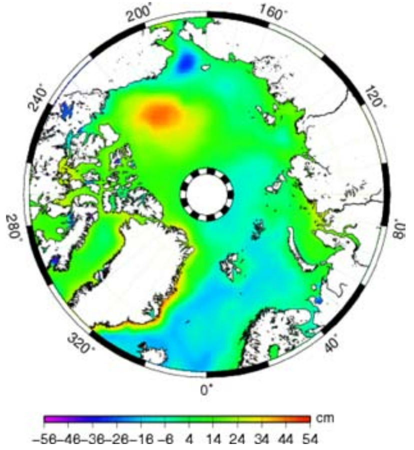

Figure 7.21: March 2007

similar features are detected in both methods, namely:

- Thicker ice export in the Fram Strait, eastern parts of Greenland.
- Thicker multi-year ice north of Greenland and Ellesmere islands (in the Canadian archipelago).
- Land-fast and thinner sea ice in the Barents and Kara seas.
- Ice free conditions in the southern regions of Svalbard and northern parts of the Barents sea.
- Flaw polynyas between the fast-ice covered regions of the Russian Arctic and the drifting ice in the Central Arctic (section 7.1.3).

The sources of error in the 'lowest level' method is due to the assumption that the lowest elevation within a 25-km area are open water regions. In this study, the major possible source of error is the mean dynamic topography model. Fig. 7.16–7.21 show the MDT signal during different ICESat mission phases. In the ArcGICE study (*Forsberg et al.* (2007)), it was found that there are large differences in the MDT signal predicted by different MDT models. However, the UW model used in this study had the best agreement with the MDT signal derived from altimetry data (see Figure 6 in *Skourup and Forsberg* (2008)). Therefore, the UW model has sufficient accuracy for the sea ice freeboard estimation. In summary, the Arctic sea ice freeboards estimated from geodetic models show good agreement with the 'lowest level' method (*overall and regional*).

7.1.5 Sensitivity analysis

A sensitivity analysis must be carried out in order to determine the uncertainty in the estimated sea ice freeboards from ICESat. Using Eqn 4.3 and assuming that the variables are uncorrelated, the sensitivity equation of the total freeboard (sea ice freeboard plus snow depth) is –

$$\sigma^2_{h_f} = \sigma^2_{h_e} + \sigma^2_{h_n} + \sigma^2_{h_t} + \sigma^2_{h_{mdt}} + \sigma^2_{h_{ibe}} \tag{7.1}$$

where, σ_{h_f}, σ_{h_e}, σ_{h_n}, σ_{h_t}, $\sigma_{h_{mdt}}$, and $\sigma_{h_{ibe}}$ are the uncertainties in the total freeboard, ellipsoidal heights, geoid undulations, ocean tides, mean dynamic topography, and inverse barometric effect correction. The expected uncertainties in each of the quantities are (i) h_e – 5 cm. *Zwally et al.* (2002) estimated an uncertainty of $\sim$ 14 cm within a GLAS 70 m footprint area. However, the GLAS accuracy improves over larger spatial scales. Hence, an uncertainty of 5 cm over 100 km was assumed. (ii) h_n – 15 cm. *Foerste et al.* (2008) reported an uncertainty of 15 cm over the full-resolution (110 km) of the geoid model, EIGEN-GL04c. (iii) h_t – 10 cm. This value was taken from the accuracy assessment carried out in this study (Chapter 5). (iv) h_{mdt} – 15 cm. The UW model agrees with the MDT derived from altimetry data (*Forsberg et al.* (2007)). Therefore, the error was assumed as 15 cm (which is half of the range variability in the MDT signal in the Arctic Ocean). (v) h_{ibe} – 5 cm. There are no formal error estimates provided for the atmospheric fields produced by the NCEP Global Data Assimilation System (GDAS), especially in the Arctic Ocean. *Herring and Quinn* (2001) report that some studies have compared the NCEP GDAS with the European Center for Medium-Range Weather Forecasting (ECMWF) analyses, however both of these analyses have used similar input data and physical models and, hence, cannot provide a quantitative error estimate. Therefore, an uncertainty of 5 cm was assumed in the Arctic Ocean. This is comparable to the sea level pressure variability of $\sim 15 mbar$ and the corresponding IBE correction of $\sim$ 15 cm (section 4.4.5). The uncertainty of 5 cm represents one-third of the variability of the sea level pressure signal.

Using the assumed uncertainties in Eqn. 7.1, an uncertainty of $\sim$ 24 cm in the total freeboard in the Arctic Ocean (at approximately 100 km length scale) was found. The freeboard distribution at regional scales (longer than 100 km) are, therefore, expected to have better accuracy.

7.1.6 Arctic sea ice freeboard distribution

It is important to compute the probability density function (PDF) of the sea ice freeboard distribution, denoted as *g(h)*, besides the *mean* of the freeboard distribution. The *g(h)* is significant for a number of reasons –

1. The shape of the *g(h)* is a measure of the extent of sea ice deformation.
2. It controls the surface heat budget. Especially, the thin ice distribution dominates the heat exchange between the ocean and atmosphere.
3. *g(h)* can be combined with the ice velocity (derived from active or passive microwave sensors) to measure the mass flux.
4. The thin ice distribution (seasonal ice cover) can also be used to estimate the melt rate or the fresh water flux.
5. By combining the *g(h)* with multi-year ice or first-year ice fraction, the ice strength and other mechanical properties of different ice types can be estimated.

6. The long term trend in *g(h)* also indicates the response of the ice cover to climate variability (*Wadhams and Amanatidis*, 2005).

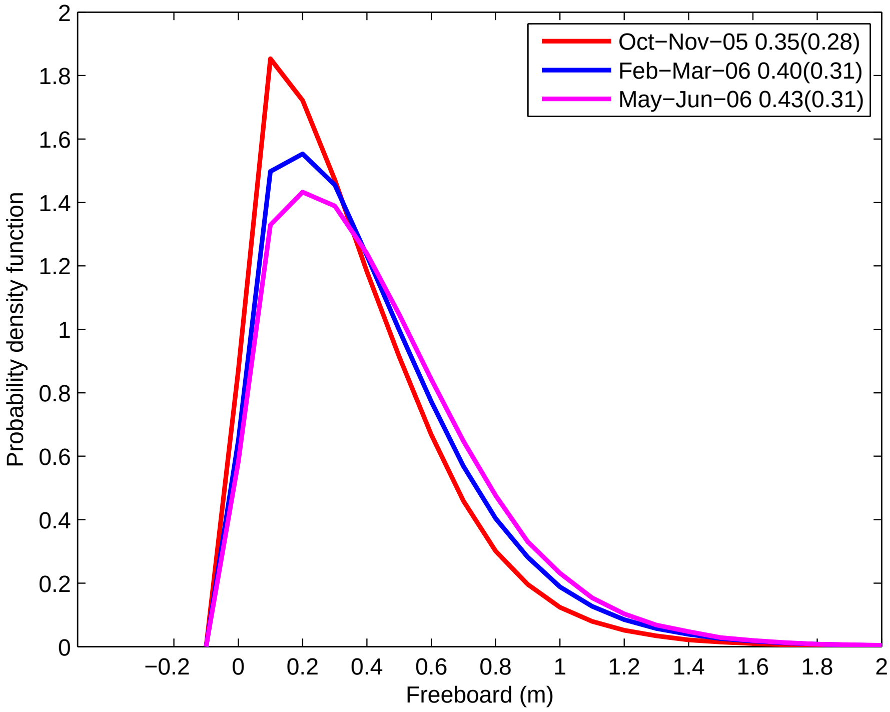

Figure 7.22: Sea ice freeboard distribution during ICESat Oct–Nov 2005, Feb–Mar 2006, May–Jun 2006 epochs.

Discussion

Fig. 7.22 shows the probability density function (PDF) of the sea ice freeboards from three ICESat mission phases – October–November 2005, February–March 2006, May–June 2006. A narrow and steep slope can be seen near freeboards < 30 cm. A wider and shallow slope can be seen near freeboards > 40 cm. This indicates that the ridged multi-year ice (MYI), represented by the thicker ice freeboard (> 40 cm), is rougher and highly deformed. A wider tail is seen due to variations in the extent of deformation depending on the age of MYI.

7.2 Sea ice growth during the freeze-up season

A first order estimate of the total freeboard (sea ice freeboard + snow depth) in the Arctic Ocean was derived using the GLAS data from the October-November 2003 ICESat epoch by applying only the geoid (dominant signal in the sea surface height) and ocean tides corrections (see Chapter 4, section 4.4). This analysis was carried out to study the sea ice growth during the freeze-up period. The GLAS data release 26 were used in this process which was the most recent release available at the time of this part of the study. The saturation corrections were poorer for release 26 when compared to release 28 data (NSIDC). However, the first order estimates indicate reasonable sea ice freeboard distribution in the Arctic.

GLAS data from 10 days of ICESat flight were used to derive the sea ice freeboard for one time-period. The 10-day window was moved forward by 5-days to derive a time-series of sea ice freeboard maps. Data from October 09 – November 08, 2003 were used to derive the time-series. The freeboard results were plotted on a 10' × 5' grids. Figs. 7.23–7.28 show a the thermodynamic ice growth in the Arctic Ocean during the freeze-up period (October). The rate of the ice growth is inversely proportional to the thickness of the ice. Therefore, fast ice growth can be noticed in the seasonal ice zone. The multi-year ice fraction (above Greenland and eastern Canada) also grows thicker and first-year ice is formed in the Beaufort gyre, Barents sea and Russian Arctic.

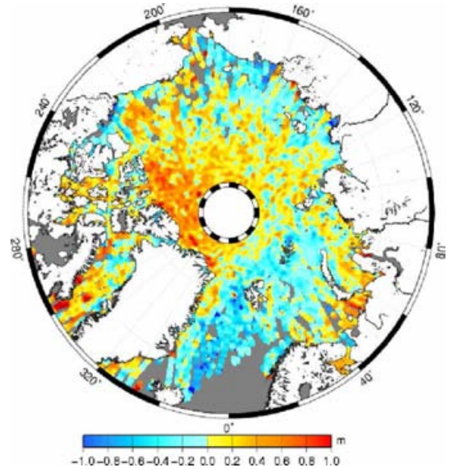

Figure 7.23: Sea ice freeboards October 9–18 2003

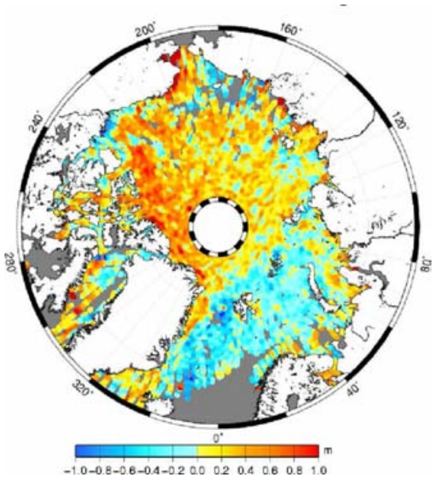

Figure 7.24: October 14–23 2003

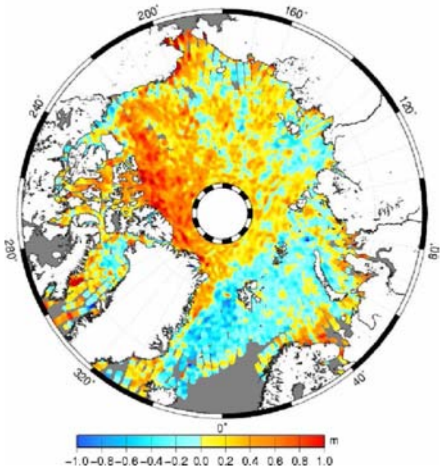

Figure 7.25: October 19–28 2003

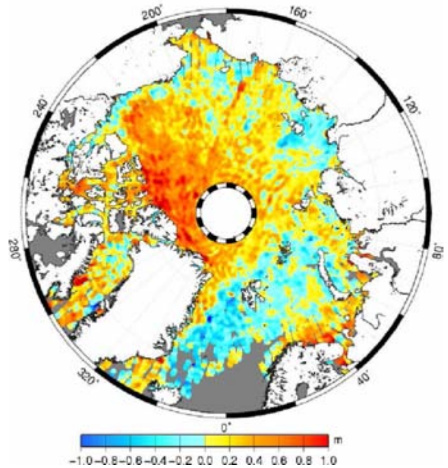

Figure 7.26: October 24–November 02 2003

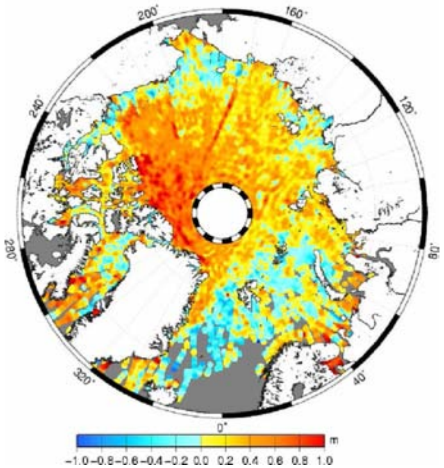

Figure 7.27: October 29–November 08 2003

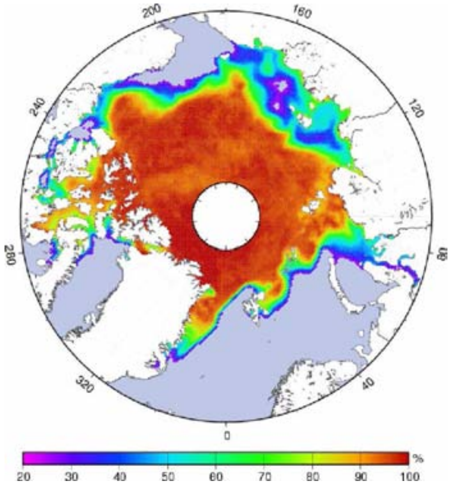

Figure 7.28: Sea ice concentration from SSM/I

The derived freeboard maps were compared with the sea ice concentration during October, 2003 obtained from the SSM/I sensor. The freeboard results show good agreement with the sea ice concentration. The regions of low or zero sea ice concentration matches with the regions of low or zero freeboard.

7.3 Sea ice thickness computation from sea ice freeboards

The total thickness (sea ice thickness + snow depth) measured using the Helicopter-borne Electromagnetic Induction (HEM) technique were obtained from *Haas et al.* (2006) for comparison with this study. The HEM data were collected on May 14, 2006 over a $\sim$ 380 km track. In order to compare the total freeboard computed in the study with the HEM total ice thickness, the total freeboard around the HEM track (Fig. 7.29) was converted into total ice thickness. The steps involved in this procedure are (i) converting the total ice freeboard into sea ice thickness, (ii) converting the sea ice thickness into total ice thickness (adding the snow depth).

Arctic sea ice freeboard can be converted into sea ice thickness by assuming hydrostatic equilibrium conditions. The physical properties of the ice layer and the overlying snow layer such as snow depth, snow density, sea water density and sea ice bulk density must be known in order to convert the freeboard into thickness (Eqn. 4.9). In this study, these physical properties were assumed as a constant, although the absolute value depends on their thermodynamic growth stage and physical constituents (*e.g.*, brine volume).

Seawater density The density of seawater is a function of temperature, salinity and pressure. In this study, the density of the surface seawater can be assumed as a constant, $1024 kg/m^3$ with an uncertainty of $\sim 1 kg/m^3$. It is valid to assume

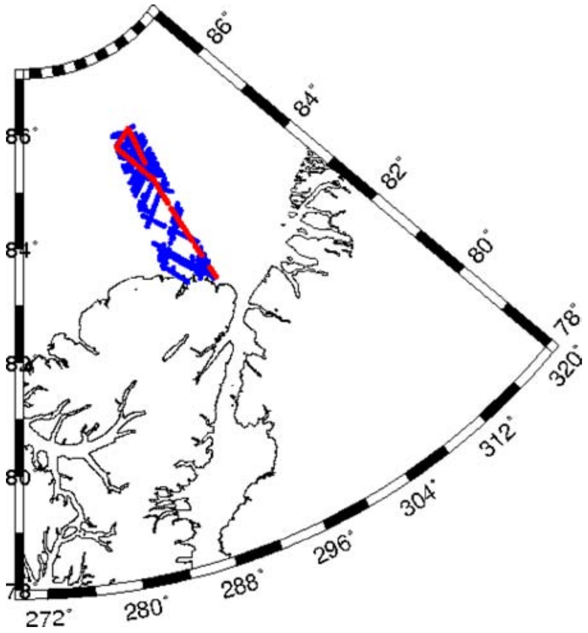

Figure 7.29: Tracks of Helicopter-borne EMI measurements (red) and ICESat freeboard measurements (blue) in the region north of Ellesmere island and Greenland.

a constant value, because the uncertainty in the thickness estimation due to the uncertainty in seawater density is insignificant (section 7.3.2). As a comparison, *Laxon et al.* (2003) used a constant value of $1023.9 kg/m^3$ with an uncertainty of $0.5 kg/m^3$ as the seawater density.

Sea ice bulk density The composition of the sea ice layer includes solid ice, solid salts and liquid brine and air pockets. Because, the distribution of these components vary within the ice layer and between ice floes, the sea ice density also varies spatially and temporally. Since 1927, a number of studies have reported the sea ice density measured using different techniques. *Timco and Frederking* (1996) presented a summary of the reported values. The sea ice density varied over a wide range of values – $720 kg/m^3$ to $940 kg/m^3$. In general, the measured density ranges from $840 kg/m^3$ to $910 kg/m^3$ for the first-year sea ice above the waterline, $720 kg/m^3$ to $910 kg/m^3$ for the multi-year sea ice layer above the waterline, and $900 kg/m^3$ to $940 kg/m^3$ for all ice types below the waterline. *Laxon et al.* (2003) used $915.1 kg/m^3$ as the constant value for ice density. In this study, the sea ice bulk density (*i.e.*, depth integrated) was assumed to be $920 kg/m^3$ with an uncertainty of $10 kg/m^3$, similar to *Kwok and Cunningham* (2008).

Snow depth *Kwok and Cunningham* (2008) estimated the snow depth distribution in the Arctic Ocean (section 4.4.6). In this study, a constant snow depth of 50 cm (with an uncertainty of 5 cm) was assumed along the HEM track ($\sim$ 380 km) in the MYI region north of Greenland and Ellesmere island. This value is based on the average snow depth in the northern parts of Ellesmere Island (Figure 4 in *Kwok and Cunningham* (2008)).

Snow density *Warren et al.* (1999) reported that the snow density exhibits seasonal variations, but very little geographic variation on the sea ice. Their results indicate that the temporal variations range from $\sim 250 kg/m^3$ in September to $320 kg/m^3$ in June, and the rate of increase in snow density is higher from September to December than from January to June. *Kwok and Cunningham* (2008) used the similar values as *Warren et al.* (1999) with some modifications – a lower snow density ($\sim 200 kg/m^3$ instead of $250 kg/m^3$) was used for the fall season from September to December. It is challenging to estimate the time-dependent snow bulk density (*i.e.*, density integrated over the snow depth/layer) for the entire Arctic basin. Various processes such as snow storms (add more fresh snow that has a lower density) constantly modify the snow layer and the density distribution within the snow layer. Therefore, there are significant uncertainties in the assumed snow density values. *Warren et al.* (1999) reported a $100 kg/m^3$ uncertainty in their snow density climatology. In this study,

Table 7.2: A summary of the assumed values for the physical properties of sea ice and snow depth

Parameter	Assumed constant	Uncertainty
Snow depth	50 cm	5 cm
Snow density	320 kg/m^3	100 kg/m^3
Sea ice density	920 kg/m^3	10 kg/m^3
Seawater density	1024 kg/m^3	1 kg/m^3

the snow density was assumed to be a constant, $320 kg/m^3$ in May (based on *Warren et al.* (1999) and *Kwok and Cunningham* (2008)).

Table 7.2 summarizes the snow density, snow depth, sea ice bulk density and sea water density values that were assumed in this study and the uncertainties in each of those parameters. A sensitivity analysis must be performed in order to assess the uncertainty in the ice thickness estimation process. The sources of uncertainty in the thickness estimates are the errors in the freeboard estimation, and assumptions made about the physical properties of the sea ice and snow layer.

7.3.1 Comparison of total ice thickness from HEM measurements and ICESat

The sea ice thickness was calculated along the HEM track using the sea ice freeboard heights from the ICESat May 2006 epoch. The objective of this comparison is (i) to demonstrate the potential of deriving sea ice thickness estimates from ICESat, and (ii) to perform a *regional* validation of the sea ice thickness distributions.

Fig. 7.30 shows the sea ice thickness distribution in the region (Fig. 7.29) north of Greenland and Ellesmere Island. It can be seen that the HEM-based total ice thickness distribution is relatively narrow, when compared to the ICESat-based thickness

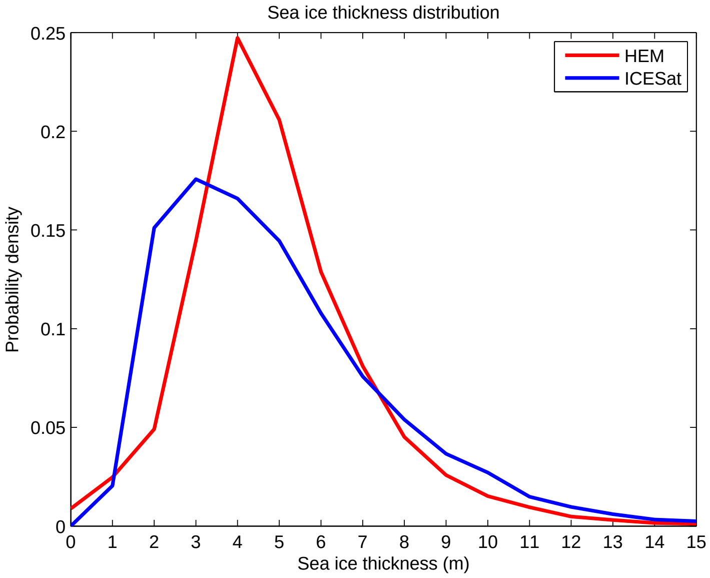

Figure 7.30: Probability density function of the total ice thickness (sea ice + snow depth) distribution derived from ICESat (blue) and HEM (red).

distribution. This is because more ICESat points were available to derive the thickness distribution in the study area (Fig. 7.29). Hence, more number of ice thickness classes were sampled by ICESat. The mean, median and standard deviation of the HEM-based total thickness distribution were 4.94 m, 4.60 m and 2.24 m respectively. The mean, median and standard deviation of the ICESat-based total thickness distribution were 5.47 m, 4.91 m and 2.66 m, respectively. This indicates that the thickness distributions derived from the two techniques agree within 0.53 m. These differences are within the accuracy of the two techniques. It can also be seen that the ICESat-based thickness distribution has a slightly higher frequency over the thicker ice classes, which might have increased the mean when compared to the HEM distribution. Since, more ICESat points were available in the study area, the standard deviation is higher, confirming that a wider range of thickness classes were sampled by ICESat.

7.3.2 Sensitivity analysis

A sensitivity analysis must be carried out in order to examine the uncertainty in the estimated sea ice thickness. Using Eqn 4.9 and assuming that the physical properties are uncorrelated, the sensitivity equation of the sea ice thickness is

$$\sigma_{h_i}^2 = \sigma_{h_{tf}}^2 \left(\frac{\partial h_i}{\partial h_{tf}}\right)^2 + \sigma_{h_s}^2 \left(\frac{\partial h_i}{\partial h_s}\right)^2 + \sigma_{\rho_s}^2 \left(\frac{\partial h_i}{\partial \rho_s}\right)^2 + \sigma_{\rho_i}^2 \left(\frac{\partial h_i}{\partial \rho_i}\right)^2 + \sigma_{\rho_w}^2 \left(\frac{\partial h_i}{\partial \rho_w}\right)^2 \quad (7.2)$$

where,

$$\frac{\partial h_i}{\partial h_{tf}} = \frac{\rho_w}{\rho_w - \rho_i},$$
$$\frac{\partial h_i}{\partial h_s} = \frac{\rho_w - \rho_s}{\rho_w - \rho_i},$$
$$\frac{\partial h_i}{\partial \rho_s} = \frac{h_s}{\rho_w - \rho_i},$$
$$\frac{\partial h_i}{\partial \rho_i} = \frac{\rho_w h_{tf} - (\rho_w - \rho_s)h_s}{(\rho_w - \rho_i)^2},$$
$$\frac{\partial h_i}{\partial \rho_w} = \frac{-\rho_i h_{tf} + (\rho_i - \rho_s)h_s}{(\rho_w - \rho_i)^2},$$

where, h_i is the sea ice thickness, h_s is snow depth, h_{tf} is total freeboard, ρ_w is seawater density, ρ_s is snow density, and ρ_i is sea ice density. The uncertainties in the physical properties are assumed as, (i) $\sigma_{h_{tf}} = 5$ cm. This value is the relative difference in the overall mean taken from the comparison with *Kwok and Cunningham* (2008) study; (ii) $\sigma_{h_s} = 0.05$ m; (iii) $\sigma_{\rho_s} = 100 kg/m^3$; (iv) $\sigma_{\rho_w} = 1 kg/m^3$; (v) $\sigma_{\rho_i} = 10 kg/m^3$ (Table 7.2). The nominal values used in the sensitivity calculations are (i) $h_{tf} = 1.0$ m; (ii) $h_s = 0.5$ m; (iii) $\rho_s = 320 kg/m^3$; (iv) $\rho_w = 1024 kg/m^3$; (v) $\rho_i = 920 kg/m^3$.

The uncertainty in the computed sea ice thickness, σ_{h_i}, in the MYI region north of Ellesmere island and Greenland, is estimated as 0.98 m. This is comparable to the

Table 7.3: Sensitivity analysis of the thickness estimates

x	σ_x	$\frac{\partial h_i}{\partial h_x}$	$\sigma_x \left(\frac{\partial h_i}{\partial h_x}\right)$
h_{tf} m	0.05	9.85	0.49
h_s m	0.05	-6.77	-0.33
$\rho_s(kg/m^3)$	100	0.0048	0.48
$\rho_i(kg/m^3)$	10	0.0621	0.62
$\rho_w(kg/m^3)$	1	-0.0573	-0.057

$\sim$ 0.75 m uncertainty estimated by *Kwok and Cunningham* (2008) over the perennial ice cover. A larger uncertainty was found in this study, because the uncertainties vary with the relative thickness and snow depth values (a larger nominal value was used in this study, because the study area represents the thickest ice cover region in the Arctic Ocean). Over seasonal ice zones with thinner freeboard and snow depth, the thickness estimates are expected to have lower uncertainties. For example, using different nominal values that represent the FYI region in Winter (h_{tf} = 30 cm, h_{ts} = 20 cm), the estimated uncertainty decreases to 0.646 m.

7.4 Summary

- ICESat data provides dense coverage at the high-latitude regions that can be exploited to study the temporal evolution of the sea ice cover. Such an analysis was carried out in this thesis. Using 10 days of ICESat release 26 data, a first-order estimate of the time-series of total freeboard heights in the Arctic Ocean was derived. The sea ice begins to form in the seasonal ice cover regions and continues to grow in thickness and area. Similar analysis could be carried out with the upcoming releases that contain improved saturation corrections.
- The sea ice freeboard maps obtained from release-28 data show good agreement

with QuikSCAT backscatter fields. The freeboard distributions in October 2005 and February 2006 were compared with the findings from other studies. The freeboard estimation using the geodetic and oceanographic models agrees well with the other methods.

- The error budget was computed from the sensitivity analysis for the freeboard estimation procedure used in this study. The sensitivity analysis shows that the uncertainty in the freeboard estimation is on the order of $\sim 24cm$ and the MDT is the major source of error in the freeboard estimation. In this thesis, the MDT model which was consistent with the MDT derived from satellite altimetry was used. It is expected that the MDT models will continue to improve in the future with the launch of the GOCE satellite and the assimilation of altimetry-derived MDT signals. Although an uncertainty of 24 cm was found over a 100 km length scale, the overall mean of the freeboard distribution in October 2005 and February 2006 agree within 5 cm with the *Kwok and Cunningham* (2008) study. This implies that both methods resulted in a similar sea ice distribution and the inherent uncertainties in both methods are on the same scale. In conclusion, both methods are able to provide sea ice distribution in the Arctic, and the current limitations in the method described here are due to the component models, which will continue to improve in the future.

- The sea ice freeboard maps show reasonable regional and seasonal distribution that are consistent with the reported values in the literature. The probability density distribution of the sea ice freeboard heights were also derived in order to study the physical characteristics of the sea ice cover. The non-Gaussian shape of the PDF (with wide shallow tail) indicates that the MYI cover is highly deformed with higher number of thicker ice classes. The relatively narrow thin ice classes indicate that the FYI cover nearly attains the same thickness (uniform growth rate) with little deformation. A time-series of the PDF distribution can be used to study the change in mechanical properties of the ice cover.

- It was demonstrated that the sea ice thickness can also be estimated from the sea ice freeboard heights. The sensitivity analysis indicates that the accuracy of this procedure is 0.98 cm (comparable to the reported values in the literature). The sea ice thickness estimates derived in this study show good agreement (within 0.53 cm) with independent measurements (HEM).

Chapter 8

Conclusions and Outlook

8.1 Conclusions

The list of contributions and conclusions from this research work are presented by addressing the research objectives stated in section 1.2.

- *The sea ice freeboard heights in the Arctic Ocean were derived from ICESat sea ice altimetry data products using a* new *method.* Regional and seasonal analyses of the sea ice freeboard distribution were also carried out which indicated that the freeboard heights estimated in this study are consistent with the regional/seasonal values reported in the literature.

- *The present generation of geoid, ocean tides and mean dynamic topography models were used to estimate the instantaneous sea surface heights at basin-wide in the Arctic Ocean.* The MDT signal is likely the major source of error in the sea surface height (and freeboard) estimation because there are differences in the MDT signal predicted by different MDT models. Nevertheless, the MDT models are expected to improve in the future, with the launch of the GOCE satellite and the assimilation of ice-altimetry based MDT signals.

- The advantages of using the method described in this study to derive freeboard heights are that (i) it does not depend on other data sets such as RADARSAT to identify the open water regions and (ii) it does not depend on the availability of open water regions within every 25 km × 25 km area. Sea ice freeboard heights can be derived at more ICESat footprint locations when compared to other methods that depend on ‘observing’ the instantaneous sea surface heights.

- *The uncertainty of the sea ice freeboard retrieval process was estimated as* $\sim 24cm$. However, a regional accuracy assessment of the existing MDT models must be carried out, in order to determine a more representative error budget for the freeboard estimates.

- *The accuracy assessment of the existing global and regional ocean tide models that was carried out in this study indicates that the best ocean tide model for the Arctic Ocean is the AOTIM-5 model.* Therefore, the tide model correction from the GOT ‘00 model must be replaced by the AOTIM-5 model, because the two models show $>$ 20 cm differences in some parts of the Arctic Ocean which will affect the freeboard estimation.

- *The sea ice freeboard maps show good comparison with the ‘lowest level’ method.* Although this is not an entirely independent comparison (both maps were derived from ICESat), the good comparison between the two freeboard maps indicates that the existing geoid/ocean tides/MDT models, in general, have a reasonable accuracy in the Arctic Ocean to enable the estimation of freeboard height at accuracies comparable to the observational techniques, e.g. lowest level.

- *It was demonstrated that the sea ice thickness can also be derived from ICESat at regional scales with an accuracy of* $\sim$ *98 cm over complicated MYI zones.* The accuracy is, however, expected to improve over seasonal ice zones.

- *The preliminary field experiments carried out in Churchill, Manitoba, indicate* *that Churchill is a suitable site for validating ICESat elevations because it provides a variety of surface types in one location.* The field campaigns are also inexpensive compared to Arctic expeditions. With a limited number of GPS RTK and ICESat elevations for comparison, it was found that the measurements agree within < 10 cm. This indicates that ICESat data have sufficient accuracy to provide sea ice freeboard heights.

8.2 Outlook

An outlook into the future of sea ice freeboard retrieval from ICESat is provided.

- The accuracies of the geoid and mean dynamic topography models are expected to improve with the launch of the GOCE satellite. The main objective of GOCE is to determine the geoid with an accuracy of 1–2 cm at better than 100 km spatial resolution and to determine the mean ocean circulation (*Drinkwater et al.*, 2007). The ocean tide models are also expected to improve in the future with the availability of ice-altimetry data from ICESat since 2003 (and, in the future, possibly Cryosat-2 and ICESat-2) for assimilation into these models. The improvements in the accuracy of models will also improve the accuracy of the freeboard heights. Altimetry data are currently assimilated in many models and also used in the sea ice freeboard estimation. Rather than estimating one parameter with high accuracy, altimetry data can provide an optimal estimate of all of the geophysical parameters.
- An optimal estimate of the instantaneous sea surface height can be achieved by combining the different methods of sea surface height estimation. The in-

stantaneous local sea level can be observed when ICESat passes through open water regions and leads. These measurements can be used to constrain the instantaneous sea surface heights modeled in this study. In this manner, a better accuracy can be achieved in all regions. When there are no leads present in the region (25 km × 25 km), the oceanographic models can provide an estimate of the sea surface height and, when the leads are present in the region, the observations will constrain the modeled sea surface heights.

- The method of sea ice freeboard retrieval used in this study can be used to derive freeboard heights from the upcoming Cryosat-2 and ICESat-2 missions. A continuous temporal coverage of the Arctic Ocean may be achieved with the upcoming missions when compared to ICESat that provides coverage of up to four months every year only.
- The accuracy of sea ice thickness estimates can be improved by using regional *in-situ* sea ice and snow bulk density profiles. A number of field campaigns were carried out by the research community in different parts of the Arctic Ocean. Access to these data sets will greatly reduce the uncertainty in the thickness estimates at regional scales. A more comprehensive accuracy assessment of the estimated freeboard heights can be achieved when such independent data sets are available for validation.
- The interannual trend in the sea ice thickness (and volume) can be derived in the future, as the accuracy of the sea ice freeboard and thickness will continue to improve (*e.g.*, *Kwok et al.* (2009) and *Kurtz et al.* (2009)).

Bibliography

Abshire, J. B., X. Sun, H. Riris, J. M. Sirota, J. F. McGarry, S. Palm, D. Yi, and P. Liiva (2005), Geoscience Laser Altimeter System (GLAS) on the ICESat Mission: On-orbit measurement performance, *Geophys. Res. Lett.*, *32*, L21S02, doi:10.1029/2005GL024028.

Ackley, S. F., M. A. Lange, and P. Wadhams (1990), Snow cover effects on Antarctic sea ice thickness, in *Sea Ice Properties and Processes, CRREL Monogr. 90-1*, edited by S. F. Ackley and W. F. Weeks, pp. 16–21, U.S. Army Corps of Eng., Hanover, N. H.

Adolphs, U. (1999), Roughness variability of seaice and snowcover thickness profiles in the Ross, Amundsen, and Bellingshausen Seas, *J. Geophys. Res.*, *104*, 13,577–13,591.

Agnew, T., A. Lambe, and D. Long (2008), Estimating sea ice area flux across the Canadian Arctic Archipelago using enhanced AMSR-E, *J. Geophys. Res.*, *113*, C10011, doi:10.1029/2007JC004582.

Alexandrov, V. Y., T. Martin, J. Kolatschek, H. Eicken, M. Kreyscher, and A. P. Makshtas (2000), Sea ice circulation in the Laptev Sea and ice export to the Arctic Ocean: Results from satellite remote sensing and numerical modeling, *J. Geophys. Res.*, *105*(C7), 17,143–17,160, doi:10.1029/2000JC900029.

Alexandrov, V. Y., S. Sandven, O. M. Johannessen, and K. Kloster (2007), Interpretation of Sea Ice Parameters in SAR images, in *Remote Sensing of Sea Ice in the Northern Sea Route*, edited by O. M. Johannessen, V. Y. Alexandrov, I. Y. Frolov, S. Sandven, L. H. Pettersson, L. P. Bobylev, K. Kloster, V. G. Smirnov, Y. U. Mironov, and N. G. Babich, chap. 4.3, Springer-Praxis.

Andersen, O. B., and P. Knudsen (1997), Multi-satellite ocean tide modelling - the K1 constituent, *Progress in Oceanography*, *40*, 197–216.

Andersen, O. B., P. L. Woodworth, and R. A. Flather (1995), Intercomparison of recent ocean tide models, *J. Geophys. Res.*, *100*(C12), 25,261–25,282, doi:10.1029/95JC02642.

AVISO (2008), AVISO and PODAAC User Handbook - IGDR and GDR Jason Products.

Barber, D. G., A. Thomas, and T. N. Papakyriakou (1998), Role of SAR in surface energy flux measurements over sea ice, in *Analysis of SAR Data of the Polar Oceans: Recent Advances*, edited by C. Tsatsoulis and R. Kwok, pp. 35–67, Springer-Verlag, Berlin.

Barber, D. G., J. J. Yackel, and J. M. Hanesiak (2001), Sea ice, RADARSAT-1 and Arctic climate processes: A review and update., *Can. J. Remote Sens.*, *27(1)*, 51–60.

Beaven, S. G., G. L. Lockhart, S. P. Gogineni, and A. R. Hosseinmostafa (1995), Laboratory measurements of radar backscatter from bare and snow-covered saline ice sheets, *Int. J. Remote Sens.*, *16*(5), 851–876.

Bhang, K. J., F. W. Schwartz, and A. Braun (2007), Verification of the Vertical Error in C-Band SRTM DEM Using ICESat and Landsat-7, Otter Tail County, MN, *IEEE Trans. Geosci. Remote Sens.*, *45*, 36–44, doi:10.1109/TGRS.2006.885401.

Bindschadler, R., H. Choi, C. Shuman, and T. Markus (2005), Detecting and measuring new snow accumulation on ice sheets by satellite remote sensing, *Remote Sens. Environ.*, *98*, 388–402, doi:10.1016/j.rse.2005.07.014.

Bingham, R. J., and K. Haines (2006), Mean dynamic topography: intercomparisons and errors, *Phil. Trans. R. Soc. A*, *364*, 903–916, doi:10.1098/rsta.2006.1745.

Bitz, C., M. Holland, A. Weaver, and M. Eby (2001), Simulating the ice-thickness distribution in a coupled climate model, *J. Geophys. Res.*, *106*(C2), 2441–2463.

Bleck, R., C. Rooth, D. Hu, and L. T. Smith (1992), Salinity-driven Thermocline Transients in a Wind- and Thermohaline-forced Isopycnic Coordinate Model of the North Atlantic, *J. Phys. Oceanogr.*, *22*, 14861505.

Bogdanov, A. V., S. Sandven, O. M. Johannessen, V. Y. Alexandrov, L. P. Bobylev, and V. S. Loshchilov (2007), Sea ice retrieval algorithms for SAR, in *Remote Sensing of Sea Ice in the Northern Sea Route*, edited by O. M. Johannessen, V. Y. Alexandrov, I. Y. Frolov, S. Sandven, L. H. Pettersson, L. P. Bobylev, K. Kloster, V. G. Smirnov, Y. U. Mironov, and N. G. Babich, chap. 4.4, Springer-Praxis.

Bonnefond, P., P. Exertier, O. Laurain, Y. Meacutenard, A. Orsoni, G. Jan, and E. Jeansou (2003), Absolute Calibration of Jason-1 and TOPEX/Poseidon Altimeters in Corsica, *Mar. Geod.*, *26*, 261–284.

Braun, A., and G. Fotopoulos (2007), Assessment of SRTM, ICESat, and Survey Control Monument Elevations in Canada, *Photogramm. Engg. Rem. Sens.*, *73*(12), 1333–1342.

Brenner, A. C., H. J. Zwally, C. R. Bentley, B. M. Csath, D. J. Harding, M. A. Hofton, J.-B. Minster, L. Roberts, J. L. Saba, R. H. Thomas, and D. Yi (2003), Derivation of Range and Range Distributions From Laser Pulse Waveform Analysis for Surface Elevations, Roughness, Slope, and Vegetation Heights, Algorithm Theoretical Basis Document.

Brown, R. D., and P. Cote (1992), Interannual variability of landfast ice thickness in the Canadian High Arctic, 1950-89, *Arctic*, *45*(3), 273–284.

Carabajal, C. C., and D. J. Harding (2005), ICESat validation of SRTM C-band digital elevation models, *Geophys. Res. Lett.*, *32*, L22S01, doi:10.1029/2005GL023957.

Cavalieri, D., C. Parkinson, P. Gloersen, and H. J. Zwally (1996), updated 2008. Sea ice concentrations from Nimbus-7 SMMR and DMSP SSM/I passive microwave data. Boulder, Colorado USA: National Snow and Ice Data Center. Digital media.

Cavalieri, D. J., and C. L. Parkinson (2008), Antarctic sea ice variability and trends, 19792006, *J. Geophys. Res.*, *113*, C07004, doi:10.1029/2007JC004564.

Chang, A. T. C., and L. S. Chiu (1990), Global snow variation derived from SMMR: preliminary results, in *Sea Ice Properties and Processes, CRREL Monogr. 90-1*, edited by S. F. Ackley and W. F. Weeks, pp. 213–217, U.S. Army Corps of Eng., Hanover, N. H.

Chelton, D. B., J. C. Ries, B. J. Haines, L. Fu, and P. S. Callahan (2001), *Satellite Altimetry and Earth Sciences, A Handbook of Techniques and Applications*, vol. International Geophysics Seriess Volume 69, chap. 1 Satellite Altimetry, pp. 1–122, Academic Press.

CIS (2009), Canadian Ice Service, New Arctic Program and Ice thickness data archive, http://ice-glaces.ec.gc.ca/app/wsvpagedsp.cfm?id=11703, (accessed May 2009).

Comiso, J. (1990), updated quarterly. DMSP SSM/I Daily and Monthly Polar Gridded Bootstrap Sea Ice Concentrations, Edited by J. Maslanik and J. Stroeve. Boulder, Colorado USA: National Snow and Ice Data Center. Digital media., Boulder, CO: National Snow and Ice Data Center. Digital media.

Comiso, J. C. (2002), A rapidly declining perennial sea ice cover in the Arctic, *Geophys. Res. Lett.*, *29 (20)*, 1956, doi:10.1029/2002GL015650.

Comiso, J. C., and C. L. Parkinson (2008), Arctic sea ice parameters from AMSR-E data using two techniques and comparisons with sea ice from SSM/I, *J. Geophys. Res.*, *113*, doi:10.1029/2007JC004255.

Comiso, J. C., D. J. Cavalieri, and T. Markus (2003), Sea Ice Concentration, Ice Temperature, and Snow Depth Using AMSR-E Data, *IEEE Trans. Geosci. Remote Sens.*, *41*(2), 243–252.

Drinkwater, M. R., R. Haagmans, D. Muzi, A. Popescu, R. Floberghagen, M. Kern, and M. Fehringer (2007), The GOCE Gravity Mission: ESAS First Core Earth Explorer, in *Proceedings of the 3rd International GOCE User Workshop.*

Dunbar, R. B., A. R. Leventer, and D. A. Mucciarone (1998), Biogenic sediment fluxes in the Ross Sea, Antarctica: atmospheric and sea ice forcing, *J. Geophys. Res.*, *103*, 30,741–30,760.

Eanes, R., and S. Bettadpur (1996), The CSR3.0 global ocean tide model: Diurnal and Semi-diurnal ocean tides from TOPEX/POSEIDON altimetry, *CRS-TM-96-05, Univ. of Texas, Center for Space Research, Austin, Texas.*

Eanes, R. J. (1994), Diurnal and semidiurnal tides from TOPEX/POSEIDON altimetry, *EOS Trans. AGU*, *75(16)*, 108.

Eanes, R. J. (2002), The CSR 4.0 Global Ocean Tide Model, ftp://ftp.csr.utexas.edu/pub/tide (accessed April 2009).

Egbert, G. D. (2009), TPXO 7.0 Global Ocean Tide Model, http://www.coas.oregonstate.edu/research/po/research/tide/global.html, (accessed April 2009).

Egbert, G. D., and S. Y. Erofeeva (2002), Efficient inverse modeling of barotropic ocean tides, *J. Atmos. Oceanic Technol.*, *19*(2), 183–204.

Egbert, G. D., R. D. Ray, and B. G. Bills (2004), Numerical modeling of the global semidiurnal tide in the present day and in the last glacial maximum, *J. Geophys. Res.*, *109*, C03003, doi:10.1029/2003JC001973.

Eicken, H. (2003), From the microscopic to the macroscopic to the regional scale: Growth, microstructure and properties of sea ice, in *Sea ice - An introduction to its physics, biology, chemistry and geology*, edited by D. N. Thomas and G. S. Dieckmann, chap. 2, Blackwells Science Ltd., London.

Eicken, H., and M. A. Lange (1989), Sea ice thickness data: The many vs. the few, *Geophys. Res. Lett.*, *16*(6), 495–498, doi:10.1029/89GL00670.

Eicken, H., W. B. Tucker, and D. K. Perovich (2001), Indirect measurements of the mass balance of summer Arctic sea ice with an electromagnetic induction technique, *Ann. Glaciol.*, *33*, 194–200.

Eisen, O., and C. Kottmeier (2000), On the importance of leads in sea ice to the energy balance and ice formation in the Weddell Sea, *J. Geophys. Res.*, *105*, 14,045–14,060.

Ekman, M. (1989), Impacts of Geodynamic Phenomena on systems for height and gravity, *J. Geodesy*, *63*(3), 281–296, doi:10.1007/BF02520477.

Ezraty, R., and J. F. Piolle (2001), *CONVECTION SeaWinds on QuikSCAT Polar Sea Ice Grids User Manual*, Department of Oceanography from Space (CERSAT) at IFREMER.

Farrell, S. L., S. W. Laxon, D. C. McAdoo, D. Yi, and H. J. Zwally (2009), Five years of Arctic sea ice freeboard measurements from the Ice, Cloud and land Elevation Satellite, *J. Geophys. Res.*, *114*, C04,008, doi:10.1029/2008JC005074.

Foerste, C., R. Schmidt, R. Stubenvoll, F. Flechtner, U. Meyer, R. Knig, H. Neumayer, R. Biancale, J.-M. Lemoine, S. Bruinsma, S. Loyer, F. Barthelmes, and S. Esselborn (2008), The GeoForschungsZentrum Potsdam/Groupe de Recherche de Godsie Spatiale satellite-only and combined gravity field models: EIGEN-GL04S1 and EIGEN-GL04C, *J. Geod.*, *82*, 331–346, doi:10.1007/s00190-007-0183-8.

Foreman, M. G. G. (1977), Manual for Tidal Heights Analysis and Prediction, *Pacific Marine Science Report 77-10*, Institute of Ocean Sciences, Patricia Bay, Sidney, B.C.

Forsberg, R., and S. Kenyon (2004), Gravity And Geoid in The Arctic Region The Northern Polar Gap Now Filled, in *Proc. GOCE Workshop, ESA-ESRIN.*

Forsberg, R., and H. Skourup (2005), Arctic Ocean gravity, geoid and sea-ice freeboard heights from ICESat and GRACE, *Geophys. Res. Lett.*, *32*, L21502, doi: 10.1029/2005GL023711.

Forsberg, R., A. Olesen, L. Bastos, A. Gidskehaug, and U. M. L. Timmen (2000), Airborne geoid determination, *Earth Planets Space*, *52*, 863–866.

Forsberg, R., H. Skourup, O. B. Andersen, P. Knudsen, S. W. Laxon, A. Ridout, J. Johannesen, F. Siegismund, H. Drange, C. C. Tscherning, D. Arabelos, A. Braun, and V. Renganathan (2007), Combination of spaceborne, airborne and in-situ gravity measurements in support of Arctic sea ice thickness mapping, *Technical Report 7*, Danish National Space Center.

Foster, T. D. (1969), Experiments on haline convection induced by the freezing of seawater, *J. Geophys. Res.*, *74(6)*, 6967–6974.

Fricker, H. A., A. Borsa, B. Minster, C. Carabajal, and B. B. K. Quinn and (2005), Assessment of ICESat performance at the salar de Uyuni, Bolivia, *J. Geophys. Res.*, *32*, L21S06, doi:10.1029/2005GL023423.

Fu, L., and A. Cazanave (2001), *Satellite Altimetry and Earth Sciences, A Handbook of Techniques and Applications*, vol. International Geophysics Seriess Volume 69, 1-122 pp., Academic Press.

Fu, L., and G. Pihos (1994), Determining the response of sea level to atmospheric pressure forcing using TOPEX/POSEIDON data, *J. Geophys. Res.*, *99*(C12), 24,633–24,642.

Galley, R., M. Trachtenberg, A. Langlois, D. Barber, and L. Shafai (2009), Observations of geophysical and dielectric properties and ground penetrating radar signatures for discrimination of snow, sea ice and freshwater ice thickness, *Cold Regions Science and Technology*, *57*, 29–38, doi:10.1016/j.coldregions.2009.01.003.

Gloersen, P., C. L. Parkinson, D. J. Cavalieri, J. C. Comiso, and H. J. Zwally (1999), Spatial distribution of trends and seasonality in the hemispheric sea ice covers: 1978 - 1996, *J. Geophys. Res.*, *104*(C9), 20,827–20,835, doi:10.1029/1999JC900121.

Godin, G., and F. G. Barber (1980), Variability of the tide at some sites in the Canadian Arctic, *Arctic*, *33*(1), 30–37.

Haas, C. (2003), Dynamics versus Thermodynamics: The Sea Ice Thickness Distribution, in *Sea ice - An introduction to its physics, biology, chemistry and geology*, edited by D. N. Thomas and G. S. Dieckmann, chap. 3, Blackwells Science Ltd., London.

Haas, C. (2004), Late-summer sea ice thickness variability in the Arctic Transpolar Drift 1991–2001 derived from ground-based electromagnetic sounding, *Geophys. Res. Lett.*, *31*, L09,402, doi:10.1029/2003GL019394.

Haas, C., J. Haapala, S. Hanson, L.Rabenstein, E. Rinne, and J. Wilkinson (2006), CryoVex 2006 Field Report, *Tech. rep.*, European Space Agency.

Haas, C., A. Pfaffling, S. Hendricks, L. Rabenstein, J.-L. Etienne, and I. Rigor (2008), Reduced ice thickness in Arctic Transpolar Drift favors rapid ice retreat, *Geophys. Res. Lett.*, *35*, L17,501, doi:10.1029/2008GL034457.

Hallikainen, M., and D. P. Winebrenner (1992), The physical basis for sea ice remote sensing, in *Microwave Remote Sensing of Sea Ice*, edited by F. D. Carsey, AGU Geophysical Monograph 68, 1st ed., chap. 3, Washington DC.

Harding, D. J., and C. C. Carabajal (2005), ICESat waveform measurements of within-footprint topographic relief and vegetation vertical structure, *Geophys. Res. Lett.*, *32*, L21S10, doi:10.1029/2005GL023471.

Hegerl, G. C., F. W. Zwiers, P. Braconnot, N. Gillett, Y. Luo, J. M. Orsini, N. Nicholls, J. Penner, and P. Stott (2007), Understanding and Attributing Climate Change, in *Climate Change 2007: The Physical Science Basis. Contribution of Working Group I to the Fourth Assessment Report of the Intergovernmental Panel on Climate Change*, edited by S. Solomon, D. Qin, M. Manning, Z. Chen, M. Marquis, K. Averyt, M. Tignor, and H. Miller, Cambridge University Press, Cambridge, United Kingdom and New York, NY, USA.

Heil, P., J. K. Hutchings, A. P. Worbya, M. Johanssonc, J. Launiainenc, C. Haas, and W. D. Hibler (2008), Tidal forcing on sea-ice drift and deformation in the western Weddell Sea in early austral summer, 2004, *Deep-Sea Res.II*, *55*, 943–962, doi:10.1016/j.dsr2.2007.12.026.

Herring, T. A., and K. Quinn (2001), Atmospheric Delay Correction to GLAS Laser Altimeter Ranges, Algorithm Theoretical Basis Document.

Hibler, W. D. (1979), A dynamic thermodynamic sea ice model, *J. Phys. Oceanogr.*, *9*, 815–846.

Hibler, W. D. (1980), Modeling a variable thickness sea ice cover, *Mon. Wea. Rev.*, *108*, 1943–1973.

Holland, M. M., C. M. Bitz, and B. Tremblay (2006), Future abrupt reductions in the summer Arctic sea ice, *Geophys. Res. Lett.*, *33*, L23503, doi:10.1029/2006GL028024.

Holloway, G., and A. Proshutinsky (2007), Role of tides in Arctic ocean/ice climate, *J. Geophys. Res.*, *112*, C04S06, doi:10.1029/2006JC003643.

Hughes, C. W., and R. J. Bingham (2008), An Oceanographer's guide to GOCE and the Geoid, *Ocean Sciences*, *4*, 15–29.

Hvidegaard, S. M., and R. Forsberg (2002), Sea-ice thickness from airborne laser altimetry over the Arctic Ocean north of Greenland, *Geophys. Res. Lett.*, *29*(20), 1952, doi:10.1029/2001GL014474.

Iacozza, J., and D. Barber (1999), Modelling the Distribution of Snow on Sea Ice Using Variograms, *Atmos.Ocean*, *37*, 21–51.

Ingram, W. J., C. A. Wilson, and J. F. B. Mitchell (1989), Modeling climate change: An assessment of sea ice and surface albedo feedbacks, *J. Geophys. Res.*, *94*, 8609–8622.

Jakobsson, M., N. Cherkis, J. Woodward, B. Coakley, and R. Macnab (2000), A new grid of Arctic bathymetry: A significant resource for scientists and mapmakers, *Eos Transactions, AGU*, *81(9)*, 89, 93, 96.

Kagan, B., D. Romanenkova, and E. Sofinaa (2008), Tidal ice drift and ice-generated changes in the tidal dynamics/energetics on the Siberian continental shelf, *Cont. Shelf. Res*, *28*, 351–368, doi:10.1016/j.csr.2007.09.004.

King, M. A., and L. Padman (2005), Accuracy assessment of ocean tide models around Antarctica, *Geophys. Res. Lett.*, *32*, L23608, doi:10.1029/2005GL023901.

King, M. A., N. T. Penna, P. J. Clarke, and E. C. King (2005), Validation of ocean tide models around Antarctica using onshore GPS and gravity data, *J. Geophys. Res.*, *110*, B08401, doi:10.1029/2004JB003390.

Knauss, J. A. (1978), *Introduction to Physical Oceanography*, Prentice-Hall Inc.

Koentopp, M., O. Eisen, C. Kottmeier, L. Padman, and P. Lemke (2005), Influence of tides on sea ice in the Weddell Sea: Investigations with a high-resolution dynamic-thermodynamic sea ice model, *J. Geophys. Res.*, *110*, C02,014, doi: 10.1029/2004JC002405.

Kovacs, A., and J. S. Holladay (1990), Airborne sea ice thickness sounding, in *Sea Ice Properties and Processes, CRREL Monogr. 90-1*, edited by S. F. Ackley and W. F. Weeks, pp. 225–229, U.S. Army Corps of Eng., Hanover, N. H.

Kowalik, Z., and A. Y. Proshutinsky (1994), The Arctic Ocean tides, in *The Polar Oceans and their Role in Shaping the Global Environment*, pp. 137–158, AGU, Geoph. Monograph.

Kurtz, N. T., T. Markus, D. J. Cavalieri, W. Krabill, J. G. Sonntag, and J. Miller (2008), Comparison of ICESat Data With Airborne Laser Altimeter Measurements Over Arctic Sea Ice, *IEEE Trans. Geosci. Remote Sens.*, *46*, 1913–1924.

Kurtz, N. T., T. Markus, D. J. Cavalieri, L. C. Sparling, W. B. Krabill, A. J. Gasiewski, and J. G. Sonntag (2009), Estimation of sea ice thickness distributions through the combination of snow depth and satellite laser altimetry data, *J. Geophys. Res.*, *114*, C10,007, doi:10.1029/2009JC005292.

Kwok, R. (2000), Recent Changes in Arctic Ocean Sea Ice Motion Associated with the North Atlantic Oscillation, *Geophys. Res. Lett.*, *27*(6), 775–778, doi:10.1029/1999GL002382.

Kwok, R. (2004), Annual cycles of multiyear sea ice coverage of the Arctic Ocean: 19992003, *J. Geophys. Res.*, *109*, C11004, doi:10.1029/2003JC002238.

Kwok, R. (2008), Summer sea ice motion from the 18 GHz channel of AMSR-E and the exchange of sea ice between the Pacific and Atlantic sectors, *Geophys. Res. Lett.*, *35*, doi:10.1029/2007GL032692.

Kwok, R., and G. F. Cunningham (2002), Seasonal ice area and volume production of the Arctic Ocean: November 1996 through April 1997, *J. Geophys. Res.*, *107*(C10), 8038, doi:10.1029/2000JC000469.

Kwok, R., and G. F. Cunningham (2008), ICESat over Arctic sea ice: Estimation of snow depth and ice thickness, *J. Geophys. Res.*, *113*, C08,010, doi:10.1029/2008JC004753.

Kwok, R., and D. A. Rothrock (1999), Variability of Fram Strait ice flux and North Atlantic Oscillation, *J. Geophys. Res.*, *104*(C3), 5177–5190, doi:10.1029/1998JC900103.

Kwok, R., G. F. Cunningham, and S. S. Pang (2004a), Fram Strait sea ice outflow, *J. Geophys. Res.*, *109*, C01009, doi:10.1029/2003JC001785.

Kwok, R., H. J. Zwally, and D. Yi (2004b), ICESat observations of Arctic sea ice: A first look, *Geophys. Res. Lett.*, *31*, L16401, doi:10.1029/2004GL020309.

Kwok, R., G. F. Cunningham, H. J. Zwally, and D. Yi (2006), ICESat over Arctic sea ice: Interpretation of altimetric and reflectivity profiles, *J. Geophys. Res.*, *111*, C06006, doi:10.1029/2005JC003175.

Kwok, R., G. F. Cunningham, H. J. Zwally, and D. Yi (2007), Ice, Cloud, and land Elevation Satellite (ICESat) over Arctic sea ice: Retrieval of freeboard, *J. Geophys. Res.*, *112*, C12,013, doi:10.1029/2006JC003978.

Kwok, R., G. F. Cunningham, M. Wensnahan, I. Rigor, H. J. Zwally, and D. Yi (2009), Thinning and volume loss of the Arctic Ocean sea ice cover: 20032008, *J. Geophys. Res.*, *114*, C07,005, doi:10.1029/2009JC005312.

Lange, M. A. (1990), Development and physical properties of sea ice in the Weddell Sea, Antartica, in *Sea Ice Properties and Processes, CRREL Monogr. 90-1*, edited by S. F. Ackley and W. F. Weeks, pp. 22–28, U.S. Army Corps of Eng., Hanover, N. H.

Laxon, S., N. Peacock, and D. Smith (2003), High interannual variability of sea ice thickness in the Arctic region, *Nature*, *425*, 947–950, doi:10.1038/nature02050.

LeGrand, P., H. Mercier, and T. Reynaud (1998), Combining T/P altimetric data with hydrographic data to estimate the mean dynamic topography of the North Atlantic and improve the geoid, *Ann. Geophys.*, *16*, 638–650.

LeGrand, P., E. J. O. Schrama, and J. Tournadre (2003), An inverse estimate of the dynamic topography of the ocean, *Geophys. Res. Lett.*, *30*, 1062, doi:10.1029/2002GL014917.

Lemoine, F. G., S. C. Kenyon, J. K. Factor, R. Trimmer, N. K. Pavlis, D. S. Chinn, C. M. Cox, S. M. Klosko, S. B. Luthcke, M. H. Torrence, Y. M. Wang, R. G. Williamson, E. C. Pavlis, R. H. Rapp, and T. R. Olson (1998), The Development of the Joint NASA GSFC and NIMA Geopotential Model EGM96, *Tech. rep.*, NASA/TP-1998-206861.

LeProvost, C., F. Lyard, J. Molines, M. Genco, and F. Rabilloud (1998), A hydrodynamic ocean tide model improved by assimilating a satellite altimeter-derived data set, *J. Geophys. Res.*, *103(C3)*, 5513–5529.

Leuschen, C. J., R. N. Swift, J. C. Comiso, R. K. Raney, R. D. Chapman, W. B. Krabill, and J. G. Sonntag (2008), Combination of laser and radar altimeter height measurements to estimate snow depth during the 2004 Antarctic AMSR-E Sea Ice field campaign, *J. Geophys. Res.*, *113*, C04S90.

Levitus, S. (1982), Climatological altas of the world ocean.

Lindsay, R. W., and J. Zhang (2005), The Thinning of Arctic Sea Ice, 1988-2003: Have We Passed a Tipping Point?, *J. Climate*, *18*, 4879–4894.

Lindsay, R. W., and J. Zhang (2006), Assimilation of Ice Concentration in an Ice-Ocean Model, *J. Atmos. Oceanic Technol.*, *23*, 742–749.

Magruder, L., E. Silverberg, C. Webb, and B. Schutz (2005), In situ timing and pointing verification of the ICESat altimeter using a ground-based system, *Geophys. Res. Lett.*, *32*, L21S04, doi:10.1029/2005GL023504.

Makinen, J., and J. Ihde (2008), The Permanent Tide in Height Systems, in *Observing our Changing Earth*, edited by M. G. Sideris, International Association of Geodesy Symposia, pp. 81–87, Springer Berlin Heidelberg, doi:10.1007/978-3-540-85426-5.

Martin, C. F., R. H. Thomas, W. B. Krabill, and S. S. Manizade (2005), ICESat range and mounting bias estimation over precisely-surveyed terrain, *Geophys. Res. Lett.*, *32*, L21S07, doi:10.1029/2005GL023800.

Martin, S., I. Polyakov, T. Markus, and R. Drucker (2004), Okhotsk Sea Kashevarov Bank polynya: Its dependence on diurnal and fortnightly tides and its initial formation, *J. Geophys. Res.*, *109*, C09S04, doi:10.1029/2003JC002215.

Massom, R. A., H. Eicken, C. Haas, M. O. Jeffries, M. R. Drinkwater, M. Sturm, A. P. Worby, X. Wu, V. I. Lytle, S. Ushio, K. Morris, P. A. Reid, S. G. Warren, and I. Allison (2001), Snow on Antarctic sea ice, *Rev. Geophys.*, *39*(3), doi:10.1029/2000RG000085.

Maximenko, N. A., and P. P. Niiler (2004), Hybrid Decade-Mean global sea level with mesoscale resolution, in *Recent Advances in Marine Science and Technology*, edited by N. Saxena, p. 55 59, PACON Int, Honolulu, Hawaii.

Maykut, G. A. (1986), The surface heat and mass balance, in *The Geophysics of Sea Ice*, *NATO ASI Series B: Physics*, vol. 146, edited by N. Untersteiner, pp. 395–463, Plenum Press, New York.

Melling, H. (1998), Detection of features in first-year pack ice by synthetic aperture radar (SAR), *Int. J. Remote Sens.*, *19*(6), 1223–1249.

Menard, Y., E. Jeansou, and P. VIncent (1994), Calibration of the TOPEX/POSEIDON altimeter at Lampedusa: Additional results at Harvest, *J. Geophys. Res.*, *99*(C12), 24,487–24,504.

Miller, P. A., S. W. Laxon, and D. L. Feltham (2005), Improving the spatial distribution of modeled Arctic sea ice thickness, *Geophys. Res. Lett.*, *32*, L18503, doi:10.1029/2005GL023622.

Miller, P. A., S. W. Laxon, and D. L. Feltham (2007), Consistent and contrasting decadal Arctic sea ice thickness predictions from a highly optimized sea ice model, *J. Geophys. Res.*, *112*, C07,020, doi:10.1029/2006JC003855.

Mironov, Y. U., Z. M. Gudkovich, V. P. Karklin, and C. Myrmehl (2007), Sea Ice Conditions in the Arctic Ocean, in *Remote Sensing of Sea Ice in the Northern Sea Route*, edited by O. M. Johannessen, V. Y. Alexandrov, I. Y. Frolov, S. Sandven, L. H. Pettersson, L. P. Bobylev, K. Kloster, V. G. Smirnov, Y. U. Mironov, and N. G. Babich, chap. 4.3, Springer-Praxis.

Morison, J., M. Steele, T. Kikuchi, K. Falkner, and W. Smethie (2006), Relaxation of central Arctic Ocean hydrography to pre-1990s climatology, *Geophys. Res. Lett.*, *33*, L17604, doi:10.1029/2006GL026826.

Morison, J., J. Wahr, R. Kwok, and C. Peralta-Ferriz (2007), Recent trends in Arctic Ocean mass distribution revealed by GRACE, *Geophys. Res. Lett.*, *34*, L07602, doi:10.1029/2006GL029016.

Murty, T. S. (1985), Modification of hydrographic characteristics, tides, and normial modes by ice cover, *Mar. Geod.*, *9*(4), 451–468.

Mysak, L., R. Ingram, J. Wang, and A. van der Baaren (1996), The Anomalous Sea-lce Extent in Hudson Bay, Baffin Bay and th Labrador Sea During Three Simultaneous NAO and ENSO Episodes, *Atmos.Ocean*, *34*, 313–343.

Niedzielski, T., and W. Kosek (2009), Forecasting sea level anomalies from TOPEX/Poseidon and Jason-1 satellite altimetry, *J. Geod.*, *83*, 469476, doi: 10.1007/s00190-008.

Niiler, P. P., N. A. Maximenko, and J. C. McWilliams (2003), Dynamically balanced absolute sea level of the global ocean derived from near-surface velocity observations, *Geophys. Res. Lett.*, *30*(22), 2164, doi:10.1029/2003GL018628.

Ogi, M., and J. M. Wallace (2007), Summer minimum Arctic sea ice extent and the associated summer atmospheric circulation, *Geophys. Res. Lett.*, *34*, L12,705, doi:10.1029/2007GL029897.

Onstott, R. G. (1992), SAR and scatterometer signatures of sea ice, in *Microwave Remote Sensing of Sea Ice*, edited by F. D. Carsey, AGU Geophysical Monograph 68, 1st ed., chap. 5, Washington DC.

Padman, L., and S. Erofeeva (2004), A barotropic inverse tidal model for the Arctic Ocean, *Geophys. Res. Lett.*, *31*, L02303, doi:10.1029/2003GL019003.

Padman, L., and H. A. Fricker (2005), Tides on the Ross Ice Shelf observed with ICESat, *Geophys. Res. Lett.*, *32*, L14503, doi:10.1029/2005GL023214.

Padman, L., S. Y. Erofeeva, and H. A. Fricker (2008), Improving Antarctic tide models by assimilation of ICESat laser altimetry over ice shelves, *Geophys. Res. Lett.*, *35*, L22,504.

Parkinson, C. L., D. J. Cavalieri, P. Gloersen, H. J. Zwally, and J. C. Comiso (1999), Arctic sea ice extents, areas, and trends, 1978 - 1996, *J. Geophys. Res.*, *104*(C9), 20,837, doi:10.1029/1999JC900082.

Peacock, N. R., and S. Laxon (2004), Sea surface height determination in the Arctic Ocean from ERS altimetry, *Geophys. Res. Lett.*, *109*, C07001, doi:10.1029/2001JC001026.

Pease, C. H., S. A. Salo, and J. E. Overland (1983), Drag measurements for first-year sea ice over a shallow sea, *J. Geophys. Res.*, *88*, 2853–2862.

Plag, H. P. (2000), Arctic Tide Gauges: A status report, *Tech. rep.*, UNESCO.

Polonsky, I. N., S. P. Love, and A. B. Davis (2005), Wide-Angle Imaging Lidar Deployment at the ARM Southern Great Plains Site: Intercomparison of Cloud Property Retrievals, *J. Atmos. Oceanic Technol.*, *22*, 628–648.

Randall, D., J. Curry, D. Battisti, G. Flato, R. Grumbine, S. Hakkinen, D. Martinson, R. Preller, J. Walsh, and J. Weatherly (1998), Status of and Outlook for Large-Scale Modeling of AtmosphereIceOcean Interactions in the Arctic, *Bull. Amer. Meteor. Soc.*, *79*, 197–219.

Randall, D. A., R. Wood, S. Bony, R. Colman, T. Fichefet, J. Fyfe, V. Kattsov, A. Pitman, J. Shukla, J. Srinivasan, R. Stouffer, A. Sumi, and K. Taylor (2007), Climate Models and Their Evaluation, in *Climate Change 2007: The Physical Science Basis. Contribution of Working Group I to the Fourth Assessment Report of the Intergovernmental Panel on Climate Change*, edited by S. Solomon, D. Qin, M. Manning, Z. Chen, M. Marquis, K. Averyt, M. Tignor, and H. Miller, Cambridge University Press, Cambridge, United Kingdom and New York, NY, USA.

Rapp, R. H., R. S. Nerem, C. K. Shum, S. M. Klosko, and R. G. Williamson (1991), Consideration of permanent tidal deformation in the orbit determination and data analysis for the Topex/Poseidon Mission, *Tech. Rep. 100775*, NASA Technical Memorandum.

Ray, R. D. (1999), A global ocean tide model from TOPEX/POSEIDON Altimetry: GOT99.2, *Tech. Memo. 209478*, NASA.

Rigor, I. G., J. M. Wallace, and R. L. Colony (2002), Response of Sea Ice to the Arctic Oscillation, *J. Clim.*, *15*, 2648–2663.

Rio, M.-H., and F. Hernandez (2004), A mean dynamic topography computed over the world ocean from altimetry, in situ measurements, and a geoid model, *J. Geophys. Res.*, *109*, C12,032, doi:10.1029/2003JC002226.

Rollenhagen, K., R. Timmermann, T. Janjic, J. Schrter, and S. Danilov (2009), Assimilation of sea ice motion in a finite-element sea ice model, *J. Geophys. Res.*, *114*, C05,007, doi:10.1029/2008JC005067.

Rothrock, D. A., and M. Wensnahan (2007), The accuracy of sea-ice drafts measured from U. S. Navy submarines, *J. Atmos. Oceanic Technol.*, *24*(11), 1936.

Rothrock, D. A., Y. Yu, and G. A. Maykut (1999), Thinning of the Arctic sea-ice cover, *Geophys. Res. Lett.*, *26*(23), 3469–3472, doi:10.1029/1999GL010863.

Rothrock, D. A., J. Zhang, and Y. Yu (2003), The Arctic ice thickness anomaly of the 1990s: A consistent view from observations and models, *J. Geophys. Res.*, *108*(C3), 3083, doi:10.1029/2001JC001208.

Schutz, B. E., H. J. Zwally, C. A. Shuman, D. Hancock, and J. P. DiMarzio (2005), Overview of the ICESat Mission, *Geophys. Res. Lett.*, *32(21)*, GL024,009, doi:10.1029/2005GL024009.

Serreze, M. C., J. A. Maslanik, T. A. Scambos, F. Fetterer, J. Stroeve, K. Knowles, C. Fowler, S. Drobot, R. G. Barry, and T. M. Haran (2003), A record minimum Arctic sea ice extent and area in 2002, *Geophys. Res. Lett.*, *30*(3), 1110, doi:10.1029/2002GL016406.

Shum, C. K., P. L. Woodworth, O. B. Andersen, G. D. Egbert, O. Francis, C. King, S. M. Klosko, C. L. Provost, X. Li, J.-M. Molines, M. E. Parke, R. D. Ray, M. G. Schlax, D. Stammer, C. C. Tierney, P. Vincent, and C. I. Wunsch (1997), Accuracy assessment of recent ocean tide models, *J. Geophys. Res.*, *102*(C11), 25,173–25,194, doi:10.1029/97JC00445.

Shuman, C. A., H. J. Zwally, B. E. Schutz, A. C. Brenner, J. P. DiMarzio, V. P. Suchdeo, and H. A. Fricker (2006), ICESat Antarctic elevation data: Preliminary precision and accuracy assessment, *Geophys. Res. Lett.*, *33*, L07501, doi:10.1029/2005GL025227.

Skourup, H., and R. Forsberg (2008), GEOID, Sea Level and Vertical Datum of the Arctic - Improved by ICESat and Grace, *Geomatica*, *62*, 287–298.

Spinhirne, J. D., S. P. Palm, W. D. Hart, D. L. Hlavka, and E. J. Welton (2005), Cloud and aerosol measurements from GLAS: Overview and initial results, *Geophys. Res. Lett.*, *32*, L22S03, doi:10.1029/2005GL023507.

St-Laurent, P., F. J. Saucier, and J.-F. Dumais (2008), On the modification of tides in a seasonally ice-covered sea, *J. Geophys. Res.*, *113*, C11,014, doi:10.1029/2007JC004614.

Steele, M., and G. Flato (2000), Sea ice growth, melt, and modeling: A survey, in *The Freshwater Budget of the Arctic Ocean*, edited by E. L. Lewis, P. Lemke, T. D. Prowse, and P. Wadhams, chap. 23, pp. 549–587, Kluwer.

Steele, M., J. Morison, W. Ermold, I. Rigor, M. Ortmeyer, and K. Shimada (2004), Circulation of summer Pacific halocline water in the Arctic Ocean, *J. Geophys. Res.*, *109*, C02,027.

Stroeve, J., M. M. Holland, W. Meier, T. Scambos, and M. Serreze (2007), Arctic sea ice decline: Faster than forecast, *Geophys. Res. Lett.*, *34*, L09,501, doi:10.1029/2007GL029703.

Tapley, B. D., S. Bettadpur, M. Watkins, and C. Reigber (2004), The gravity recovery and climate experiment: Mission overview and early results, *Geophys. Res. Lett.*, *31*, L09607, doi:10.1029/2004GL019920.

Thorndike, A. S., D. A. Rothrock, G. A. Maykut, and R. Colony (1975), The Thickness Distribution of Sea Ice, *J. Geophys. Res.*, *80*, 4501–4513.

Timco, G. W., and R. M. W. Frederking (1996), A review of sea ice density, *Cold Regions Science and Technology*, *24*, 1–6.

Tushingham, A. M. (1992), Observations of postglacial uplift at Churchill, Manitoba, *Can. J. Remote Sens.*, *29*, 3418–2425.

Varnai, T., and R. F. Cahalan (2007), Potential for airborne offbeam lidar measurements of snow and sea ice thickness, *J. Geophys. Res.*, *112*, C12S90, doi: 10.1029/2007JC004091.

Voss, K. J., and J. S. Schoonmaker (1992), Temperature-dependence of beam scattering in young sea ice, *Appl. Opt.*, *31*, 3388–3389.

Vossepoel, F. C. (2007), Uncertainties in the mean ocean dynamic topography before the launch of the Gravity Field and Steady-State Ocean Circulation Explorer (GOCE), *J. Geophys. Res.*, *112*, C05,010.

Wadhams, P., and G. Amanatidis (Eds.) (2005), *Arctic Sea-Ice Thickness: Past, Present and Future*, European Commission International Workshop, European Commission.

Wadhams, P., and N. R. Davis (2000), Further evidence of ice thinning in the Arctic Ocean, *Geophys. Res. Lett.*, *27*, 24, doi:10.1029/2000GL011802.

Wadhams, P., J. C. Comiso, J. Crawford, G. Jackson, W. Krabill, R. Kutz, C. B. Sear, R. Swift, W. B. Tucker, and N. R. Davis (1991), Concurrent remote sensing of Arctic sea ice from submarine and aircraft, *Int. J. Remote Sens.*, *12(9)*, 1829–1840.

Wadhams, P., W. B. Tucker, W. B. Krabill, N. Swift, J. C. Comiso, and N. R. Davis (1992), Relationship Between Sea Ice Freeboard and Draft in the Arctic Basin, and Implications for Ice Thickness Monitoring, *J. Geophys. Res.*, *97*(C12), 20,325–20,334.

Warren, S. G., I. G. Rigor, N. Untersteiner, V. F. Radionov, N. N. Bryazgin, Y. I. Aleksandrov, and R. Colony (1999), Snow depth on Arctic sea ice, *J. Clim.*, *12*, 1814–1829.

Wessel, P., and W. H. F. Smith (1991), Free software helps map and display data, *EOS Trans. AGU*, *72*, 441.

Wolf, D., V. Klemann, J. Wunsch, and F.-P. Zhang (2006), A reanalysis and reinterpretation of geodetic and geological evidence of glacial-isostatic adjustment in the Churchill region, Hudson Bay, *Surveys in Geophysics*, *27*(1), 19–61.

Wunsch, C. (1972), Bermuda Sea level in relation to tides, weather, and baroclinic fluctuations, *Rev. of Geophys. and Space Physics*, *10*(1), 1–49.

Yackel, J. J., D. G. Barber, and T. N. Papakyriakou (2001), On the Estimation of Spring Melt in the North Water Polynya using RADARSAT-1, *Atmos.Ocean*, *39(3)*, 195–208.

Yi, D., X. Sun, and H. J. Zwally (2003), A study of the GLAS echo waveform using ground test data, in *EGS - AGU - EUG Joint Assembly, Abstracts.*

Yu, Y., G. A. Maykut, and D. A. Rothrock (2004), Changes in the thickness distribution of Arctic sea ice between 1958-1970 and 1993-1997, *J. Geophys. Res.*, *109*, C08004, doi:10.1029/2003JC001982.

Zhang, J., and D. Rothrock (2001), A Thickness and Enthalpy Distribution Sea-Ice Model, *J. Phys. Oceanogr.*, *31*, 2986–3001.

Zhang, J., D. Rothrock, and M. Steele (2000), Recent Changes in Arctic Sea Ice: The Interplay between Ice Dynamics and Thermodynamics, *J. Clim.*, *13*, 3099–3114.

Zhang, X., and J. E. Walsh (2006), Toward a Seasonally Ice-Covered Arctic Ocean: Scenarios from the IPCC AR4 Model Simulations, *J. Clim.*, *19*, 1730–1747.

Zwally, H. J., B. Schutz, W. Abdalati, J. Abshire, C. Bentley, A. Brenner, J. Bufton, J. Dezio, D. Hancock, D. Harding, T. Herring, B. Minster, K. Quinn, S. Palm, J. Spinhirne, and R. Thomas (2002), ICESat's laser measurements of polar ice, atmosphere, ocean, and land, *J. Geodyn.*, *34*, 405–445.

Appendix A

Sea ice freeboard heights from ICESat

The procedure for deriving the sea ice freeboard heights from ICESat is explained in this section.

1. The ICESat GLAS-13 sea ice altimetry data products are available for downloading through the NSIDC. These granules (files) are first converted from binary to ASCII format using the NSIDC IDL tools.

2. Each GLAS-13 record contains the following parameters (Table A). The NSIDC IDL software were modified to extract the necessary parameters that are needed for the sea ice freeboard estimation. In this study, *i_lat, i_lat, i_UTCTime, i_elev, i_ocElv, i_reflctUcorr, i_gainSet1064, i_SeaIceVar, i_satElevCorr, i_ElvuseFlg, i_numPk* were extracted. The GLAS-13 data file now contain a matrix of the above parameters.

3. Only the data above 66° N were retained. The next step is data filtering. See section 4.2.3 for the filtering procedure. The GLAS-13 data for each mission phase now contain a matrix of the UTC time, latitude, longitude, and corrected sea ice surface elevation.

4. The GOT '00 model from the GLAS-13 product (i_ocElv) was added back to the corrected sea ice surface elevation (see chapter 5). Since the ICESat elevations refer to the Topex/Poseidon ellipsoid, 71 cm was subtracted to reference them to the WGS-84 ellipsoid (section 4.4.1).

5. After the saturation corrections are applied (section 4.2.3), the next step is the estimation of instantaneous sea surface heights. The UTC time, latitude and longi-

Table A.1: ICESat GLAS-13 record

Name	Description
i_rec_ndx	GLAS record index
i_UTCTime	Transmit time of first shot in frame in J2000
i_transtime	One-way transmit time
i_Spare1	Spares
i_deltagpstmcor	Delta GPS time correction
i_dShotTime	Laser shot time deltas (shots 2-40)
i_lat	Coordinate data, latitude, specific to sea ice range
i_lat	Coordinate data, longitude, specific to sea ice range
i_elev	Sea ice surface elevation
i_PADPoint	PAD pointing unit vector in ICRF
i_PODFixedPos	Position orbit vector in ICRF
i_sigmaatt	Attitude quality indicator
i_Azimuth	Local azimuth
i_SolAng	Solar incidence angle
i_tpintensity_avg	Transmit pulse intensity - frame average
i_tpazimuth_avg	Transmit pulse azimuth - frame average
i_tpeccentricity_avg	Transmit pulse eccentricity - frame average
i_tpmajoraxis_avg	Transmit pulse major axis - frame average
i_poleTide	Pole Tide
i_gdHt	Geoid
i_erElv	Solid earth tide elevation (at first and last shot)
i_spElv	Tide elevations, specific
i_ldElv	Load tide elevation
i_spare12	Spares
i_wTrop	Range correction - wet troposphere
i_dTrop	Range correction - dry troposphere
i_surfType	Region type (view byte structure)
i_bs_conf	Blowing snow confidence
i_bs_erd	Blowing snow range delay
i_DEM_elv	DEM elevation
i_refRng	Reference range
i_TrshRngOff	Threshold retracker range offset
i_siRngOff	Sea ice range offset
i_SigEndOff	Signal end range offset
i_cntRngOff	Centroid range offset
i_reflctUncorr	Reflectivity not corrected for atmospheric effects
i_reflCor_atm	Reflectance correction, atmosphere

i_maxSmAmp	Peak amplitude of smoothed received echo
i_ocElv	Ocean tide elevation (at first and last shot)
i_numPk	Number of peaks found in the return
i_spare11	Spares
i_skew2	Skewness
i_spare4	Spares
i_BergElev	Iceberg elevation
i_spare10	Spares
i_SiRngFst	Sea ice range increment to first peak
i_SeaIceVar	Standard deviation of the sea ice Gaussian fit
i_ElvuseFlg	Elevation use flag (view byte structure)
i_atm_avail	Atmosphere availaility flag (view byte structure)
i_erd	Estimated range delay
i_rdu	Range delay uncertainty
i_cld1_mswf	Cloud multiple scattering warning flag (view byte structure)
i_MRC_af	Medium resolution cloud availability flag (view byte structure)
i_spare9	Spares
i_ElvFlg	Elevation definition flag (view byte structure)
i_rng_UQF	Range offset quality/use flag (view byte structure)
i_atmQF	Atmosphere flag (view byte structure)
i_timecorflg	Time correction flag (view byte structure)
i_APID_AvFlg	APID data availability flag (view byte structure)
i_AttFlg2	Attitude flag 2 (view byte structure)
i_spare5	Spares
i_FrameQF	Altimeter frame quality flag (view byte structure)
i_OrbFlg	POD flag (orbit flag) (view byte structure)
i_rngCorrFlg	Range correction flag (view byte structure)
i_CorrStatFlg	Correction status flag (view byte structure)
i_beam_coelev	Co-elevation
i_beam_azimuth	Azimuth
i_AttFlg1	Attitude flag 1 (view byte structure)
i_Spare6	Spares
i_DEM_hires_src	High Resolution Source Flag (view byte structure)
i_DEM_hires_elv	High Resolution Elevation
i_satNdx	Saturation Index

i_satElevCorr	Saturation Elevation Correction
i_satCorrFlg	Saturation Correction Flag (view byte structure)
i_satNrgCorr	Saturation Energy Correction
i_spare13	Spares
i_gval_rcv	Gain Value used for Received Pulse
i_RecNrgAll	Received Energy signal begin to signal end
i_FRir_cldtop	Full Resolution 1064 Cloud Top
i_FRir_qaFlag	Full Resolution 1064 Quality Flag (view byte structure)
i_FRir_ODflg	Full Resolution 1064 Optical Depth Flag
i_FRir_intsig	Full Resolution 1064 Integrated Signal
i_spare14	Spares
i_Surface_temp	Surface Temperature
i_Surface_pres	Surface Pressure
i_Surface_relh	Relative Humidity
i_maxRecAmp	Max Amplitude of Received Echo
i_sDevNsOb1	Standard deviation of 1064 nm background noise (alternate)
i_pctSAT	Percent Saturation
i_TxNrg	1064 nm laser transmit energy
i_eqElv	Equilibrium tide elevation (at first and last shot)
i_spare8	Spares

tude are used to calculate the ocean tides, geoid height, mean dynamic topography and inverse barometric effect at each ICESat footprint using the models described in section 4.4. An additional correction was calculated for the geoid heights to change its permanent-tide reference system from tide-free to zero-tide (section 4.4.2). The sum of these parameters yields the instantaneous sea surface height at the ICESat footprint.

6. The estimated instantaneous sea surface height is then removed from the GLAS-13 elevation obtained from step 4 to get the total freeboard (sea ice plus snow thickness). The final output of the freeboard retrieval algorithm is time, latitude, longitude and total freeboard at each ICESat footprint. Finally, the data are gridded onto a 10' × 5' grid and plotted using the Generic Mapping Tools (see chapter 7).